



PONTIFICIA UNIVERSIDAD CATÓLICA DEL PERÚ

Escuela de Posgrado

*Fusion of thermal and three-dimensional data for chronic
wound monitoring*

Tesis para obtener el grado académico de Doctora en Ingeniería que
presenta:

Evelyn Patricia Gutierrez Ayala

Asesores:

Dra. Sylvie Françoise Treuillet

Dr. Benjamín Castañeda Aphan

Lima, 2023

Informe de Similitud

Yo, Dr. Benjamín Castañeda Aphan, docente de la Escuela de Posgrado de la Pontificia Universidad Católica del Perú, asesor(a) de la tesis/el trabajo de investigación titulado

Fusión of Thermal and three dimensional data for chronic wound monitoring, de la autora Evelyn Patricia Gutierrez Ayala, dejo constancia de lo siguiente:

- El mencionado documento tiene un índice de puntuación de similitud de 14%. Así lo consigna el reporte de similitud emitido por el software *Turnitin* el 05/04/2023.
- He revisado con detalle dicho reporte y la Tesis o Trabajo de Suficiencia Profesional, y no se advierte indicios de plagio.
- Las citas a otros autores y sus respectivas referencias cumplen con las pautas académicas.

Lugar y fecha:

Lima, 7 de abril de 2023

Apellidos y nombres del asesor / de la asesora: <u>Castañeda Aphan, Benjamín</u>	
DNI: 10791304	
ORCID: 0000-0002-1913-0636	
Firma	

ÉCOLE DOCTORALE MATHÉMATIQUES, INFORMATIQUE, PHYSIQUE
THÉORIQUE ET INGÉNIERIE DES SYSTÈMES
LABORATOIRE PRISME / LABORATORIO DE IMÁGENES MÉDICAS - PUCP

THÈSE EN COTUTELLE INTERNATIONALE présentée par :

Evelyn GUTIERREZ

soutenue le : 13 Avril 2023

pour obtenir le grade de :
Docteur de Université d'Orléans
et de l'*Université Pontificia Universidad Católica de Peru*

Discipline/ Spécialité : Informatique

Fusion of thermal and three-dimensional data for chronic wound monitoring

THÈSE dirigée par :

Mme. Sylvie TREUILLET
M. Benjamín CASTAÑEDA

Maître de Conférences, Université d'Orléans
Professeur des universités, Pontificia Universidad Católica del Perú

RAPPORTEURS :

Mme Sandra PEREZ
M. Yannick BENEZETH

Maître de conférences, Pontificia Universidad Católica del Perú
Maître de Conférences, Université de Bourgogne

JURY :

Mme. Sylvie TREUILLET
M. Benjamín CASTAÑEDA
M. Walter BLONDEL
M. Pierre VIEYRES

Maître de Conférences, Université d'Orléans
Professeur des universités, Pontificia Universidad Católica del Perú
Professeur des universités, Université de Lorraine
Professeur des universités, Université d'Orléans,
Laboratoire PRISME – IUT Bourges
Maître de conférences, Pontificia Universidad Católica del Perú
Maître de Conférences, Université de Bourgogne

Acknowledgments

I am deeply grateful to all those who have contributed to the successful completion of my thesis. Their support, guidance, and encouragement have been indispensable in helping me achieve my academic goals.

First and foremost, I would like to extend my heartfelt appreciation to my advisors, Dr. Sylvie Treuillet and Dr. Benjamin Castaneda, for providing me with the opportunity to undertake this project and for generously offering their valuable time and guidance throughout its development.

I also extend my sincere gratitude to the reviewers for their insightful comments and constructive feedback, which have been invaluable in refining my work and ensuring its quality.

To my family, my parents, Alberto, and Rockito, I am deeply grateful for their unconditional love and unwavering emotional and financial support. Their constant encouragement and motivation have been a source of inspiration for me throughout my academic journey.

Special thanks to Omar for his friendship, and availability to answer my questions whenever needed. Special thanks also to my friends Ivonne, Vilma, Fiorella and Fedra, who provided me with encouragement, emotional support, and who have made the completion of my thesis more enjoyable.

I am also grateful to all the friends I had the pleasure of meeting during the course of this project, including Gabriel, Stefano, Antonio, Dian, Kouboura, Rania, Doha, Giselle, Marouane, Yassine, Amine, Fadila, Aymen, and others I might have missed. Their contributions and conversations have enriched my academic and personal experiences, and I am grateful for the friendships and connections I have made along the way.

Once again, thank you to all who have supported me throughout this journey. I could not have completed this thesis without their contributions, and I am grateful for the knowledge and memories that I will carry with me as a result of this experience.

Evelyn Gutierrez

Abstract

Chronic wounds are a serious health problem because they do not follow a normal healing process and take a long time to heal. Monitoring the evolution of the wound is vital to evaluate the current treatment and determine the need for a different approach. Traditionally, this assessment is based on manual measurements and visual observation, which can be subjective and non-quantitative, leading to uncertainty in patient follow-up.

This thesis proposes to leverage color and thermal imaging from cameras embedded in a smartphone to provide a non-invasive tool for wound assessment. Standard and affordable devices enables its applicability and scalability in clinical settings.

We propose a methodology to create realistic and accurate 3D thermal models from a set of images captured with affordable and handheld devices. This approach was automated and evaluated in clinical settings on a total of 68 wound cases with varying degrees of severity, in Lima, Peru. Our findings show the feasibility of this method and highlight its potential for wound assessment through the use of thermal metrics derived from the 3D thermal models.

Keywords: 3D models, thermography, chronic wounds, portable devices.

Résumé (Français)

Les plaies chroniques constituent un problème de santé grave car elles ne suivent pas un processus de guérison normal et prennent beaucoup de temps à guérir. Le suivi de l'évolution de la plaie est vital pour évaluer le traitement actuel et déterminer la nécessité d'une approche différente. Traditionnellement, cette évaluation est basée sur des mesures manuelles et une observation visuelle, qui peuvent être subjectives et non quantitatives, entraînant une incertitude dans le suivi du patient.

Cette thèse propose d'exploiter l'imagerie couleur et thermique des caméras embarquées dans un smartphone pour fournir un outil non invasif d'évaluation des plaies. Des appareils standards et abordables permettent son applicabilité et son adaptabilité en milieu clinique.

Nous proposons une méthodologie pour créer des modèles thermiques 3D réalistes et précis à partir d'un ensemble d'images capturées avec des appareils portables et abordables. Cette approche a été automatisée et évaluée en milieu clinique sur un total de 68 cas de plaies de différents degrés de gravité, à Lima, au Pérou. Nos résultats montrent la faisabilité de cette méthode et mettent en évidence son potentiel pour l'évaluation des plaies grâce à l'utilisation de métriques thermiques dérivées des modèles thermiques 3D.

Mots clés : Modèles 3D, thermographie, plaies chroniques, appareils portables

Resumen (Español)

Las heridas crónicas constituyen un grave problema de salud porque no siguen un proceso normal de cicatrización y tardan mucho tiempo en curar. El seguimiento de la evolución de la herida es vital para evaluar el tratamiento actual y determinar la necesidad de un enfoque diferente. Tradicionalmente, esta evaluación se basa en mediciones manuales y en la observación visual, que pueden ser subjetivas y no cuantitativas, lo que genera incertidumbre en el seguimiento del paciente.

Esta tesis propone aprovechar las imágenes térmicas y a color de cámaras integradas en un smartphone para proporcionar una herramienta no invasiva de evaluación de heridas. Los dispositivos estándar y asequibles permiten su aplicabilidad y escalabilidad en entornos clínicos.

Proponemos una metodología para crear modelos térmicos 3D realistas y precisos a partir de un conjunto de imágenes captadas con dispositivos asequibles y portátiles. Este enfoque se automatizó y evaluó en entornos clínicos sobre un total de 68 casos de heridas con distintos grados de gravedad, en Lima, Perú. Nuestros hallazgos muestran la viabilidad de este método y destacan su potencial para la evaluación de heridas mediante el uso de métricas térmicas derivadas de los modelos térmicos 3D.

Palabras clave: modelos 3D, termografía, heridas crónicas, dispositivos portátiles

Contents

Acknowledgments	iv
Abstract	v
Introduction	1
The problem	1
STANDUP Project WP2	2
Contributions	2
Structure of this thesis	2
1 Medical Context	4
1.1 Chronic wounds	4
1.2 Wound assessment tools	5
1.2.1 Traditional wound assessment	5
1.2.2 Imaging tools for wound assessment	5
1.3 Wound evaluation metrics	7
1.3.1 Wagner grading system	7
1.3.2 Evaluation regions	7
1.3.3 Geometrical metrics	9
1.3.4 Thermal metrics	9
1.4 Discussion	11
1.5 Conclusion	12
2 Three dimensional modeling	13
2.1 3D modeling definitions	13
2.2 3D acquisition systems applied to wounds	14
3D acquisition systems for wounds	15
2.3 Basics of 3D Computer Vision	17
Camera reference frame	17
2.3.1 Camera calibration	18
Triangulation	19

Bundle adjustment	20
2.3.2 Computer Graphics	20
2.4 Structure from Motion (SfM)	21
2.5 Conclusion	23
3 Two dimensional thermography	24
3.1 Physics of infrared radiation	24
3.1.1 History of infrared	25
3.1.2 Basic concepts	25
3.2 Thermography	27
3.2.1 History of infrared remote detectors	27
3.2.2 Thermal Imaging devices	28
3.2.3 Skin thermography	30
3.2.4 Portable and low-cost thermal cameras	31
3.3 Accuracy of thermal imaging systems	32
3.4 Conclusion	33
4 Towards improved temperature estimation according to point of view	35
4.1 Experimental setup	35
4.1.1 Acquisition protocol	36
4.1.2 Estimation of camera angle and distance fom object	36
4.1.3 Temperature estimation from IR image	37
4.1.4 Evaluation metrics	37
4.2 Stage I: Exploration	38
4.3 Stage II: Improving temperature estimation	39
4.3.1 Regression model with inverse prediction	40
4.3.2 Combining temperatures from multiple views	42
4.4 Conclusion	43
5 Thermal 3D modeling	44
5.1 Overview of multimodal registration	45
5.1.1 RGB-IR registration	45
5.2 Multimodal Stereo Calibration	47
5.3 State-of-the-art on thermal 3D model creation	49
5.3.1 Calibration-based method	49
5.3.2 Multimodal (IR-RGB) registration approach	53
5.4 Proposed methodology for multiview thermal 3D model	54
5.4.1 Stage I: Calibration-based thermal 3D model creation	56
5.4.2 Stage II. Refinement of thermal camera poses	57

5.4.3	Stage III: Fusion of several thermal views	59
5.4.4	Evaluation of multi-view consistency	60
5.5	Proof of concept on real wounds	60
5.5.1	Calibration-based thermal 3D models	61
5.5.2	Thermal camera pose refinement	62
5.5.3	Multi-View Thermal 3D models	62
5.6	Discussion	64
5.7	Conclusion	65
6	Clinical Application	67
6.1	Towards automated creation of thermal 3D models	67
6.1.1	Background Removal	68
6.1.2	3D model scaling	69
6.1.3	3D wound segmentation	70
6.2	Quantitative wound measurements	70
6.2.1	Evaluation regions	71
6.2.2	Wound surface area	71
6.2.3	Thermal metrics	71
6.3	Experimental Setup	72
6.3.1	Research protocol in clinical environment	73
6.3.2	Data Acquisition	73
6.3.3	Database	75
6.4	Evaluation of thermal 3D models and metrics	76
6.4.1	Relevance of thermal metrics for wound assessment	77
6.5	Discussion	80
6.6	Conclusion	82
7	Conclusion and perspectives	83
7.1	Conclusion	83
7.2	Perspectives	84
	Using 3D thermal models beyond chronic wounds	85
	Computing resources	85
	Appendix	86
7.3	Other attempts to create thermal 3D models	86
7.3.1	SfM with thermal imaging only	86
7.4	Visualization Tools	86
7.4.1	Online HTML visualization	86
7.4.2	Smartphone Application	88

<i>CONTENTS</i>	xi
Related works	89
Bibliography	90

List of Figures

1.1	Wound measurement from a 2D image using a commercial mobile application. Image obtained from [15].	6
1.2	Wagner grading system obtained from [11]. The arrows represent the progression of chronic wounds. The wound can evolve from grade 0 to grade 5. Furthermore, wound stages can be reverted to grade 0 with proper care, except if the wound reaches grade 5.	8
1.3	Illustration of 3D geometrical metrics: wound depth in (a) and wound volume in (b) and (c) estimated using different approaches. Images obtained from [108, 91].	9
1.4	Example of manually selected ROIs in the wound and periwound; as well as the thermal measurements obtained for each ROI.	10
2.1	Illustration of types of 3D models for surface modeling of a toe. Images based on our own data collection.	14
2.2	Commercial systems based on proprietary hardware and software.	17
2.3	Illustration of the camera reference frame, the image plane and the 3D object.	17
2.4	Projection of 3D points from the world frame into the image plane.	18
2.5	Illustration of triangulation of a point from points matched in two 2D images.	19
2.6	Illustration of the rasterization of a triangle into a 2D image pixel plane. Martin Kraus, Pixels covered by a triangle, CC BY-SA 3.0	21
2.7	General 3D SfM reconstruction pipeline implemented in Meshroom, a well-known open source software for passive 3D reconstruction.	22
3.1	Electromagnetic waves and the visible part of the electromagnetic spectrum. Image created by Philip Ronan, Gringer, EM spectrumrevised, higlighed IR spectrum by Evelyn Gutierrez, CC BY-SA 3.0	25
3.2	Representation of Herchel’s experiment with Newton’s prism. The temperature outside the visible spectrum is generally 20°C (top). The temperature increases to 25.9°C in the red region (center). The temperature increases further outside the visible spectrum to 27°C (bottom). This is explained by invisible infrared radiation (Images obtained from [42]).	26
3.3	Illustration of the radiation density emitted by a black body at different temperatures. The wavelength of the radiation peak increases as the temperature decreases, i.e. wavelength is inversely proportional to the temperature. Image obtained from 4C, Wiens law, modified by Evelyn Gutierrez, CC BY-SA 3.0	28
3.4	Illustration of the radiation sources reaching the thermal camera, composed of radiation from the object (red), radiation from the surroundings reflected on the object and the camera lens (blue), and radiation from the atmospheres (purple). Original image obtained from [61]. Colors were added to differentiate radiation sources.	29

3.5	Illustration of a radiometric JPG image, and conversion to temperatures using the Equation 4.5	30
3.6	Illustration of the FlirOne Pro thermal camera attached to a smartphone for obtaining thermal images of a wound phantom.	31
3.7	Illustration of the visible spectrum detected by a common smartphone camera, and the IR range spectrum detected with a FlirOne handheld camera [8]).	33
3.8	Schema of error source of any thermal camera as described by [61]. Camera-object angles and distances are highlighted as in this thesis, they are taken into account for improving temperature estimations.	33
4.1	Experimental setup: A pair of images RGB-IR images obtained from FlirOne Gen3. Temperature controlled standatd is observed from different angles and distances.	36
4.2	Illustration of the distance and angle of observation between the camera and the target object.	37
4.3	Target object and region of interes (ROI) from which the temperature has been measured	38
4.4	Boxplots for relative errors as a function of deciles of distances and deciles of angles of the camera from the temperature-controlled target.	40
4.5	Illustration of changes in the regression model equation when using inverse prediction.	41
4.6	Weighting functions for distance (left) and angles (right) to calculate the multiview averaged temperature.	42
5.1	Illustration of the lack of distinctive silhouettes in IR images which can lead to mismatched registration of silhouettes.	46
5.2	Infrared and corresponding RGB image of a foot where contours are not clearly defined in the infrared image due to the presence of other leg.	47
5.3	FlirOne Pro thermal camera. In this camera, RGB and IR sensors are in fixed relative positions.	47
5.4	Example of the detection of edges on RGB image (left) and its corresponding IR image (right) for a multimodal calibration chessboard.	48
5.5	Our classification scheme for thermal 3D modeling methods.	49
5.6	Stationary thermal 3D model systems. Images obtained from [101] (a), [30] (b), [12] (c), [51] (d), and [105] (e), [53] (f).	50
5.7	Portable thermal 3D model creation systems. Device images obtained from [96] (a), [71] (b), and [81] (c).	52
5.8	Summary of the inputs, outputs and stages of the proposed methodology.	55
5.9	Workflow of the proposed methodology.	55
5.10	Workflow illustrating the creation of calibration-based thermal 3D models using passive reconstruction and multimodal calibration of stereo cameras.	56
5.11	Illustration of the thermal camera pose refinement process based on the reference thermal 3D model and optimization.	58
5.12	Optimization process carried out for each thermal view to refine camera pose.	59
5.13	Six cases of foot and lower extremity injuries used to show application of our algorithm for multi-view thermal 3D model creation.	61

5.14	Calibration-based thermal 3D models created based on 3D models from passive reconstruction and initial infrared camera poses estimated by stereo multimodal calibration.	61
5.15	Example of thermal 3D registration before and after the IR Camera Pose Refinement	62
5.16	Illustration of synthetic thermal images created by projecting the reference view model using the baseline (left), the adjusted IR camera pose (center), and the original thermal image (right). The dashed horizontal lines show that the synthetic images are in better alignment with the actual thermal image when the camera pose is adjusted.	63
5.17	Two examples of calibration-based thermal 3D models and their corresponding multi-view thermal 3D models. Multi-view thermal models created with the proposed methodology.	63
5.18	Six cases were chosen to show the thermal 3D creation.	64
6.1	Pipeline for automated creation of thermal 3D models.	68
6.2	Automatic background removal procedure by deep learning based skin segmentation: raw RGB image (left) and the corresponding image after applying background removal (right).	68
6.3	Example of 3 cases where the background removal treatment was applied. Baseline 3D models with reconstructed background objects (top) and corresponding 3D models once the background removal process is implemented (bottom).	69
6.4	Illustration of Aruco markers detection process and computation of the scale factor.	70
6.5	Ilustración de la segmentación en imágenes 2D, y su resultado en el modelo 3D de una herida.	70
6.6	Depicted in the 3D model are the distinct regions of skin, including the wound bed, wound edges, peri-wound, and normal skin.	72
6.7	Workflow for image acquisition in the clinical environment	73
6.8	A sample of an ArUco marker. The ArUco marker is easy to detect by well known algorithms implemented in opencv.	74
6.9	Acquisition configuration proposed as a reference. First, acquisition is performed with the high-resolution camera of the mobile device in two circular motions in front of the wound. Next, a small thermal image is acquired with the thermal camera in a similar motion, and a thermal image captured from further away.	75
6.10	Illustration of handheld image acquisition using portable devices in clinical settings for creating thermal 3D models of wounds.	76
6.11	Examples of 3D color and thermal models created for three different wound sizes and wound grades. In each case, color 3D models (left), thermal 3D models (center) and blended color and thermal 3D model visualization (right) are displayed.	77
6.12	Distribution of temperature differences for different grades of wounds. The wound grade corresponds to the Wagner classification for diabetic wounds.	78
6.13	Distribution of temperature differences for different grades of wounds. The wound grade corresponds to the Wagner classification for diabetic wounds.	79
7.1	Example of SfM reconstruction using only thermal images.	86
7.2	Preview of a web page created to organize and navigate through the results of thermal 3D modeling.	87
7.3	Visualization tool to observe the color and thermal 3D model on the web page.	87

7.4 Preview of the smartphone application which provides acquisition support and visualization of results.	88
--	----

List of Tables

1.1	Previous studies that have shown thermography to be useful for wound assessment, organized based on the portability of the system, whether smartphone-connected use is possible, and inclusion of 3D models.	7
1.2	Previous studies where thermal metrics were studied for wound evaluation or monitoring, classified by type of thermal metrics analyzed.	10
1.3	Previous studies where either thermography, or 3D models were analysed for wound assessment.	10
2.1	Commercial systems based on proprietary hardware and software for wound imaging. 16	
3.1	Wavelength of the radiation peak, according to Wien’s Law, for a black body at 20°C, 30°C and 40°C. These temperatures are considered since this temperature range is found in the skin of the human body.	31
3.2	Comparison of size and price for various thermal camera devices	32
3.3	Comparison of size and price for various thermal camera devices	32
4.1	Distribution of distances (in centimeters) on the 365 acquired images	38
4.2	Distribution of angles (in degrees) on the 365 acquired images	39
4.3	Summary of temperature errors on the 365 acquired images	39
4.4	Statistics on the errors before and after applying the proposed method to improve the estimated temperatures from 5-fold cross-validation testing on 240 images. . .	41
4.5	Estimated coefficients for the temperature correlation model.	41
4.6	Absolute error and relative error using raw images, mean value and weighted mean to estimate temperatures.	43
5.1	Studies on the creation of thermal 3D models using stationary systems.	50
5.2	Studies on the creation of thermal 3D models using calibration-based portable systems.	52
5.3	Intraclass Correlation Coefficient (ICC) before and after the refinement of thermal camera poses. Last columns shows the relative change in ICC.	64
6.2	Distribution of wound grades in the 68 thermal 3D models processed.	76
6.3	Statistics for temperature differences, including the mean and its 95% confidence interval (CI). The final column displays the p-value obtained from a t-test that was used to determine whether the temperature differences between evaluation regions are statistically different from zero.	78

6.4	ANOVA test results for each temperature difference metric, to test for significant differences between wound grades.	78
6.5	Statistical analysis of the coefficient of variation (CV) metrics obtained from thermal 3D models created for 68 wound cases. The table presents each evaluated metric along with its basic statistical measures, such as minimum value, quartile 1, median, mean, quartile 3, and maximum.	79
6.6	Kruskall Wallis test results to assess whether thermal variability is significantly different between wound grades.	80

Introduction

The problem

Chronic wound treatment are a serious health concern with significant costs, accounting for 2-4% of healthcare expenditure in Europe and increasing every year[75]. Moreover, worldwide, it is estimated that 15% of people with diabetes will suffer from chronic wound, and diabetic foot ulcers which lead to limb amputation and a high mortality rate similar to some types of cancer. [17, 45, 9].

Chronic wounds, such as leg ulcers, pressure sores, and diabetic wounds, can take months to heal and do not typically heal within expected time frames. Proper monitoring of these wounds is crucial to avoid complications and ensure optimal healing outcomes. However, traditional wound monitoring methods in clinical settings often rely on subjective visual observations and manual measurements which can be time-consuming, and painful.

This lack of adequate wound assessment systems highlights a pressing need for affordable and user-friendly devices. These tools would support wound monitoring both in medical centers and at home, particularly in rural areas lacking access to medical resources. With the development of such devices, patients can receive timely and reliable treatments, leading to better wound healing and improved quality of life.

Imaging tools provide automatic metrics on the visual characteristics of wounds for follow-up, and recent advancements in digital cameras on smartphones make it easy to obtain estimates of geometrical metrics with a simple image capture. While 2D images provide cost-efficient and useful information in wound follow-up, they only offer a limited view of the wound.

On the other hand, 3D models provide more comprehensive and informative metrics that accurately reflect the wound's condition [47, 54]. Moreover, thermal information is also valuable in wound assessment, especially to evaluate the evolution of the wound or assess if the wound has an infection. [27, 14, 35]

By combining 3D modeling and thermography, complementary information can be centralized to provide a more comprehensive understanding of wound conditions. Recent technology advancements make obtaining 3D models and thermography easier and more affordable than in the past. However, most studies only focus on either of the two modalities, 3D models or thermography, and few studies combine both. Furthermore, most studies that do use both require complex settings or expensive equipment, making them inaccessible and impractical to most healthcare providers.

The need for an affordable and portable system capable of generating thermal 3D models for wound assessment is critical. Existing studies propose specialized, expensive and complex systems with limited application to large patient populations. However, the availability of an accessible, low-cost tool for wound assessment would be of great benefit to both patients and clinicians. Clinicians would be able to make more informed treatment decisions more quickly, resulting in better outcomes. In addition, a three-dimensional visualization of the wound would inform patients of the progress of their wound, motivating them to continue treatment. In the long term, patients could use this technology to assess the wound remotely from home, which would reduce the overall cost and make treatment more convenient for them. Therefore, the study of thermal 3D modeling is essential to improve wound management and patient outcomes.

STANDUP Project WP2

This research work contributes to the MSCA RISE project STANDUP (Smartphone Thermal ANalysis for Diabetic foot Ulcer Prevention and treatment) funded by the European Community [87]. Started in January 2018, the project brings together 6 universities all over the world and of 2 European high tech companies with the aim of reducing DFU incidence by using a smartphone associated to a thermal camera plugged into the smartphone.

Within the project, a Work Package, the Work Package (WP2), is dedicated to the evaluation of the healing of a foot ulcer by a multimodal approach combining color imaging, 3D reconstruction and thermal now available on smartphones. The WP2 is focused on developing a mobile application, which will integrate color imaging, 3D reconstruction, and thermal imaging to provide a more complete assessment of ulcer progression over time by monitoring tools to help diagnose and track changes in ulcers from one visit to the next. The present thesis is carried out within the framework of WP2.

Contributions

Starting from an analysis of the state of the art, the expected contributions of this work concern the creation of a reliable and accurate thermal 3D model from a low-cost camera plugged on a Smartphone and its application to the monitoring of chronic wounds.

In this context, our contribution can be summarized as follows:

- The study of accuracy of skin and wound temperature measurements from freehand acquisitions, and using a low-cost camera.
- The optimization of temperature estimations in a multi-view thermography context.
- An improved methodology for combining thermography and 3D models into an unified and automated process suitable for clinical application.
- An analysis of thermal metrics and their potential for chronic wound assessment.
- Finally, implementation in a clinical study on real patients to demonstrate the feasibility and usefulness of the proposed tool in a clinical setting.

These contributions represent a significant advance in wound assessment, providing an affordable and practical tool for creating 3D thermal models from which objective wound monitoring metrics can be obtained.

Structure of this thesis

With the aim of providing a comprehensive understanding of the assessment and monitoring of chronic wounds using computer vision techniques, this thesis is structured as follows:

- Chapter 1 provides medical context for chronic wounds and their evaluation. This includes a review of imaging systems and metrics utilized on chronic wound assessment.
- Chapter 2 introduces concepts on 3D modeling, and computer vision, which are the basics for the development of algorithms for thermal 3D models in later chapters.
- In Chapter 3, basic concepts on infrared radiation, thermography, and thermal cameras are introduced, providing a foundation for the temperature correction methodologies presented in the following chapter.

- Chapter 4 presents two distinct approaches to improving temperature estimation, with a detailed evaluation of the methodologies in an experimental setup. Results are compared and analyzed to identify the most useful approach.
- Chapter 5 includes a review of previous works for the creation of thermal 3D models. Moreover, this chapter presents our proposed methodology for creating accurate thermal 3D models using multi-view RGB and IR images from portable devices.

Finally, in chapter 6, a process for automating the creation of the thermal 3D model is presented. Then, the feasibility of the process of thermal 3D model creation is shown in a clinical study on chronic wounds of diabetic patients. Thermal metrics created with our thermal 3D models are analyzed to determine their usefulness in wound assessment and monitoring.

Chapter 1

Medical Context

Contents

1.1	Chronic wounds	4
1.2	Wound assessment tools	5
1.3	Wound evaluation metrics	7
1.4	Discussion	11
1.5	Conclusion	12

Chronic wounds are a significant healthcare concern affecting millions of people worldwide. These wounds can be challenging to manage, often leading to prolonged healing times, increased health-care costs, and decreased quality of life for patients. Proper assessment and management of chronic wounds are critical to ensure optimal patient outcomes.

This chapter aims to provide general information for readers who may not be familiar with chronic wound assessment and the available medical tools. The chapter covers the definition of chronic wounds, an overview of the wound assessment tools available, and commonly used wound evaluation metrics.

1.1 Chronic wounds

Wounds consist of an injury to the skin after which a healing process usually takes place. Depending on how the healing process develops, wounds can be classified as acute or chronic. A wound is considered chronic if it takes more than 4 to 6 weeks to heal. Causes of chronic wound include leg ulcers, pressure sores, diabetic wounds. Chronic wounds can become stalled at some stage of the healing process, which can lead to complications such as bacterial colonization, infection and tissue death. These complications could lead to amputations and in the worst case can be life-threatening.

As a general rule, a wound that takes longer than 3 months is considered a chronic wound [68]. Chronic wounds occur due to vascular compromise, chronic inflammation, or repeated tissue aggression [20]. Thus, certain populations are at higher risk to have wounds that can become chronic: for example, diabetic patients and the aging population. Chronic wounds usually are classified into one of these categories: diabetic foot ulcers, venous leg ulcers and pressure ulcers [68].

1.2 Wound assessment tools

1.2.1 Traditional wound assessment

Traditionally wound assessment is done based on manual measurement and visual observations. This assessment is the most common way to document wound progression and is commonly performed in a healthcare facility by an experienced nurse or physician.

Apart from the qualitative assessment, quantitative measurements (wound length, width, depth, and volume) might manually be obtained using a ruler close to the wound or a dampened cotton tip applicator for depth. Therefore, traditional assessment is inaccurate, painful, and uncomfortable for the patient. In addition, contact tools such as rulers or tapes increase the risk of cross-contamination by bacterial spread.

Manual measurements do not require major equipment; however, the information collected by the traditional method is limited, subjective assessment, and prone to human error. Moreover, traditional assessment is time-consuming. The complexity and time costs increase when documenting large wounds and multiple wounds in one area.

1.2.2 Imaging tools for wound assessment

Unlike manual traditional wound assessment, imaging tools provide reliable and noncontact measurements [73]. Imaging, especially 2D images, allows information to be retrieved quickly and provides time-efficient and objective metrics for wound evaluation, follow-up, and even to increase patient awareness.

Standard tools for wound assessment include digital images, 3D models, infrared imaging, ultrasound, and hyperspectroscopy. Each technology provides different complementary information for the evaluation. In this thesis, the focus is on the use of 3D models and infrared images.

Two-dimensional (2D) images

Two-dimensional images are the most widely used imaging tool in wound assessment. Obtaining them is cost-effective and easy thanks to digital cameras and even easier thanks to the ubiquitous availability of smartphones nowadays.

The basic 2D image acquisition procedure consists of taking an image from a sufficient distance taking care to clean the wound beforehand, and using adequate illumination. A ruler or other reference object should be included in the scene to provide correct measurements.

Digital imaging serves to document the visual characteristics in order to evaluate the evolution of the wound. Another way to use 2D imaging is to obtain metrics of the extent of the wound. Length, width, and perimeter, as well as 2D area, can be calculated from the images. In addition, several studies nowadays focus on the development of wound imaging wound segmentation algorithms and the classification of wound tissue types in order to objectively automate geometric wound measurements [103, 1, 76].

Despite its advantages, The accuracy of measurements obtained using simple techniques based on 2D imaging highly depends on the camera view. A large variability can be observed depending on the viewing angle, as previously noted [3]. The perspective effect and the curvature of the limb can cause significant measurement errors. In addition, the depth of the wound cannot be accessed by a simple image, while the healing process takes place in depth. [83, 24]. These limitations justified the three-dimensional approaches that have emerged subsequently.



Figure 1.1: Wound measurement from a 2D image using a commercial mobile application. Image obtained from [15].

Three-dimensional (3D) models

Three-dimensional models of the wound surface provide comprehensive information and improved visualization compared to two-dimensional images. First 3D models systems utilized complex devices inappropriate for clinical use. In the 2000s, photogrammetry promoted using 3D models with simple commercial cameras [91, 99].

While 3D models offer several advantages in wound assessment and monitoring compared to 2D imaging, there are also disadvantages: cost, complexity, time processing, and data storage. Recent advancements have made this technology more accessible and useful for healthcare professionals. A broader discussion on advantages and disadvantages of current 3D model systems are developed in Chapter 2.

Thermography

Thermography is another non-invasive tool that provides the surface temperature of the wound and skin. In chronic wound assessment, thermography is used to detect temperature changes that can indicate the presence of inflammation or infection [14, 27]. This information can guide treatment decisions, such as topical wound dressings or antibiotics.

The basic principle behind thermography is that the metabolic activity of living tissue generates heat, which infrared cameras can detect. In the case of chronic wounds, thermography can be used to identify areas of increased temperature that may indicate the presence of inflammation or infection.

Several studies show the value of thermography in chronic wounds, most of them using handheld devices and even, in some cases, using devices connected to smartphones. A summary of previous studies demonstrating that thermal metrics are the important metrics in wound assessment are listed and categorized in Table 1.1.

Table 1.1: Previous studies that have shown thermography to be useful for wound assessment, organized based on the portability of the system, whether smartphone-connected use is possible, and inclusion of 3D models.

Study	Portable Device	Smartphone-connected	Includes 3D modeling
Non Portable system			
Barone, Paoli, and RZIONALE [12]	No	No	Yes
Chang et al. [26]	No	No	Yes
Portable system			
Fierheller and Sibbald [35]	Yes	No	No
Bharara et al. [14]	Yes	No	No
Nakagami et al. [65]	Yes	No	No
Dini et al. [32]	Yes	No	No
Chaves et al. [28]	Yes	No	No
Chanmugam et al. [27]	Yes	No	No
Xue et al. [102]	Yes	Yes	No
Aliahmad et al. [5]	Yes	No	No

1.3 Wound evaluation metrics

1.3.1 Wagner grading system

The Wagner grading system is a straightforward and widely adopted wound classification system. The grading is based on the depth of the ulcer; the presence of osteomyelitis or gangrene; and the extent of necrotic tissue. According to this classification system, the condition of a wound can fall into one of 6 different stages:

- Grade 0: No wound.
- Grade 1: Superficial wound.
- Grade 2: Deep wound, extending to ligaments and muscles, but without bone involvement or abscess.
- Grade 3: Deep wound with cellulitis or abscess and often accompanied by osteomyelitis.
- Grade 4: Localized gangrene.
- Grade 5: Extensive gangrene involving the entire foot.

Fig 1.2 shows the schematic representation of this grading. Wagner wound grading system provides a representation of the natural progression of foot wounds. The grading system shows that wound status can flow from grade zero to grade five; and any grade up to grade four can be reversed to grade zero with appropriate treatment [97]. This wound grading system allows for a more systematic qualification of the wound status.

1.3.2 Evaluation regions

A comprehensive wound assessment involves not only the assessment of the wound itself but also the evaluation of the surrounding areas beyond the wound [33]. The assessment of these regions is important in the evaluation of a chronic wound. The following is a summary of the regions that are critical to assess and their significance in the comprehensive assessment of a chronic wound.

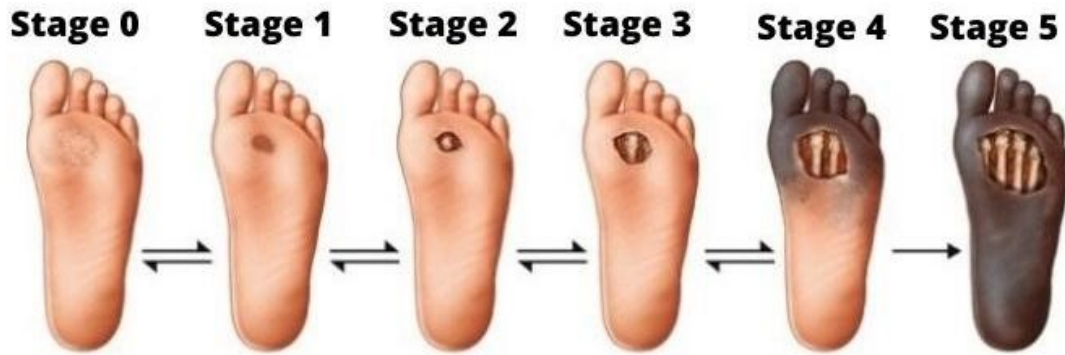


Figure 1.2: Wagner grading system obtained from [11]. The arrows represent the progression of chronic wounds. The wound can evolve from grade 0 to grade 5. Furthermore, wound stages can be reverted to grade 0 with proper care, except if the wound reaches grade 5.

Wound bed

Wound size and depth are important parameters to monitor over time. Wound size is obtained by 2D or 3D assessment. A 2D measurement, such as 2D length, width and area, can provide information about the extent of the wound, while a 3D assessment, such as 3D wound volume and area, can provide information about the depth of the wound.

Other characteristics that can be assessed on the wound bed include tissue type, perfusion, pH and exudate. These are briefly described below:

- **Tissue type:** The type of tissue present in the wound bed, such as granulation tissue, necrotic tissue, or slough, is evaluated to determine the stage of the healing process and to guide treatment decisions.
- **Perfusion:** blood flow to the wound bed is assessed to determine if tissue perfusion is adequate and to identify any problems that may affect healing.
- **Exudate:** the amount and type of wound exudate or discharge is assessed to determine the level of inflammation and the need for topical treatments.
- **pH:** the pH of the wound bed is assessed to determine the level of acidity or alkalinity and to identify any problems that may affect healing.

Wound edges

Assessment of the wound edges can provide information about wound healing by giving signs of wound contraction. Therefore, it is important to consider the color and texture of the wound edges during wound assessment.

Periwound

The periwound is the area of skin beyond the wound edges. Particularly, color, texture and temperature are important in the wound evaluation. The periwound can provide information about the presence of inflammation or infection and the extent of the wound [33]. Identification of areas of reduced blood flow in the periwound may be important for wound healing, as adequate blood flow is essential for proper healing. This information about the periwound can help guide treatment decisions.

1.3.3 Geometrical metrics

Common wound measurements include length, width, perimeter and wound surface 2D area and volume. Generally, length and width are defined by the main diameters measured manually or in images (see Figure 1.1). A rough approximation of the surface can be made from these two diameters by an ellipse model. Segmentation of the wound in the image provides a more accurate measurement. A single depth measurement (at the deepest point) provides a rough approximation of the volume by an ellipsoid model. Digital 3D models allow a more accurate evaluation of the volume without contact [4, 108].

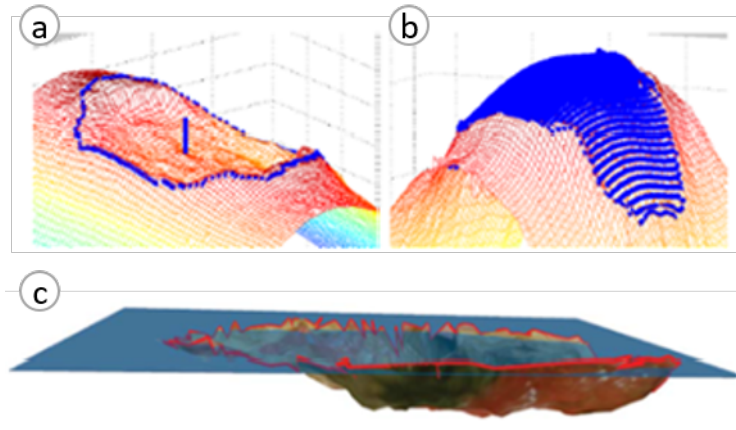


Figure 1.3: Illustration of 3D geometrical metrics: wound depth in (a) and wound volume in (b) and (c) estimated using different approaches. Images obtained from [108, 91].

1.3.4 Thermal metrics

Thermal imaging can help improve wound care [2, 14, 27, 28, 32, 35, 41, 82]. Thermal imaging metrics are obtained by manually selecting points of interest (POI) or a region of interest (ROI) within an evaluation region. Both the ROI and POI are typically defined manually and subjectively. A ROI is typically a square region within the wound and periwound area. ROIs can provide much more information than POI, enabling summary metrics such as mean temperature, and standard deviation of the temperature. Fig 1.4 illustrates a manual and subjective selection of two ROIs within the wound bed and the periwound.

Temperature metrics are derived from combining measurements of temperature at different ROIs or POIs located in different areas of interest, i.e. wound bed, edges, periwound. The most common metrics are temperature differences between these regions of interest; however, other metrics, such as temperature variability, have also been proposed and studied.

Most studies point out that the temperature difference between zones can be a useful indicator in chronic wound monitoring [28, 27, 35, 65, 26]. The metrics are obtained typically by comparing mean temperatures in regions of interest for wound assessment: wound, periwound, and reference temperature. A difference of the maximum relative temperatures between regions has also been performed in [27].

Another temperature metric that has been tested is thermal variability [26]. The variance of the temperature of the wound bed, which was segmented semi-automatically, was analyzed. In [5], areas with isometric temperatures were used to delineate. Wound area was defined from the isothermal areas of the thermal images and it was determined that the ratio of isothermal areas between the first two weeks and the first visit was useful in distinguishing between healing and nonhealing ulcers in diabetic feet.

Table 1.2 provides a summary of the studies that analyzed thermal metrics classified according to the type of thermal metric used.

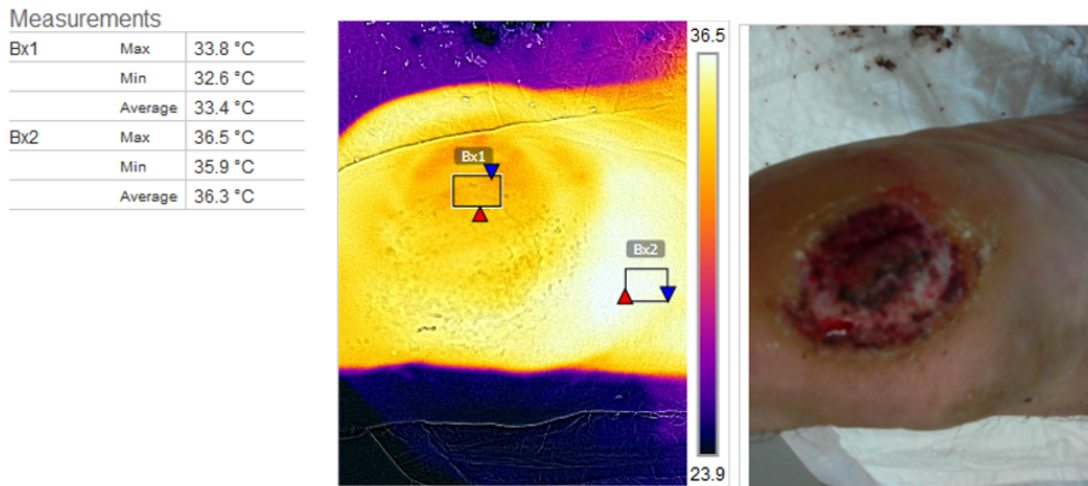


Figure 1.4: Example of manually selected ROIs in the wound and periwound; as well as the thermal measurements obtained for each ROI.

Table 1.2: Previous studies where thermal metrics were studied for wound evaluation or monitoring, classified by type of thermal metrics analyzed.

Study	Temperature differentials	Temperature variability	Others
Chaves et al. [28]	X		
Chanmugam et al. [27]	X		
Fierheller and Sibbald [35]	X		
Nakagami et al. [65]	X		
Chang et al. [26]	X	X	
Barone, Paoli, and Razionale [12]			X
Aliahmad et al. [5]			X

Finally, Table 1.3 shows a list of the reviewed studies using either 3D modeling or thermography for wound assessment. As can be seen, the majority of studies have focused on the 3D model; and only a few studies have studied the combination of thermography and 3D models for wound assessment.

Table 1.3: Previous studies where either thermography, or 3D models were analysed for wound assessment.

Study	3D models	Thermography
Shah, Wollak, and Shah [83]	X	
Shamata and Thompson [85]	X	
M. C. Barbosa, Carvalho, and Gomes [59]	X	
Jørgensen et al. [47]	X	
Treuillet, Albouy, and Lucas [91]	X	
Zenteno et al. [107]	X	
Yee, Harmon, and Yi [106]	X	
Parvizi et al. [72]	X	
Stockton et al. [88]	X	
Zvietcovich et al. [108]	X	

Study	3D models	Thermography
Lasschuit, Featherston, and Tonks [54]	X	
Lu et al. [58]	X	
Mamone et al. [60]	X	
Fierheller and Sibbald [35]		X
Nakagami et al. [65]		X
Dini et al. [32]		X
Chaves et al. [28]		X
Chanmugam et al. [27]		X
Xue et al. [102]		X
Aliahmad et al. [5]		X
Bharara et al. [14]		X
Barone, Paoli, and Razionale [12]	X	X
Chang et al. [26]	X	X
Mirabella et al. [62]	X	X

1.4 Discussion

Traditional wound assessment methods that do not require specialized equipment are practical and can be easily performed in many cases. However, relying on a subjective, note-taking approach can result in inaccuracies and lead to suboptimal treatment, prolonging the patient’s healing process. On the other hand, image-based diagnostic tools are simple to obtain and provide great value at a low cost. Physicians are increasingly incorporating 2D imaging into routine wound documentation for follow-up purposes. Although more effort is required to organize the images and extract metrics from them, using computer vision and artificial intelligence helps automate the process, enabling rapid and timely measurement.

The 3D models provide a complete and accurate representation of the wound, including its depth and shape. This can help healthcare providers to more accurately evaluate the healing process and determine the best course of treatment. Additionally, 3D models can be rotated and viewed from different angles, providing a more comprehensive understanding of the wound than is possible with 2D images, which is very useful for telemedicine. However, using 3D models for wound assessment also has some limitations. Obtaining 3D images may be more time-consuming and resource-intensive than obtaining 2D images. The use of three-dimensional models as documentation tool is not widespread, as expensive equipment systems and complex setup can hinder their application in clinical settings.

Even though 3D models provide much more comprehensive information than 2D imaging, the complex setup and cost of equipment prevent its widespread use. Nevertheless, technological advances have moved towards creating three-dimensional models using more portable and affordable devices than before, such as portable laser scanners, commercial scanners, and, more recently, smartphones.

Several previous studies have shown that thermal measures are related to inflammation and infection. Differences between evaluation regions are commonly highlighted as useful metrics for wound evaluation. Other measurements, such as temperature variability, have also been proposed, but few studies have been performed on its utility.

One of the weaknesses of 2D thermal imaging analysis is the selection of the region of interest within regions of evaluation, i.e., wound bed, periwound, and normal skin. The regions of interest within evaluation regions are defined manually, which is subjective and depends on the clinician.

1.5 Conclusion

In this chapter, we introduce chronic wounds and wound assessment. Wound assessment is performed traditionally with manual measurement methods, which provides subjective and limited information for wound evaluation over time. In contrast, imaging tools can help reduce the shortcomings of traditional assessment. Imaging tools provide comprehensive information that can lead to objective assessment metrics, which in turn leads to a systematic approach to treatment.

Specifically, three-dimensional models offer a data structure that provides comprehensive information for assessing and monitoring wounds over time. Metrics obtained from 3D models are more informative, reliable, and accurate than 2D metrics. Moreover, the most recent technology allows 3D model creation with straightforward acquisition and low-cost equipment.

Thermography, on the other hand, provides complementary information and could be obtained at a low cost, given current technology. Thermal metrics are often obtained from manually defined regions of interest within evaluation regions, which are subjective and lead to inter-observer variability. Therefore, a robust definition of evaluation regions in wound assessment is required. For this, thermal information should be registered to visual information, and regions of interest such as wound, periwound, and normal skin could be objectively defined to obtain objective and automated metrics from thermography.

Chapter 2

Three dimensional modeling

Contents

2.1 3D modeling definitions	13
2.2 3D acquisition systems applied to wounds	14
2.3 Basics of 3D Computer Vision	17
2.4 Structure from Motion (SfM)	21
2.5 Conclusion	23

A 3D model is a digital representation of an object. In this chapter, we introduce the concept of three-dimensional modeling and explore related 3D computer vision concepts and methods. These topics are essential to understanding the research presented in the following chapters of this thesis. We assume that readers have a basic understanding of computer vision; otherwise, more information can be found in [90].

This chapter is structured as follows: First, the section 2.1 introduces commonly used objects for 3D modeling. The section 2.2 describes existing reconstruction approaches and gives an overview of current systems used for 3D wound modeling and measurement. In the section 2.3, we provide an overview of the fundamental concepts of 3D computer vision that are relevant to our research. In the section 2.4, the Structure from Motion (SfM) algorithm is detailed and its applications on wounds are reviewed.

2.1 3D modeling definitions

For modeling the skin or wound surface various 3D model can be used. In the following, 3D models that can help represent the surface of the skin are presented

3D Point Cloud

A 3D point cloud is a collection of points in 3D space. Mathematically, a 3D point cloud is composed by a set of points $\mathbf{P} = \mathbf{p}_1, \mathbf{p}_2, \dots, \mathbf{p}_n$, where the position of each point in 3D space is defined by its x, y, and z coordinates, each point $\mathbf{p}_i = [x_i, y_i, z_i]^T$ is a vector in 3D space.

3D Mesh

A 3D point cloud can be converted into a triangulated 3D mesh by connecting its points to form lines, which in turn can be connected to form triangular polygons, representing the surface of the object. The lines connecting the points can be represented as a set of edges, where each edge connects two points and is defined as a pair of indices (i, j) such that $(\mathbf{p}_i, \mathbf{p}_j)$ is an edge. Triangles are a set of faces, and each face is defined as a set of indices (i, j, k) corresponding to the vertices forming the triangle with points $(\mathbf{p}_i, \mathbf{p}_j, \mathbf{p}_k)$.

To enhance the realism of the 3D model, texture can be added to the triangular faces of the mesh, which can include adding color and patterns. In this thesis, textured meshes are used as for 3D visualization to provide a more realistic and detailed appearance. Figure 2.1 depicts three types of 3D models which will be used throughout this thesis to help represent the surface of the skin.

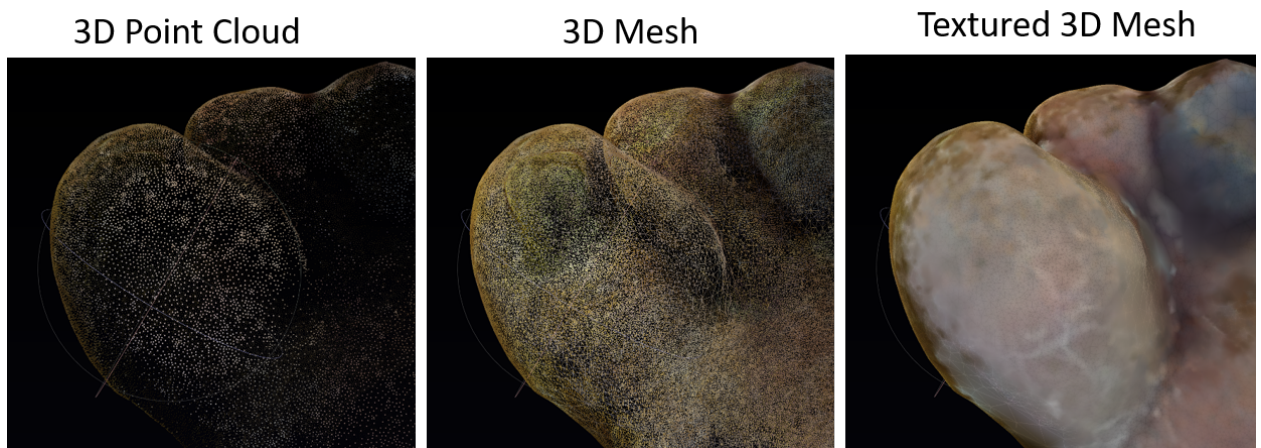


Figure 2.1: Illustration of types of 3D models for surface modeling of a toe. Images based on our own data collection.

2.2 3D acquisition systems applied to wounds

In this section we review the different systems used in previous studies for wounds. The aim is to analyze the advantages and limitations of 3D modeling systems when used for obtaining 3D models of wounds and wound evaluation measurements.

There are two approaches to the creation of three-dimensional models: active and passive triangulation.

1. Active triangulation

Active 3D reconstruction is achieved by using a sensor and an emitter, such as a laser scanner, that emits a beam of light and measures the time it takes for the beam to travel to the surface and bounce back. From these measurements, the distance of each point on the surface can be calculated by triangulation, and a 3D point cloud can be generated. Common active reconstruction devices are: laser scanners, structured light systems, RGB-D sensors, and recently, time-of-flight cameras.

Active 3D triangulation is commonly used in industrial and building inspection; robotics; and medical imaging, where precise and accurate 3D information is required. The main advantage of active 3D triangulation is that it provides highly accurate measurements, even in challenging environments, such as those with poor lighting or occlusions; however, it is typically more costly and time-consuming than passive 3D triangulation, and might require specialized equipment.

2. Passive triangulation

Passive 3D reconstruction is a method for creating 3D models from 2D images captured by a camera, without the use of any emitting signal. The 3D points triangulation is computed from a set of matching projections on images of the scene from different point of view.

One advantage of passive 3D reconstruction is that it can be performed using a single camera, making it an widely accessible solution for many applications. However, there are also limitations to passive 3D reconstruction, such as reconstruction problems on surfaces with no texture or reflective surfaces, and a reduced accuracy compared to models created using active reconstruction methods.

All in all, passive 3D reconstruction has advantages such as being non-invasive, low-cost, and easy to use. However, it also has limitations such as limited accuracy, requiring multiple images, clear visibility, and good lighting conditions.

3D acquisition systems for wounds

Nowadays, various acquisition systems are proposed to create 3D models based on either active or passive triangulation. Below is an overview of the most commonly used acquisition systems for 3D model acquisition of wounds:

Laser scanners

Laser scanners utilize active reconstruction to achieve accurate 3D modeling of wounds. Laser scanners can be highly accurate but also expensive and expensive and cumbersome to operate for clinicians [77]. Therefore, this technology is commonly used as a benchmark in evaluating new 3D modeling systems. Laser scanner 3D measurements obtained in a study demonstrated higher inter-rater and intra-rater consistency, compared to traditional gel injection [108].

Recent advances have taken advantage of handheld laser scanners to obtain three-dimensional wound measurements; however, their use is limited to a stationary mode without handheld acquisition. [107, 108].

Structured light systems

Structured light systems employ active triangulation to generate three-dimensional (3D) models. Compared to laser scanners, structured light systems tend to be more affordable. However, the obtained 3D models require additional software for processing.

Disadvantages of the structured light methodology include inaccurate outcomes when dealing with reflective surfaces, like for example, moist surfaces in open wounds. This type of systems are commonly proposed for wound evaluation, and previous studies have demonstrated that 3D measurements, are accurate and better than those obtained from manual measurements. [85, 74, 48, 84]

RGB-D Cameras

RGB-D camera systems, which include depth sensors, can be a suitable alternative for wound assessment. In [36], they tested a popular and commercial device for obtaining RGB-D images and creating 3D models, the Microsoft Kinectv2, and other similar devices PrimeSense Carmine, Orbbec Astra. They found that this type of systems can provide accurate calculation of volume, area, and perimeter, with results similar to those obtained from laser scanning. Moreover, in [31], they used a device similar to the Microsoft Kinect to obtain RGBD images to create 3D models of

wounds. The device was portable and attached to a tablet. They found that the 3D wound surface obtained with their system had less than a 4% difference compared to measurements obtained with laser scanners. RGB-D cameras offer an affordable solution, and some of them can be portable. However, they can be complex to operate for a clinician, who is not necessarily familiar with this type of devices.

Commercial 3D imaging systems for wounds

Commercially available systems, typically composed of hardware and software, provide 3D modeling and visualization. Most well known systems are listed below:

- Eykona (Fuel 3D, Los Angeles, United States) [34]
- InSight (eKare Inc., Fairfax, VA, United States) [44]
- WoundVision (Indianapolis, Indiana, United States) [100]
- Silhouette camera (Aranz, Christchurch, New Zealand) [86]
- LifeViz 3D system (Quantificare S.A., Valbonne, France) [57]

Table 2.1 provides a description of the commercial systems based on proprietary devices, which can be depicted in Figure 2.2.

Table 2.1: Commercial systems based on proprietary hardware and software for wound imaging.

System	Equipment	Functionalities
Eykona [34]	Proprietary device	2D/3D measurements
InSight [44]	Occipital sensor (proprietary device [89]), Only available for iPad	2D/3D measurements
WoundVision [100]	Proprietary device, includes a laser beam	2D measurements. Multimodal: Color and infrared data
Silhouette [86]	Proprietary device, laser-assisted device	2D/3D measurements
LifeViz 3D system [57]	Proprietary device, includes dual laser beam + light projector	3D visualization, 3D measurements

These commercially available 3D imaging systems are mainly based on structured light technology to generate high-resolution 3D models of wounds. Most notably, all commercial systems are based on portable hardware and allow freehand acquisition.

As commercial system include proprietary hardware and software, and clinicians will require time to be trained on the tool. Hence, the cost of training, in addition to the cost of hardware, software and upgrades, is a disadvantage for the usage of commercial systems.

In summary, acquisition systems have been widely used for wound modeling. However, they are typically expensive or require training due to the complexity of their handling. In contrast, passive 3D reconstruction, usually based on multi-view digital images, is known to have a reduced accuracy compared to active reconstruction methods; however, it has the great advantage of being low cost, and does not require specialized equipment since it can be done with any digital camera.

In the subsequent section of this chapter, we review the structure-from-motion algorithm and its potential application in wound evaluation. Prior to dig into this topic, we will give a review of the basic concepts of 3D computer vision necessary for this thesis and for a better understanding of the Structure from Motion algorithm.



Figure 2.2: Commercial systems based on proprietary hardware and software.

2.3 Basics of 3D Computer Vision

Triangulation is the process of determining the 3D position of a point from its projections on multiple images. The basic idea is to use the relative positions of the cameras to find the 3D position of the point in the world coordinate system. The following is an introduction to the basic concepts required for 3D point triangulation, as well as the methods used to work with 3D models that will be used in later chapters.

Camera reference frame

The camera reference frame refers to a coordinate system used to describe the position and orientation of a 3D space. The camera reference frame is typically centered at the camera's optical center. The reference frame is usually defined with the x-axis pointing to the right, the y-axis pointing downwards, and the z-axis pointing outwards from the camera lens. (See Figure 2.3)

The camera reference frame is important in computer vision, as it provides a standard coordinate system that can be used to represent the position and orientation of objects from camera's view.

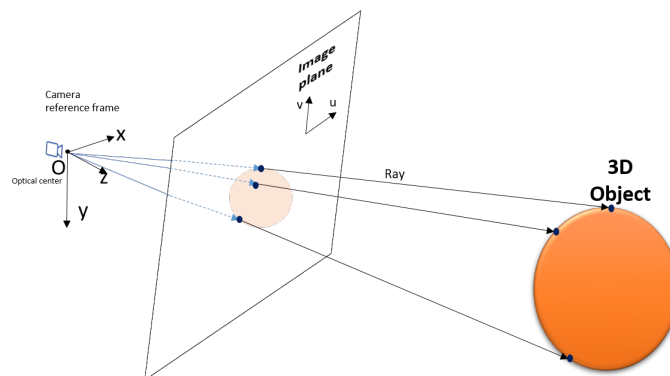


Figure 2.3: Illustration of the camera reference frame, the image plane and the 3D object.

The image plane is the 2D plane where the camera's image sensor or film is positioned and captures an image of the scene in front of it. The image plane is where the 2D image is formed, and it is typically represented by a flat surface as seen in Figure 2.3.

2.3.1 Camera calibration

Camera calibration is the process of determining the intrinsic and extrinsic parameters of a camera, including its optical properties, position and orientation relative to the scene being captured. The intrinsic parameters describe the internal characteristics of the camera such as focal length, principal point, and distortion coefficients. The extrinsic parameters describe the position and orientation of the camera in the world coordinate system.

The intrinsic parameters are represented by a 3×3 camera intrinsic matrix K , where the elements of the matrix represent the focal length (f_x and f_y), the principal point (c_x and c_y), and skew (s). The intrinsic matrix can be represented as follows:

$$K = \begin{bmatrix} f_x & s & c_x \\ 0 & f_y & c_y \\ 0 & 0 & 1 \end{bmatrix}$$

The skew parameter will be zero for most normal cameras. However, in certain unusual instances it can take non-zero values. [40]

The extrinsic parameters can be represented by a 3×4 camera extrinsic matrix R and a 3×1 translation vector t , which describe the rotation and translation of the camera with respect to the world. The extrinsic matrix can be represented as follows:

$$M_{ext} = [R|t] = \begin{bmatrix} R_{11} & R_{12} & R_{13} & t_1 \\ R_{21} & R_{22} & R_{23} & t_2 \\ R_{31} & R_{32} & R_{33} & t_3 \end{bmatrix} \quad (2.1)$$

Camera calibration is typically performed by capturing images of a special calibration pattern, such as a checkerboard pattern, from different viewpoints. The accuracy of the camera calibration depends on the quality of the calibration pattern, the number of images taken, and the accuracy of the corner detection algorithm used to detect the pattern in the images.

The projection of points from the 3D world frame to a 2D image plane requires the usage of intrinsic and extrinsic matrices as shown in Figure 2.4.

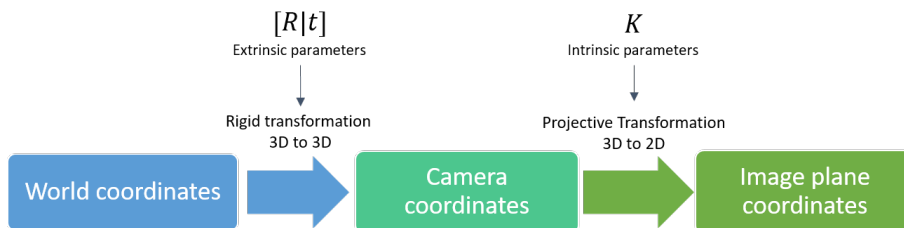


Figure 2.4: Projection of 3D points from the world frame into the image plane.

Both intrinsic and extrinsic matrices are assembled into a single matrix called the camera projection matrix defined below.

Camera projection matrix

The camera matrix or projection matrix is a 3×4 matrix that provides the mapping from 3D points in the world to 2D points in an image. Then, the projection of a 3D point P onto 2D camera plane is given by:

$$P = K[R|t] = \begin{bmatrix} f & 0 & c_x \\ 0 & f & c_y \\ 0 & 0 & 1 \end{bmatrix} \begin{bmatrix} r_1 & r_2 & r_3 & t_1 \\ r_4 & r_5 & r_6 & t_2 \\ r_7 & r_8 & r_9 & t_3 \end{bmatrix} \quad (2.2)$$

where K is intrinsic matrix and $[R|t]$ the extrinsic matrix.

Perspective Projection

Given a 3D point $X = [X_w, Y_w, Z_w]^T$, to transform P in the world coordinates to image pixel coordinates x , the perspective projection is used as follows:

$$x = PX = K[R|t]X = \begin{bmatrix} f & 0 & c_x \\ 0 & f & c_y \\ 0 & 0 & 1 \end{bmatrix} \begin{bmatrix} r_1 & r_2 & r_3 & t_1 \\ r_4 & r_5 & r_6 & t_2 \\ r_7 & r_8 & r_9 & t_3 \end{bmatrix} \begin{bmatrix} X_w \\ Y_w \\ Z_w \\ 1 \end{bmatrix} \quad (2.3)$$

Triangulation

Triangulation is mathematically described as follows: Let P_1 and P_2 be the projection matrices for two cameras that observe the same 3D point X , and let x_1 and x_2 be the corresponding 2D projections of X in the two images (Figure 2.5). The relationship between X , P_1 , and x_1 can be represented as:

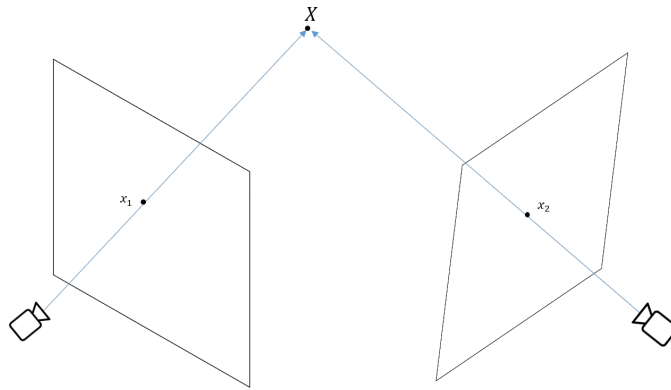


Figure 2.5: Illustration of triangulation of a point from points matched in two 2D images.

$$x_1 = P_1 X \quad (2.4)$$

Similarly, the relationship between X , P_2 , and x_2 can be represented as:

$$x_2 = P_2 X \quad (2.5)$$

To find the 3D position of $X = [X_1, X_2, X_3, X_4]$, a linear system of equations is set up stacking the two equations and solving for X :

$$\begin{bmatrix} x_{1,1} & x_{1,2} & x_{1,3} & 1 \\ x_{2,1} & x_{2,2} & x_{2,3} & 1 \end{bmatrix} \begin{bmatrix} X_1 \\ X_2 \\ X_3 \\ X_4 \end{bmatrix} = \begin{bmatrix} x_{1,1} & x_{1,2} & x_{1,3} \\ x_{2,1} & x_{2,2} & x_{2,3} \end{bmatrix} \begin{bmatrix} P_{1,1} & P_{1,2} & P_{1,3} & P_{1,4} \\ P_{2,1} & P_{2,2} & P_{2,3} & P_{2,4} \\ P_{3,1} & P_{3,2} & P_{3,3} & P_{3,4} \end{bmatrix} \quad (2.6)$$

Bundle adjustment

Bundle Adjustment is an optimization technique for simultaneously refine the 3D structure of a scene and the camera parameters from a set of matched points in images.

The goal of bundle adjustment is to minimize the reprojection error between the observed 2D points and their estimated projections in the image plane. Given a set of N images, each with a set of m_i corresponding 2D points in the image plane, and the initial estimates for the 3D positions of the points and the camera parameters. The reprojection error is defined as the sum of squared distances between the observed 2D points (x_{ij}) and their estimated projections(\hat{x}_{ij}):

$$E = \sum_{i=1}^N \sum_{j=1}^{m_i} |x_{ij} - \hat{x}_{ij}|^2 \quad (2.7)$$

where x_{ij} is the j th observed 2D point in the i th image, \hat{x}_{ij} is the estimated projection of the corresponding 3D point in the image plane, and m_i is the number of points in the i th image.

The optimization is solved by simultaneously updating the 3D points and camera parameters in order to minimize the reprojection error.

Bundle adjustment is a crucial step in 3D computer vision algorithms like structure from motion (SfM) and simultaneous localization and mapping (SLAM)

2.3.2 Computer Graphics

Raycasting

Raycasting is useful to find the corresponding between pixels in the image and vertices on the 3D model [95]. From this correspondence, pixel values, like temperature, on 2D images can be assigned to 3D model vertices. This methodology is useful, for example, for mapping 2D thermography values to 3D models once the thermal camera pose is known.

Raycasting consists of casting a “ray”, i.e. a straight line from the camera’s point of view, in a given direction, and checking whether it crosses any object or surface in the scene. This process is performed for each pixel in the image, resulting in the correspondence between the pixels and the vertices of the 3D model. Figure 2.3 represents the rays coming from the optical centers of the camera and their association with the 3D model.

Rasterization

Rasterization is a method commonly used in computer graphics and virtual reality to create 2D images from 3D models. The rasterization process referred to in this thesis refers to polygon rasterization, which is used to convert a triangular 3D mesh into 2D images.

Rasterization involves projecting the triangles of a 3D model onto a 2D image plane, followed by determining which pixels fall inside or on the boundary of the triangle, and computing the color of each pixel based on the triangle’s properties and position. Figure 2.6 illustrates the rasterization of a single triangle projected onto a 2D image plane. The process of determining which pixels are covered by the polygon is known as triangle rasterization. Triangle rasterization identifies which pixels fall inside or on the boundary of the triangle, and then computes the color of each pixel

based on the triangle's properties and position. This is typically accomplished using techniques such as scanline or barycentric coordinate interpolation algorithms [70].

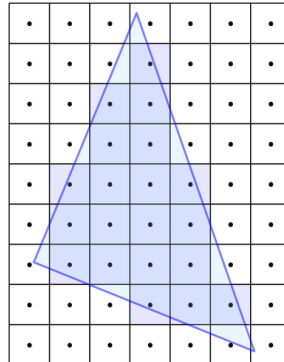


Figure 2.6: Illustration of the rasterization of a triangle into a 2D image pixel plane. [Martin Kraus, Pixels covered by a triangle, CC BY-SA 3.0](#)

2.4 Structure from Motion (SfM)

Structure from Motion (SfM) is an algorithm to create 3D structure from multiple 2D images, i.e. it is a passive reconstruction method. The Structure from Motion algorithm is a well-known algorithm used for 3D reconstruction from multiple views. SfM creates point clouds from features found in multiple 2D images. To do this, distinctive features are identified in the 2D images and the correspondences between them are mapped. It's implementation requires using linear algebra, optimization techniques, and computer graphics algorithms.

SfM is convenient 3D reconstruction algorithm as it requires only a digital camera to capture multiple view images with overlapping scenes. The digital camera could be a smartphone camera, and the acquisition does not require to be controlled, i.e. it can be done in handheld mode. Moreover, open-source software with friendly user interface are already available to create 3D models with SfM; for example, Meshroom, 3DF Zephyr, Colmap, and VisualSfM. This attribute makes SfM an attractive solution for wound evaluation, particularly since it has the potential to enable remote assessments.

In particular, Meshroom provides an open source implementation with friendly user interface [6] besides to capabilities for running its pipeline from command line. Thus, it allows for an automated and customized implementation. Figure 2.7 shows the stages of a general SfM reconstruction performed in Meshroom.

These stages are briefly described below:

1. Feature Extraction: In this stage, distinctive features are identified in 2D images using state-of-the-art algorithms such as SIFT, AKAZE, Brute Force, etc.
2. Feature Matching: Features detected in the 2D images are matched to each other. Feature descriptors are used to assess the similarity between images and the nearest neighbor algorithm is applied to map the correspondence between the features. Outliers are removed through robust matching with RANSAC.
3. Structure from Motion (SfM): The core of the process is the SfM algorithm. Two images with a large number of coincidences features are selected at random, and the origin of the 3D world is fixed at the pose of the first camera. Features are then triangulated in 3D, and the

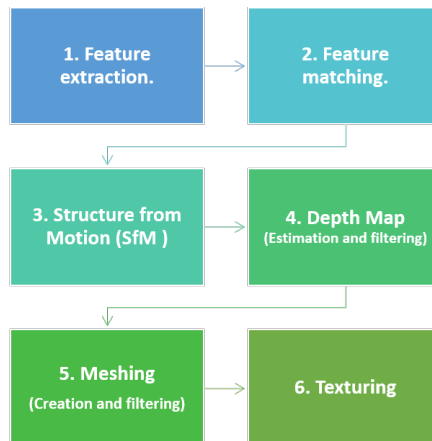


Figure 2.7: General 3D SfM reconstruction pipeline implemented in Meshroom, a well-known open source software for passive 3D reconstruction.

process repeats iteratively by selecting an image with matching features to triangulate new 3D points. In each iteration, bundle adjustment is applied to refine the camera's intrinsic and extrinsic parameters.

4. Depth Maps: With the point clouds and cameras found from the previous SfM algorithm, depth images are generated using the Semi-Global Matching (SGM) algorithm.
5. Meshing: Octrees are created from the depth maps and a 3D Delaunay tetrahedralization is performed. A Laplacian filter is applied to obtain a smooth 3D mesh.
6. Texturing: A technique UV texturing is used to add texture to the surface of the 3D model. Multiview images are fused based on state-of-the-art algorithms [55]. Then UV mapping is performed, where a 2D image, called the texture map, is mapped to the surface of the 3D model. The texture map is created by wrapping the texture around a flat representation of the 3D model and aligning the texture with the geometry of the model.

While SfM has proven to be an effective tool in chronic wound evaluation, it does have some limitations that need to be addressed. One such limitation its lower accuracy when it comes to volumetric metrics, compared to active reconstruction systems. Despite this, SfM remains a valuable tool in chronic wound evaluation, as evidenced by various studies:

Previous studies have indicated that SfM reconstruction can produce 3D models and metrics useful in wound evaluation. In [91], solely a pair of images from uncalibrated cameras was used to create 3D models of wounds. They found an average difference on volume of $0.52cm^3$ with a relative error of 0.43; and a maximum error on volume estimation of less than $1.25cm^3$, for 16 cases of wounds with a mean volume of $39.12cm^3$. In [99], multi-view 3D reconstruction from uncalibrated images was used. Comparison to an industrial 3D scanner, showed an average error of 1.3% with a precision of 3% for volume measurement.

In [25], Structure from Motion was performed using video frames with successful results. Resulting 3D models were compared to a laser scanner and a mean distance between registered 3D models was found to be less than $0.8mm$, with a root mean square error (RMSE) less than $0.55mm$. The evaluation was done on a cork phantom of $3cm$ of diameter and two leishmaniasis wounds of $1cm$ and $2cm$ diameter.

In another study, [107] has found that 3D point clouds created with SfM in an open-source software (VisualSFM) have a mean distance of $0.36mm$ when compared to 3D models obtained from laser scanners. Absolute error on the volume estimation was found to be in average $33.68mm^3$ or 19.84% for six wound followed over 4 weeks, with variable wound sizes from $2.53mm^3$ to $1214.5mm^3$.

Nevertheless, the volume evolution over 4 weeks shows the same trend as the volume evolution obtained with a laser scanner.

In [59], 3 artificial wounds were analyzed with sizes of 4.79cm², 36.97cm² and 29.47cm². Wound surface area errors were evaluated when using 2, 3, 5, and 10 images, and they found errors of 12.47%, 8.5%, 6.6% and 3.8%, which is less than the average error found when using 2D images: 32.7. Their results suggest that larger number of images can lead to reduced errors; however, larger number of images also require larger computational resources as computational cost lies in the order of $O(n^2)$.

More recently, [80] evaluated volume and other 3D measurements, by using SfM in a commercial software, Agisoft Photoscan. They found high intra-rater and inter-rater reliability, with Intraclass Correlation Coefficient (ICC) values greater than 0.98 and 0.99 respectively.

All in all, the use of SfM in wound evaluation has gained significant attention in recent years, and for good reason. Evidence suggests that SfM is a promising tool for accurately assessing wounds. While there have been some accuracy errors reported for SfM on volume estimation, the majority of studies have reported errors of less than 10%. Additionally, SfM appears to be a better, more informative, and accurate tool for measuring surface area than 2D imaging.

Interestingly, previous studies suggest that the accuracy of SfM could be further improved with a larger number of images, and computational costs can be managed if processing is done on a server. What's more, current research is even exploring the possibility of processing SfM entirely on smartphones. For instance, [69] exposes an SfM-based algorithm that can run completely on smartphones.

2.5 Conclusion

In this chapter, the fundamental concepts of 3D computer vision are introduced which will be utilized later in Chapter 5. Specifically, techniques such as raycasting, perspective projection, and rasterization are introduced.

This chapter also discusses two approaches to 3D reconstruction, namely active and passive. Although active reconstruction is very accurate, the necessary acquisition equipment is expensive. On the other hand, passive reconstruction, particularly structure-based reconstruction from motion, although less accurate, has demonstrated its potential for wound assessment. Several studies have found that SfM can enable obtaining volumetric measurements similar to those obtained with laser scanners. Moreover, wound surface area obtained using SfM is more accurate than area measurements using 2D imaging.

Open-source software, user-friendly and accessible is available for creating 3D models. However, the challenge with SfM reconstruction is that it demands significant computing power. This challenge can be overcome by performing 3D reconstruction offline, on desktop computers or on cloud servers.

In conclusion, multiple studies highlight the feasibility of SfM for providing 3D models for chronic wound assessment and obtaining 3D measurements. Although the accuracy of measurements obtained by passive reconstruction with SfM may not be as high as those obtained by laser scanning, these studies demonstrate that SfM still provides reliable indicators similar to those of laser scanners, and better than those obtained with 2D imaging, making it a useful tool for wound assessment.

Chapter 3

Two dimensional thermography

Contents

3.1 Physics of infrared radiation	24
3.2 Thermography	27
3.3 Accuracy of thermal imaging systems	32
3.4 Conclusion	33

Thermal imaging or thermography consists in detecting infrared radiation emitted from an object and convert it to temperature. Thermography provides indicators that are not visible to human eyes, providing complementary information to color images in various applications.

Thermography is used in different fields; most of them in: medicine, buildings and security. In buildings, it can be used for inspections: for checking temperature insulation of a house, for locating damaged pipes, or to detect infestations. In the field of security, thermography is used to confirm and validate the presence of people or animals in a given place. For example, to identify people at frontier crossings, and to verify the intrusion of people or animals in rural or remote areas.

Several thermography devices are currently available, and it is useful to know how they work in order to choose a suitable one for your wound application. In the medical context, it has been reported to be used to detect the presence of inflammation, irregular blood flow and even some cancers such as malignant melanomas [21, 82, 94]. It is also used in the exploration of the body's response to alternative procedures, such as the response to massage or the response to exercise in a particular part of the body [78, 94]

This chapter introduces the basics of infrared radiation and thermal cameras. Special attention is given to the accuracy of low-cost portable thermal cameras, as they are quite practical devices for our clinical application.

This chapter is structured as follows: First, Section 3.1 introduces the basic concepts on physics of infrared radiation. Next, Section 3.2 introduces thermal imaging, and particular focus is given to portable low-cost thermal devices. Then, Section 3.3 reviews the sources of errors on the temperature estimation from thermography. Finally, conclusions are given in Section 3.4.

3.1 Physics of infrared radiation

All physical objects constantly emit electromagnetic radiation. Electromagnetic radiation consists of waves that propagate through space and carry energy.

Electromagnetic radiation waves are of different wavelengths. Wavelengths can be large, longer than a continent, up to short wavelengths, smaller than the nuclei of atoms. All the diversity of waves constitute the electromagnetic (EM) spectrum (See Figure 3.1)

Within the EM spectrum, the range of wavelengths between 380 nm and 750 nm are detected by the eye, and this part of the EM spectrum is called visible spectrum.

The infrared (IR) spectrum is composed of wavelengths between $0.75 \mu\text{m}$ and $15 \mu\text{m}$. Fig. 3.1 depicts the EM spectrum with a focus on the visible spectrum and the IR spectrum.

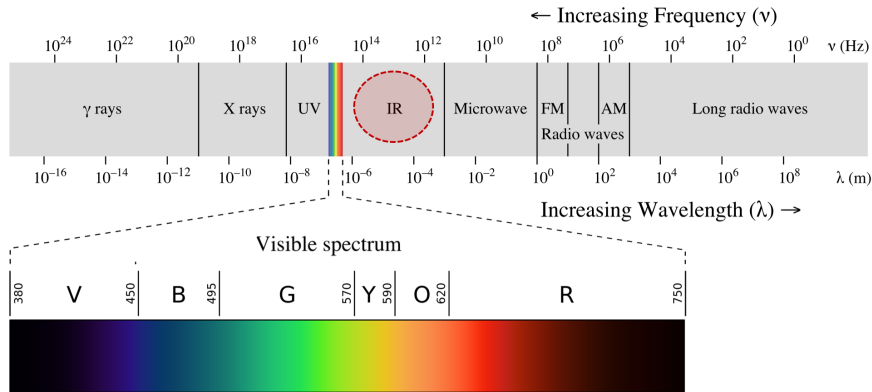


Figure 3.1: Electromagnetic waves and the visible part of the electromagnetic spectrum. Image created by Philip Ronan, Gringer, [EM spectrum revised](#), highlighted IR spectrum by Evelyn Gutierrez, CC BY-SA 3.0

3.1.1 History of infrared

The discovery of the infrared radiation was made by Herchel in 1800 while researching different optical filters to improve the telescopes of the time. While performing experiments with the classical Newton prism, he identified increased temperatures in areas beyond the red region of the visible spectrum where no colour was visible. This radiation, initially called “dark heat” or “invisible radiation”, was then called “infrared radiation”.

Fig. 3.2 illustrates the newton prism experiment and temperature measurements in 3 different zones. The temperature in the region beyond the red zone, not visible to the eye (bottom), has a higher temperature than the zones where visible red light is reflected (center) or another zone below the violet rays where no radiation is supposed to reach (top).

3.1.2 Basic concepts

Infrared spectrum

The Infrared (IR) spectrum is subdivided in 4 categories according to the wavelength of the IR radiation:

- Near infrared (NIR): Wavelengths are between $0.5 \mu\text{m}$ to $1 \mu\text{m}$.
- Short-Wave infrared (SWIR): Wavelengths are between $1 \mu\text{m}$ to $2.7 \mu\text{m}$.
- Mid-Wave infrared (MWIR): Wavelengths are between $3 \mu\text{m}$ to $5 \mu\text{m}$.
- Long-Wave infrared (LWIR): Wavelengths are between $8 \mu\text{m}$ to $14 \mu\text{m}$.

Blackbody

In physics, a blackbody or black body is an ideal object that absorbs all the radiation that it receives without any reflection, diffusion neither absorption. At a given temperature, it emits a

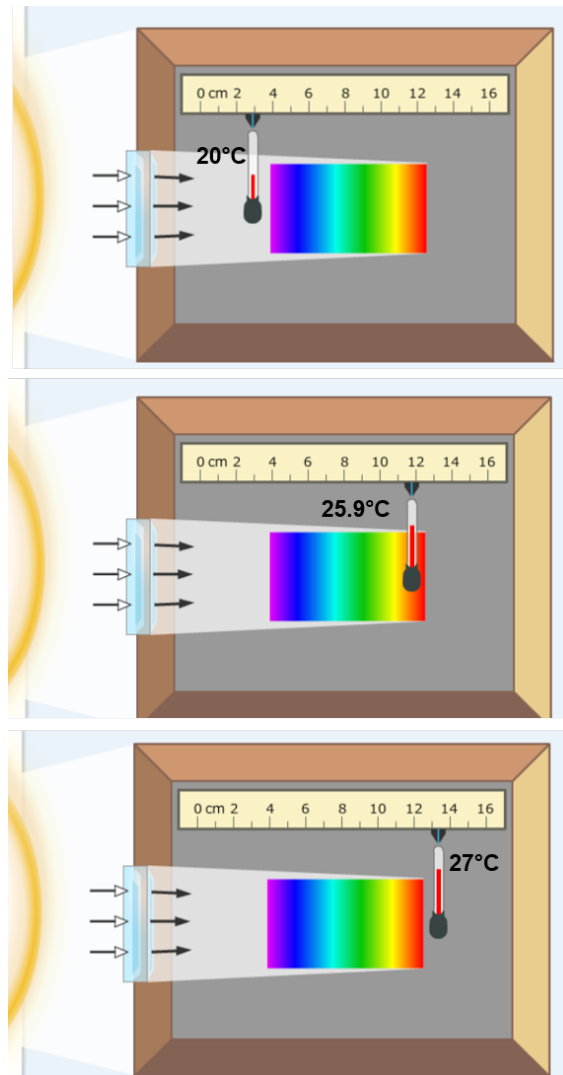


Figure 3.2: Representation of Herchel's experiment with Newton's prism. The temperature outside the visible spectrum is generally 20°C (top). The temperature increases to 25.9°C in the red region (center). The temperature increases further outside the visible spectrum to 27°C (bottom). This is explained by invisible infrared radiation (Images obtained from [42]).

maximum of EM radiation radiant energy than any other body at the same temperature. Thus, it is a perfect reference object to define EM radiation corresponding to a temperature.

All other real surfaces emit a lower quantity of energy, To quantify the amount of radiation emitted by any object at a given temperature, the concept of emissivity is used.

Emissivity

Emissivity of an object is defined as the ratio between thermal radiation emitted by the object, and the thermal radiation emitted by a blackbody at the same temperature [50, 61]:

$$\varepsilon = L_{obj}/L_{bb} \quad (3.1)$$

L_{obj} is the radiance of the surface of an object of interest. L_{bb} is the radiance of a blackbody at the same temperature.

Thus, the emissivity of a blackbody, a perfect emitter, is 1. All other objects have emissivity less than one: $\varepsilon < 1$.

Planck's Law

Planck's law can accurately describe the electromagnetic radiation of a black-body in thermal equilibrium and at a given temperature T . Thermal equilibrium is reached when there is no net flow of matter or energy between the body and its environment [61].

$$L_b(\lambda, T) = \frac{2\pi hc^2}{\lambda^5 [\exp(\frac{hc}{\lambda kT}) - 1]} \quad (3.2)$$

where $L_b(\lambda, T)$ is the radiation as a function of the wavelength λ and Temperature T .

Wien's Law

The Wien's Law states that the peak of radiation of a blackbody object varies with the temperature of the object in an inversely proportional way. To determine the wavelength for which the maximum radiation is obtained, Wien's Law provides the following equation:

$$\lambda_{max} = \frac{k}{T} \quad (3.3)$$

where λ_{max} is the wavelength on which there is a peak in the radiation. k is the Wien's displacement constant ($k \sim 2898mK$), and T is the absolute temperature of the object in Kelvins.

Fig 3.3 shows the emitted radiation as a function of wavelength for a blackbody as described by Planck's Law. Wien's Law describes that the wavelength for the maximum radiation changes inversely proportional to the temperature.

3.2 Thermography

3.2.1 History of infrared remote detectors

Remote thermocouples were the first thermal detector used in 1821. Thanks to this technology, it was possible to detect the thermal radiation of a person at a distance of 3 metres.

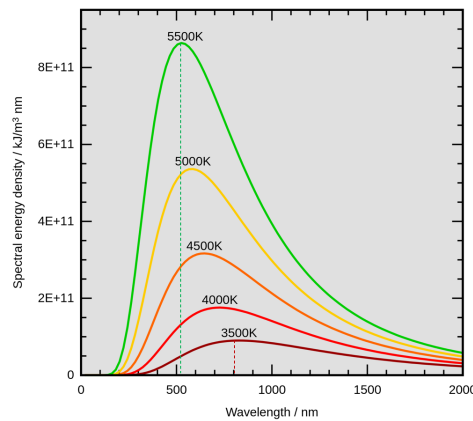


Figure 3.3: Illustration of the radiation density emitted by a black body at different temperatures. The wavelength of the radiation peak increases as the temperature decreases, i.e. wavelength is inversely proportional to the temperature. Image obtained from [4C](#), [Wiens law](#), modified by Evelyn Gutierrez, CC BY-SA 3.0

In 1880, the bolometer was invented and this was a major breakthrough. This new technology made it possible the detection of radiation at larger distances: for example, the detection of a cow was possible at 400 metres. Up to now, modern thermal imaging is based on this discovery.

Between 1900 and 1920, infrared cameras became popular for military applications; and more sensitive thermal cameras were developed at this time.

Two major advances in infrared detection technology occurred in 1939: First, the use of active thermography, in which an active light source is used to estimate the temperature of the target object. Secondly, the introduction of microbolometers for passive thermography was developed. Microbolometers allow for small and lightweight devices.

In 1950, the military secrecy surrounding the development of IR detection was released for the general public. This release enabled an increase in industrial and domestic uses. In addition, in recent years, small, low-cost thermal cameras have been introduced in recent years, which has led to their widespread use in domestic applications.

3.2.2 Thermal Imaging devices

Thermal imaging devices, also known as thermal imagers or thermal cameras are devices composed of sensors that can detect IR radiation of a scene. The IR radiation once detected is transformed into estimated temperature values using camera-specific parameters. The camera specific parameters are provided by the manufacturer and some of them can be adjusted during or after image acquisition.

From Radiation to Signal

Thermal imaging devices are composed of microbolometers which convert the infrared energy emitted to electrical signals. The electrical signals are converted to values which are proportional to the thermal radiation of the scene.

The array detector of a thermal camera device is composed of pixel detectors. Each one of them, receives the radiation and converts this to a digital signal.

$$s_i = f(M_i) \quad (3.4)$$

where s_i is the output signal and M_i the radiation intensity at pixel i .

From Signal to Temperature Estimation

The digital signal s corresponds to the total intensity of IR radiation reaching the detector. However, total radiation signal can be decomposed into the radiation of the target object and the radiation from environment factors. Thus, a decomposition has to be performed to the signal s to filter out environmental factors and obtain a signal related to the object radiation only s_{obj}

$$s = s_{obj} \cdot \varepsilon \cdot \tau_1 \cdot \tau_w \cdot \tau_2 + L_{atm1} + L_{atm2} + L_{win} + L_{refl1} + L_{refl2} \quad (3.5)$$

where:

- L_{atm1} is the signal corresponding to the radiation from atmosphere 1.
- L_{atm2} is the signal corresponding to the radiation from atmosphere 2.
- L_{win} is the signal corresponding to the radiation from the window.
- L_{refl1} is the signal corresponding to the radiation reflected from ambient 1.
- L_{refl2} is the signal corresponding to the radiation reflected from ambient 2.

Figure 3.4 depicts the decomposition of the radiation arriving to the thermal camera detector.

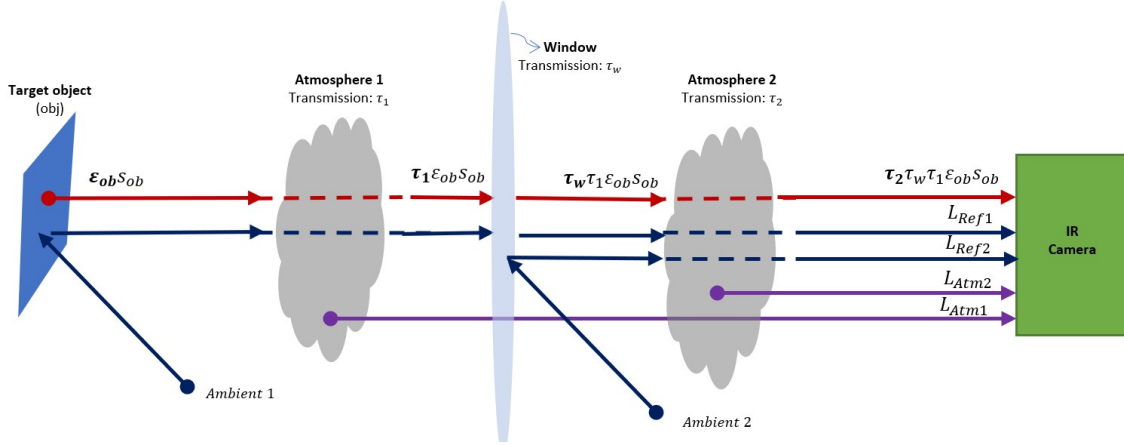


Figure 3.4: Illustration of the radiation sources reaching the thermal camera, composed of radiation from the object (red), radiation from the surroundings reflected on the object and the camera lens (blue), and radiation from the atmospheres (purple). Original image obtained from [61]. Colors were added to differentiate radiation sources.

From equation (3.5), the signal corresponding to the target object radiation, s_{obj} , is obtained as follows:

$$s_{obj} = \left(\frac{s}{\varepsilon \cdot \tau_1 \cdot \tau_w \cdot \tau_2} - L_{atm1} - L_{atm2} - L_{win} - L_{refl1} - L_{refl2} \right) \quad (3.6)$$

Given the signal associated with the object radiation, s_{obj} , the temperature is estimated from the following formula, derived from Planck's law:

$$T = \frac{PB}{\log\left(\frac{PR_1}{PR_2(s_{obj} + PF)} + PF\right)} - 273.15, ^\circ C \quad (3.7)$$

where:

- T is the temperature estimated in Celcius degrees.
- $PR1$: Planck-R1 calibration constant.

- PB : Planck-B calibration constant.
- PF : Planck-F calibration constant.
- PO : Planck-O calibration constant.
- PR_2 : Planck-R2 calibration constant.

The calibration constants are specific to each thermal imaging camera device. To obtain these parameters, the cameras undergo device calibration during manufacture [61].

Thermal Images

A thermal image, also known as infrared (IR) image or thermogram, is a digital representation of the estimated temperature in a scene. The thermal image is a single-channel image in which an arbitrary colour map has been assigned to the estimated temperature values.

Radiometric JPG files

Thermal images can be stored as radiometric JPG files. A radiometric JPG file provides, in addition to an grayscale image, an embedded matrix of values relative to the radiation of the scene.

Fig 3.5 illustrates the process of going from a radiometric JPG files to temperature values with Equation (3.7).

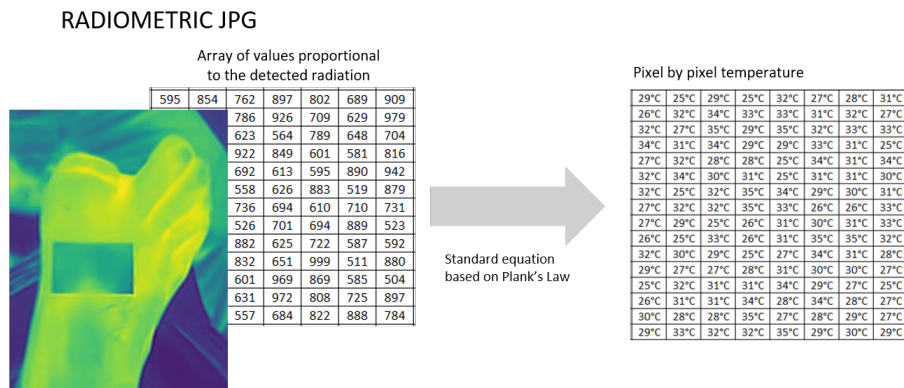


Figure 3.5: Illustration of a radiometric JPG image, and conversion to temperatures using the Equation 4.5

3.2.3 Skin thermography

Human skin has high emissivity, which is close to that of a black body, with a typical value of around 0.98 which means it emits almost all the thermal radiation that a black body would emit at the same temperature. However, the emissivity of skin can vary due to several factors, including the moisture content, which can lead to a decrease in the emissivity.

The accuracy of skin thermography can be affected by the angle of observation. Theoretical and experimental studies on human skin suggest that the emissivity significantly decreases when the viewing angle exceeds 60° [10, 56]. To minimize the effect of the viewing angle on thermography measurements, it is crucial to maintain a constant distance between the skin and the infrared camera and ensure that the viewing angle is as close to normal as possible. Specialized software or image processing techniques can also be used to account for the angle of observation and correct any errors in temperature measurement.

To measure body temperature, the peak wavelength is achieved around $\lambda = 9.5\mu m$, which corresponds to the wavelength with maximum radiant power for temperatures between 20°C and 40°C,

which are the typical temperatures of the skin and body parts. Table 3.1 shows the estimated wavelength of the peak radiance based on Wien's Law.

Therefore, thermal detectors sensible to the LWIR spectrum, from $8\mu m$ to $14\mu m$, are suitable for skin temperature measurement. LWIR thermal cameras are the most sensitive devices to the IR radiation emitted on this range of temperatures.

Table 3.1: Wavelength of the radiation peak, according to Wien's Law, for a black body at $20^{\circ}C$, $30^{\circ}C$ and $40^{\circ}C$. These temperatures are considered since this temperature range is found in the skin of the human body.

Temperature (K)	Temperature ($^{\circ}C$)	λ_{peak}
293.15	20	9.67
303.15	30	9.57
313.15	40	9.27

3.2.4 Portable and low-cost thermal cameras

Most domestic objects emit IR radiation with wavelength between $3\mu m$ to $14\mu m$, i.e. objects emit thermal radiation in the range of medium or long wave infrared, MWIR and LWIR. Hence, commercial thermal imaging devices are sensitive to either one of these two ranges of the spectrum: MWIR or LWIR.

After the introduction of thermography for both industrial and commercial use, its use has increased enormously. In addition, portable devices have been introduced and the prices of thermal cameras for non-professional use are affordable.

The latest thermal cameras from Teledyne FLIR LIC, a leading U.S. thermal camera company, are low-cost, portable, and can be used attached to a smartphone, allowing for simplified usability. Fig 3.6 shows the use of the FlirOne thermal Camera, the low-cost, portable device by FlirOne pro Teledyne FLIR LIC.

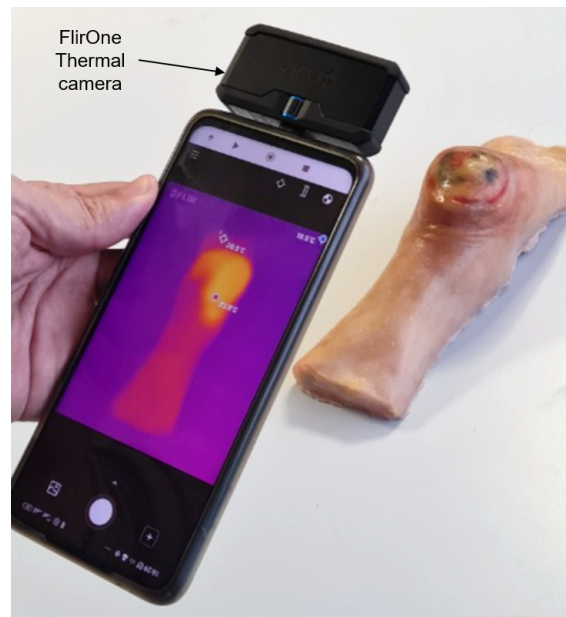


Figure 3.6: Illustration of the FlirOne Pro thermal camera attached to an smartphone for obtaining thermal images of a wound phantom.

Table 3.2: Comparison of size and price for various thermal camera devices

Name	Size	Weighth	Price
FLIR T1020	167.2 mm × 204.5 mm × 188.3 mm	2.1kg	\$25K
FLIR E96	279.4 mm x 116.84 mm x 111.76 mm	0.99kg	\$13.5K
FLIR E8-XT	244 mm x 95 mm x 140 mm	0.575kg	\$3.5K
FlirOne Pro	34 mm × 64 mm × 14 mm	34.5g	\$500
FlirOne Gen3	34 mm x 67 mm x 14mm	34.5g	\$230

Table 3.3: Comparison of size and price for various thermal camera devices

Specifications	FlirOne Gen3	FlirOne Pro
Thermal sensor size	12 um	17 um
Spectral range	8 to 14 um	8 to 14 um
IR sensor dimension	80x60 pixels	160x120 pixels
IR image dimension	640x480 pixels	640x480 pixels
Visible image dimension	1440x1080 pixels	1440x1080 pixels
FOV	50° ± 1° / 38° ± 1°	55 ° ± 1 ° / 43 ° ± 1 °
Measurement range	-20°C to 120°C	-20°C to 120°C
Accuracy	±3 °C or ±5%	±3 °C or ±5%
Thermal Sensitivity	150mK	150mK

There is a wide range of prices and various sizes available. The lightest and portable devices are the FlirOne Pro and FlirOne Gen 3, which weigh less than 50gr and are priced under \$1,000. Table 3.2 shows different thermal cameras from [Teledyne Flir LLC](#), their size and prices for comparison.

FlirOne Pro and FlirOne Gen3, the lightest low-cost thermal cameras from Teledyne Technologies Inc have similar technical specifications. The main difference is the field of view and the thermal resolution. Table 3.3 shows a comparison of technical specifications between the FlirOne Pro and FlirOne Gen3.

Both the FlirOne Pro and FlirOne Gen 3 are capable of sensing LWIR waves, making them suitable for measuring skin temperatures. Figure 3.7 illustrates the visible spectrum detected by conventional digital cameras and the LWIR spectrum detected by the FlirOne Pro and Gen 3 thermal cameras.

While both cameras provide thermal images of the same resolution, their thermal sensor resolutions differ. This disparity is due to interpolation rescaling of the original thermal image made by the proprietary software. The FlirOne Pro, for instance, increases the resolution from 120x160 to 640x480 pixels.

Overall, the FlirOne Pro is a better choice as it offers higher thermal sensor resolution than other sub-\$1,000 thermal imaging cameras

3.3 Accuracy of thermal imaging systems

Thermal imagers provide temperature estimation with certain precision; and low cost thermal cameras have lower precision. Sources of systematic errors are classified into 3 types [61], errors of method, calibration errors and errors related to electronic components.

According to simulations in [61], method errors are the primary source of error, with emissivity being a significant contributor to temperature errors. The camera-object angle and distance can also influence the accuracy of the temperature measurement. For example, the angle between the camera and the object can alter the emissivity and cause an error in thermal measurement, with larger angles resulting in lower emissivity. The distance between the camera and the object can

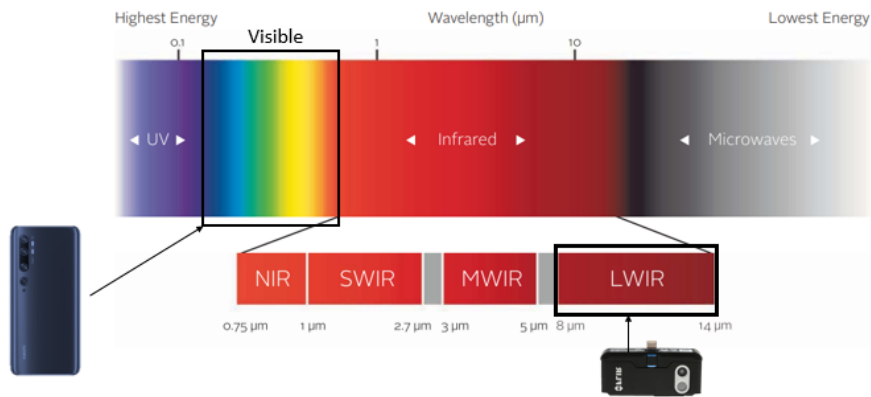


Figure 3.7: Illustration of the visible spectrum detected by a common smartphone camera, and the IR range spectrum detected with a FlirOne handheld camera [8].

also allow for more or less interference from environmental factors, affecting the accuracy of the temperature measurement [21].

Figure 3.8 depicts a summary of the sources of errors in thermography for any camera as described by [61]. It is almost impossible to completely eliminate the influence of emissivity errors. However, efforts should be made to reduce most of the errors, as this will improve the accuracy of the measurements. In this thesis, camera-object angles and distances will be taken into account for improving thermal estimation as they could be obtained when 3D information is available.

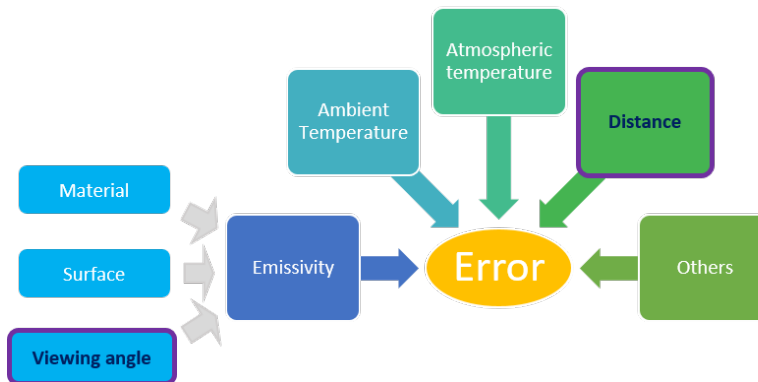


Figure 3.8: Schema of error source of any thermal camera as described by [61]. Camera-object angles and distances are highlighted as in this thesis, they are taken into account for improving temperature estimations.

3.4 Conclusion

Thermal cameras provide a graphical and quantitative tool for analyzing the temperatures of a scene by detecting infrared radiation emitted by an object. Temperature estimation consists in transforming the detected radiation into temperature from Planck-based formula that depends on various parameters of the camera, parameters related to the object and the environment.

LWIR cameras are ideal for detecting skin temperature, but many are expensive. In this context, several cameras have been compared, and the FlirOne Pro has been identified as an affordable option, plugged into a smartphone, to obtain thermographic information of wounds in clinical settings.

However, temperature estimation is subject to several errors, including those associated with distance and angles between the camera and the object, which are critical in freehand acquisition. Structure-from-Motion (SfM) can help account for these sources of error and improve the accuracy of temperature measurements.

Overall, thermal cameras provide a useful tool for analyzing temperature, but attention must be given to the parameters involved in the estimation process to ensure the accuracy of the results.

Chapter 4

Towards improved temperature estimation according to point of view

Contents

4.1 Experimental setup	35
4.2 Stage I: Exploration	38
4.3 Stage II: Improving temperature estimation	39
4.4 Conclusion	43

The previous chapter stated that temperature estimation through thermography is prone to errors due to the angle and distance between the camera and the measured object. This chapter addresses this problem and provides methods for improving temperature estimation accuracy by considering the angle and camera-object distance.

For this study, an experimental setup is performed to evaluate the effect of these factors, angle and distance, on different temperature levels controlled by a special temperature controller. Furthermore, two methods to enhance temperature estimation are proposed and analyzed. The first approach is based on single-view modeling, and the second uses a multi-view weighted averaging technique. The results of both methods are compared and discussed to determine the most useful approach for improving temperature estimation accuracy.

This chapter is organized as follows:

- The experimental framework is described in detail in Section 4.1.
- Section 4.2 analyzes the raw temperature estimation from thermography.
- The two proposed methods for improving temperature estimation are presented and discussed in Section 4.3.
- Finally, a conclusion is given in Section 4.4 section.

4.1 Experimental setup

When measuring temperatures using 2D thermography, the angle and distance between the camera and the object are not taken into consideration. This is because the 2D thermography lacks

the capability to provide information about angles and distances. Additionally, the camera's proprietary software only allows for adjusting these parameters for the entire scene, rather than adjusting them for each pixel in the thermal image.

From an experiment in which we monitor the temperature of an object, we explore the estimation error of freehand thermography. The relationship with angles and camera-object distances is analyzed to propose further improvements in temperature estimation.

4.1.1 Acquisition protocol

A temperature controller with LCD touchscreen from LINKAM (Link am Scientific Instruments Ltd, Water field, Epsom, United Kingdom) is used to control the temperature. The temperature **stage** has a circular piece of metal of 2 cm of diameter. The temperature can be set to any value between -196°C and 125°C ; and the circular piece of metal will reach the desired temperature with an accuracy of less than $\pm 0.1^{\circ}\text{C}$. Once the temperature is reached, the device keeps it for around one hour. The metal piece surface which is covered with carbon tape for eliminating specular reflections.

The FlirOne thermal camera is attached to a smartphone to simulate the handheld acquisition that occurs during clinical use. Several images are captured varying the camera-to-object distance and angle.

Four markers are placed around the temperature *plate* to calculate the distance and angle between the camera and the object, as well as a temperature label. Fig 4.1 shows the experimental setup. Two images are obtained as the thermal camera device incorporates two sensors, one for visible image and another one for thermal image.

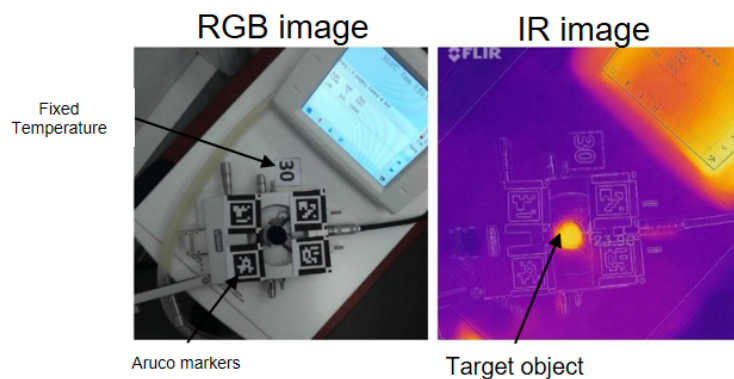


Figure 4.1: Experimental setup: A pair of images RGB-IR images obtained from FlirOne Gen3. Temperature controlled standatd is observed from different angles and distances.

The experiments are conducted within a controlled temperature closely approximating the ranges commonly found in ambient and skin temperature, a range within which indoor objects and human skin are typically observed. In order to achieve this, a set of specific temperature values, namely 21°C , 25°C , 28°C , 30°C , 32°C , 35°C , 38°C , and 40°C , have been selected for analysis.

4.1.2 Estimation of camera angle and distance fom object

The camera point of view is defined by the distance and angles between to the temperature controlled target (See Fig 4.2). The angle camera-object is defined between the optical axis of the camera and the normal to the surface of the target. The distance is defined as the euclidean distance from the camera center to the target.

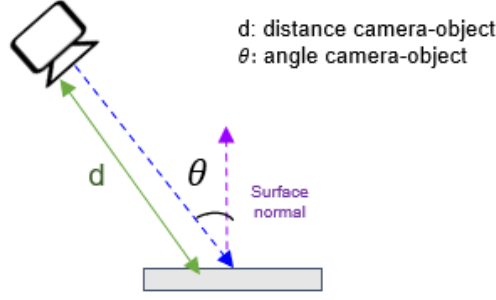


Figure 4.2: Illustration of the distance and angle of observation between the camera and the target object.

Given the camera position (\mathbf{C}), a point (\mathbf{P}) in the surface, the viewing direction vector (\mathbf{V}) and the surface normal vector (\mathbf{N}), the distance and angles are calculated as follows:

$$d = |\mathbf{C} - \mathbf{P}|$$

$$\theta = \cos^{-1} \left(\frac{\mathbf{V} \cdot \mathbf{N}}{|\mathbf{V}| |\mathbf{N}|} \right) \quad (4.1)$$

The handheld camera pose is estimated from the four aruco markers placed around the target. The estimation of the camera pose, i.e. camera-object distance and angles, is performed by utilizing four ArUco markers. The distance and angle for each ArUco marker were individually calculated, and the final camera-object distance is determined through averaging the distances of the four markers [37]. Similarly, the camera-object angle is obtained by averaging the angles of the four markers.

4.1.3 Temperature estimation from IR image

The temperature estimation from IR image is carried out using the “thermimage” package from R. It permits the adjustment of key parameters such as emissivity and ambient temperature to transform raw radiance values into temperature values (Eq. (3.7))

Ambient temperature is controlled during the experiment and set up to 22°C, while emissivity of the carbon tape covered target is set to 0.98.

The centroid of the target is manually selected in IR images, a 6x6 pixels region of interest (ROI). The average temperature is then calculated and used as the estimated temperature of the object. (See Figure 4.3)

4.1.4 Evaluation metrics

For each temperature estimate from IR image, absolute errors and relative errors are calculated from temperature controlled standard (T_{Ref}) as follows:

$$\varepsilon_{abs} = T^{Ref} - T^{Est} \quad (4.2)$$

$$\varepsilon_{rel} = \frac{(T^{Ref} - T^{Est})}{T^{Ref}} \quad (4.3)$$

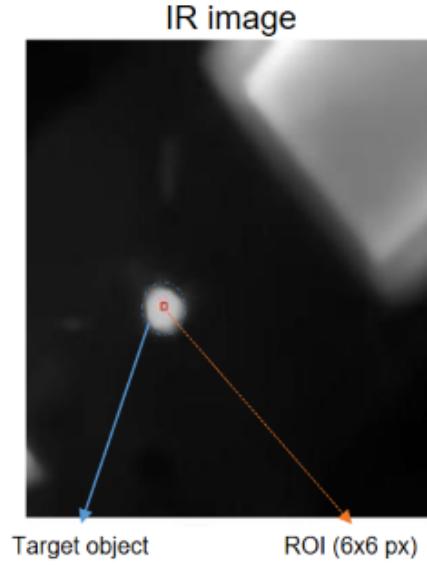


Figure 4.3: Target object and region of interest (ROI) from which the temperature has been measured

Since the errors are either positive and negative, the root mean square error (RMSE) is also considered, and it's calculated as follows:

$$RMSE = \sqrt{\frac{\sum_{i=1}^N (T_i^{Ref} - T_i^{Est})^2}{N}} \quad (4.4)$$

where N is the number of images for which the temperature is estimated.

4.2 Stage I: Exploration

Using this experimental setup, 365 thermal images are captured with FlirOne Gen3 camera connected to an iPad, varying the point of view for each temperature from 20 to 40 degrees Celsius. Table 4.1 and 4.2 present the angles and distances obtained in the experiment. The distance between the camera and the center of the target varies from 13 to 70 *cm*, and the angle varies from 0 to 60 degrees. 98% of the points of view had angles less than 50°C and distances less than 60 *cm*.

Table 4.1: Distribution of distances (in centimeters) on the 365 acquired images

Distance(<i>cm</i>)	# Obs	%
(10,15]	7	1.9%
(15,20]	86	23.6%
(20,25]	76	20.8%
(25,30]	56	15.3%
(30,35]	36	9.9%
(35,40]	30	8.2%
(40,45]	19	5.2%
(45,50]	23	6.3%
(50,55]	12	3.3%
(55,60]	13	3.6%

Distance(cm)	# Obs	%
(60,65]	5	1.4%
(65,70]	1	0.3%
(70,75]	1	0.3%
Total	365	100.0%

Table 4.2: Distribution of angles (in degrees) on the 365 acquired images

Angles (°)	# Obs	%
(0,10]	100	27%
(10,20]	126	35%
(20,30]	55	15%
(30,40]	45	12%
(40,50]	32	9%
(50,60]	7	2%
Total	365	100%

The comparison of the temperature estimates from IR images to the temperature controlled target is provided in Table 4.3. The results indicate that the absolute error ranges from -3 to 4°C and the relative error ranges from -11% to 10%. The Root Mean Squared Error (RMSE) for all images is 1.33 °C.

Table 4.3: Summary of temperature errors on the 365 acquired images

	Range	Mean	Std
Absolute error (°C)	[-2.6; 4]	-0.2	1.2
Relative error (%)	[-11.4; 10.5]	-0.9	4.1

Afterwards, the errors are analyzed according to distance and angle. Figure 4.4 presents the box plots of the relative error in percentage, grouped by deciles of distances and angles. A linear relationship between the relative error and distance is evident from the figure, while a polynomial relationship appears to fit better for the relative errors grouped by angle deciles. The pattern observed in the absolute errors is consistent with that seen in the relative errors as they are proportionally related.

The analysis of absolute and relative error indicates the potential for enhancing temperature estimates through the consideration of distances and angles. To address this, two methodologies are proposed in the next section.

4.3 Stage II: Improving temperature estimation

Two methods for improving temperature estimation in thermography are studied. First, a regression model with inverse prediction based on experimental data; and then, a multiview temperature averaging method that is evaluated using resampling techniques. The two methods are described in this section. The first methodology proposes the incorporation of distance and angle into a regression model with inverse prediction to improve temperature estimation in individual thermal images. The second approach leverages multiple views to further improve the estimation. Both methodologies are further discussed in the following section.

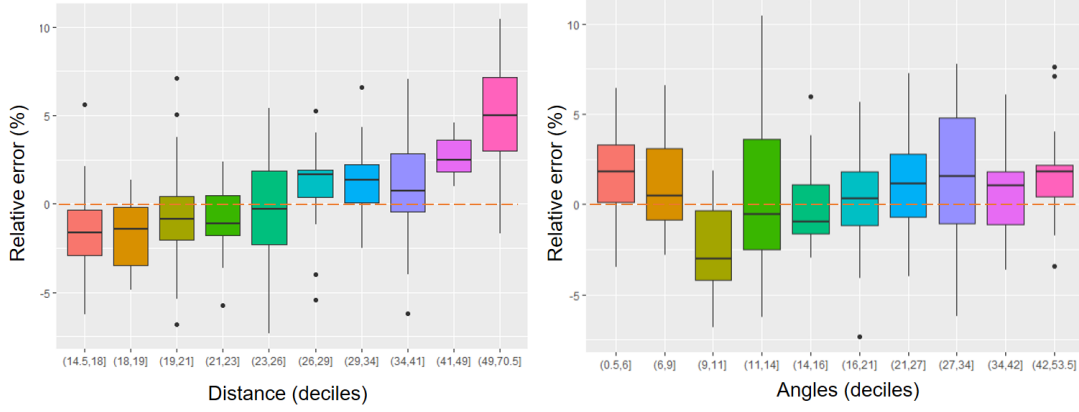


Figure 4.4: Boxplots for relative errors as a function of deciles of distances and deciles of angles of the camera from the temperature-controlled target.

4.3.1 Regression model with inverse prediction

To model the relationship between the estimated and actual temperature, a regression model that includes variables such as reference temperature, distance, angles, and their second degree term to account for their linear and nonlinear effects on the temperature estimation error. The equation of the model is as follows:

$$T_{Est} = \beta_0 + \beta_1 T_{Ref} + \beta_2 D + \beta_3 A + \beta_4 A^2 + \epsilon \quad (4.5)$$

Where:

- T_{Est} is the temperature estimated from IR images
- T_{Ref} is the real controlled-temperature of the target
- D is the distance between the camera view and the object
- A is the angle between the camera view and the object, as described previously in Section 4.1.2
- A^2 is the squared angle.

The database used for model fitting and validation is restricted to temperatures between 30°C and 40°C, resulting in a final sample size of 240 images. The regression model is fitted using 5-fold cross validation.

The objective of this study is to predict the actual temperature (T_{Ref}). However, since T_{Ref} is controlled during the experiments, it cannot be used as the target variable in a regression model due to its lack of independence between observations. As a result, the estimated temperature (T_{Est}) is used as the target variable in the regression model and T_{Ref} is included as a predictor variable.

To predict T_{Ref} , an inverse prediction methodology is applied to the regression model. The regression model and the equation for the inverse prediction procedure are illustrated in Figure 4.5.

Cross validation result is presented in Table 4.4. The results show improvements in accuracy and precision. Average error is 0.283 °C before applying the correction model, which is reduced to 0.015°C after correction. The standard deviation of errors, a measure of precision, decreased from

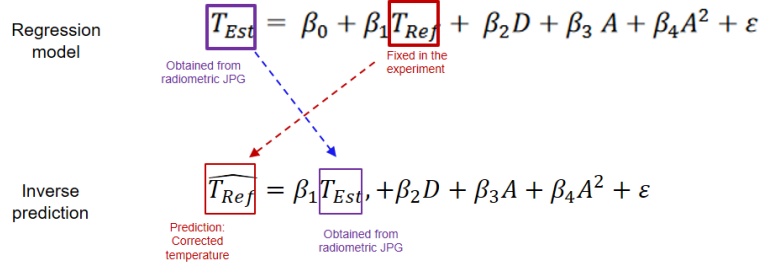


Figure 4.5: Illustration of changes in the regression model equation when using inverse prediction.

1.121 to 0.899 after correction. Additionally, the root mean squared error (RMSE) is reduced from 1.154 to 0.903, a reduction of 22.

Table 4.4: Statistics on the errors before and after applying the proposed method to improve the estimated temperatures from 5-fold cross-validation testing on 240 images.

5-Fold Cross Validation Results (n=240)		
Absolute Error (°C)	Raw estimation	After correction
Mean	0.283	0.015
Std. dev.	1.121	0.899
Relative Error (%)	Raw estimation	After correction
Mean	0.678	0.042
Std. dev.	3.190	2.60
RMSE (°C)	1.154	0.903

An R^2 of 0.932 is obtained for this model fitted to the full data set. Table 4.5 shows the estimated coefficients and p-values of significance of the variable in the proposed model. These results demonstrate the relevance of including distance and angles in the proposed model for correction (p-values < 0.05).

Table 4.5: Estimated coefficients for the temperature correlation model.

Predictors	Estimates	Confidence Interval	P-values
Intercept(β_0)	5.304	[3.998; 6.988]	<0.001
Ref. temperature(β_1)	0.880	[0.823; 0.908]	<0.001
Distance(β_2)	-0.054	[-0.059; -0.030]	<0.001
Angle(β_3)	0.039	[0.004; -0.102]	0.008
Squared Angle (β_4)	-0.001	[-0.002; -0.0001]	<0.001

The outcomes of the proposed model reveal that temperature estimation can be enhanced by taking into account the angles and distances between the object of interest and the camera. Particularly, our findings are applicable for temperatures ranging between 30 °C and 40 °C and the FlirOne Gen 3 camera. However, the extent to which our model can be generalised to other thermography devices and temperature ranges requires further investigation. In light of this, additional tests are imperative to validate our proposed model beyond the scope of this study.

4.3.2 Combining temperatures from multiple views

Weighted averaging from multiple views will be studied in this section as an alternative to improve temperature estimates. For each sample, the weighted average is calculated and used to estimate the actual temperature. The method is evaluated for four different numbers of views ($n=3, 5, 10,$ and 15) for weighted averaging and 100 samples for each reference temperature.

$$\bar{Y} = \frac{\sum_{j=1}^n w_j Y_j}{\sum_{j=1}^n w_j} \quad (4.6)$$

The weight assigned to the j -th thermal image, $w_j(\theta, d)$, is based on the angle, θ , and distance, d . The weights are defined as follows:

$$\begin{aligned} w_j &= w_j(\theta, d) = w_1(\theta)w_2(d) \\ w_1(\theta) &= \frac{1}{1 + e^{\frac{\theta-60}{4}}} \\ w_2(d) &= \frac{1}{1 + e^{\frac{d-40}{4}}} \end{aligned} \quad (4.7)$$

Shorter distances and smaller angles are assigned higher weights. This is because it has been observed that angles larger than 60° have a significant effect on emissivity [29]. On the other hand, larger distances result in larger errors due to atmospheric transmission. Based on the results in Figure 4.4, which show that relative errors increase considerably with larger distances, a cutoff value of 40 cm is chosen.

An inverse logistic function is used as a weighting function related to angle (*theta*) and camera-point distance d (See Fig 4.6). The weighting functions assign high weights to distances less than 40 cm and angles less than 60° ; and for other cases where larger distances and angles exist, small and near-zero weights are assigned.

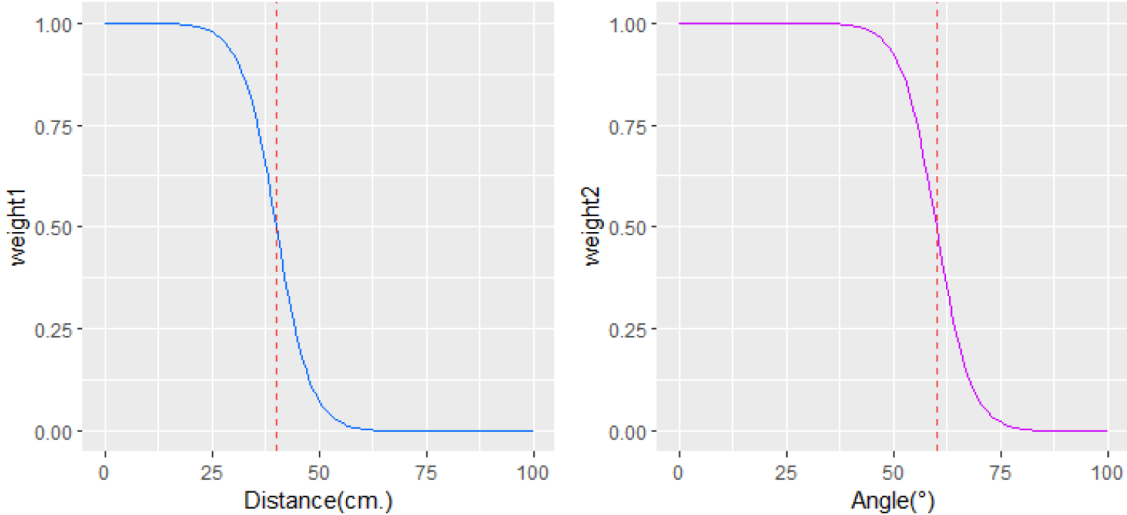


Figure 4.6: Weighting functions for distance (left) and angles (right) to calculate the multiview averaged temperature.

The results, as presented in Table 4.6, indicate that the use of a weighted average of multiple views improves the accuracy and precision of temperature estimation. The RMSE decreased from 1.33 with a single image to 0.76 with 3 images, to 0.6 with 5 images, to 0.49 with 10 images, and to 0.45 with a weighted average of 15 images. The mean error becomes closer to zero and the precision, as indicated by the standard deviation, is reduced with the use of the weighted averaging method.

Table 4.6: Absolute error and relative error using raw images, mean value and weighted mean to estimate temperatures.

	Absolute Error ($^{\circ}\text{C}$)		Relative Error (%)		RMSE
	Mean	Std	Mean	Std	
Raw IR Images (n=240)	0.28	1.12	0.68	3.19	1.154
Weigthed avg. (3 views)	-0.08	0.87	-0.05	2.55	0.760
Weigthed avg. (5 views)	-0.06	0.78	0.01	2.30	0.600
Weigthed avg. (10 views)	-0.06	0.70	0.02	2.08	0.490
Weigthed avg. (15 views)	-0.05	0.67	0.04	2.01	0.450

4.4 Conclusion

Thermal imaging cameras are susceptible to measurement errors due to various influencing factors. One weak point of low-cost thermal cameras is their accuracy, which can be inferior to professional thermal cameras, particularly when used for handheld acquisition.

Although it may not be possible to eliminate these errors completely, taking into account the angle and distance between the camera and the object has the potential to enhance temperature estimates in thermography.

Two approaches were proposed and evaluated for improving temperature estimates for low-cost portable thermal cameras. The first approach is a model-based correction, which requires temperature-controlled experiments and specialized equipment, but shows that a temperature correction model can be used for low-cost equipment. The second approach is multiview temperature averaging, which is more practical and functional. Results showed that multiview temperature averaging significantly improved accuracy and precision: the root mean square error (RMSE) can be reduced to 0.76°C when using three images and further reduced to 0.45°C when using 15 images, compared to the initial RMSE of 1.154°C obtained through raw temperature estimation from IR images.

These findings highlight the significance of incorporating additional information to enhance the precision of temperature estimates obtained through thermal imaging. We show that incorporating angles and distances into temperature estimation using multiview averaging improves temperature estimates in low-cost thermal cameras. The 3D model resulting from the structure from motion allows access to the calculations of the various points of view, making it possible to apply this multiview correction method for the temperature measurement on the object.

Chapter 5

Thermal 3D modeling

Contents

5.1 Overview of multimodal registration	45
5.2 Multimodal Stereo Calibration	47
5.3 State-of-the-art on thermal 3D model creation	49
5.4 Proposed methodology for multiview thermal 3D model	54
5.5 Proof of concept on real wounds	60
5.6 Discussion	64
5.7 Conclusion	65

As noted in Chapter 2, , 3D models provide more complete information than 2D images. In the case of thermography, the same principle applies: thermal 3D models provide more complete information than 2D thermography. In addition, 3D thermography can be useful for scanning larger curved surfaces in wound assessment and monitoring, which is not possible with 2D thermography. Current thermal 3D models rely on expensive equipment, complex configurations and usually fixed camera settings. The use of fixed camera settings presents a limitation, as it only allows scanning a limited area. Conversely, in order to scan a larger area, it is necessary to zoom out, which results in a loss of detailed thermal information. Additionally, in the case of curved areas, a single thermal view may not provide sufficient coverage of the entire area of interest. In response to these limitations, we propose a methodology that leverages 3D passive reconstruction to create multi-view thermal 3D models with simple handheld acquisition. The multi-view approach incorporates both short-distance and long-distance thermography, providing greater coverage and detail while also improving temperature estimation through the use of low-cost thermal cameras.

Furthermore, the use of portable and easy-to-acquire devices for image acquisition makes its use more accessible than previously proposed methodologies in remote areas, for example, where there is a lack of medical staff.

In this chapter, we present a methodology for creating thermal 3D models for scanning various wound surfaces and sizes, and provide robust temperature estimation. This chapter is structured as follows:

The chapter is divided into five sections: In Section 5.1, we presents an overview of multimodal registration with a focus on IR-RGB images. In Section 5.2, we explain multimodal calibration, which is usable when using rigidly connected multimodal sensor. Then, in Section 5.3, we provide an overview of the current methodologies for creating thermal 3D models. Next, in Section 5.4, we present the details of our proposed methodology. Finally, in Section 5.5, the experimental

validation of the proposed methodology is presented, followed by a discussion in Section 5.6. The conclusion ends the chapter in Section 5.7.

5.1 Overview of multimodal registration

Before diving into the topic of multimodality, let's first define registration and modality. Registration is the process of aligning in a common reference system two or more similar objects taken at various times or from diverse sensors [79]. In medical imaging, the term "modality" refers to the type of imaging technology used to acquire an image. Examples of imaging modalities include X-ray, magnetic resonance imaging (MRI), ultrasound, and thermography (IR), among others.

Unimodal registration consists of aligning images from a single modality. For example, it could consist of aligning two different infrared images of the same body part captured with the same technology at different times. In contrast, multimodal registration involves aligning images from different modalities, such as aligning a thermal and an RGB image of the same body part. Multimodal registration is more difficult than unimodal registration because of differences in the features and characteristics revealed in each image modality, making direct comparison quite complex.

To achieve the desired alignment, a reference image and a moving image are involved, and a spatial transformation should be found to bring the moving image closer to the reference one. According to [46], multimodal registration methodologies are classified in feature-based and intensity-based.

In the feature-based approach, points, lines, or contours, are used with matching techniques to align the moving image with the reference image. However, finding common unique features between the multimodal images can be a challenge due to their different nature.

On the other hand, the intensity-based approach involves finding the spatial transformation by optimizing a similarity metric between images. The similarity metric depends on a comparison of the intensities between both images. The method is straightforward, but selecting a suitable evaluation metric for accurate image alignment is a challenge.

To date, there is no general methodology for multimodal registration that works well in all environments. The method of registration depends on the specific characteristics of the image pair to be registered, and it requires making three crucial decisions in selecting - the appropriate spatial transformation, - the similarity metric, and the optimization algorithm.

5.1.1 RGB-IR registration

This section focuses on the registration between color and thermal images. Color images are acquired and stored as an RGB matrix defining the red, green and blue color components. IR images only encode one radiation value and usually have a much lower resolution than color images.

Registration of RGB to IR images poses a significant challenge due to the fundamental differences between color and IR images. While color images contain sharp color changes, IR images exhibit smooth intensity changes, making edge identification difficult (See Figure 5.1). Previous studies have attempted to solve this problem by using entropy similarity metrics, such as mutual information, in an intensity-based registration approach. This technique aims to optimize the alignment of RGB and IR images by measuring the similarities between their respective intensity values. This presupposes the transformation of the RGB image into an grayscale intensity image. Despite its usefulness in some scenarios, the intensity-based approach has certain limitations, such as the difficulty of selecting suitable evaluation metrics to ensure an accurate image alignment.

Feature-based registration with silhouettes is another common approach used for aligning infrared and color images, particularly when the objects of interest are warmer or colder than the ambient temperature, as in the case of human skin [16]. This method requires small objects with varied contours, which are far away from the camera to ensure that the edges of the object can be detected. Buildings, for example, have visible and detectable edges in both infrared and RGB space, which

can be used for thermal color registration [104, 43]. Another application is the IR-RGB registration of head images using the edges of facial features and contours of the head. The edges and textures of wounds can also be used for registration, as demonstrated in the registration of foot images for diabetic foot ulcer prevention [38]. In this case, images of the feet are taken from a distance of about 80 cm, allowing the contours of the foot to be well distinguished and registered.

When it comes to registering thermal and color images, there are several challenges to consider, especially when dealing with thermal images of skin and body parts.

Lack of texture in thermography When dealing with thermography of skin with no lesions, the temperature may not exhibit significant variability, and uniform values are not helpful for registration. To enhance the contrast of IR images in such cases, an intensity transformation is applied [52].

Lack of distinctive silhouettes Another related challenge is the lack of sharp silhouettes of the target object. For example, in the case of legs, silhouettes do not vary much even if there are large changes in perspective. This can lead to registration errors if silhouettes are used. Figure 5.1 illustrates this problem by showing an example of two IR images in which the silhouettes are very similar, however, they are taken from different perspectives. A registration between the silhouettes of both images could lead to an incorrect registration.

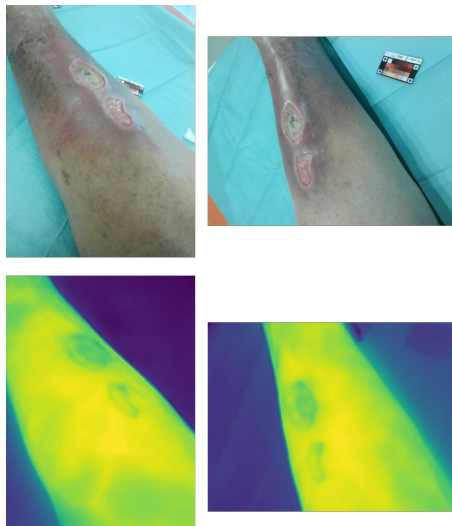


Figure 5.1: Illustration of the lack of distinctive silhouettes in IR images which can lead to mismatched registration of silhouettes.

Confounding silhouettes A limitation of the use of silhouettes arises when background objects alter the silhouettes of object of interest in IR images. This can occur in the case of wound imaging in clinical settings: by scanning the object from multiple perspectives, the patient's surrounding body may be confused with the object of interest in the IR image space.

Fig 5.2 shows an example where silhouettes of the object of interest are not easily distinguishable between IR and RGB images. In this example, the silhouette of the foot is not well defined in the IR image due to the presence of the other leg.

In conclusion, the registration between IR-RGB images is mainly done by features, in particular silhouettes. When they are distinctive and appear in both modalities. This is especially useful in certain cases such as: buildings, faces or small objects having sharp edges. For wounds on feet and legs, a lack and mis-segmentation of the silhouettes can complicate the registration.

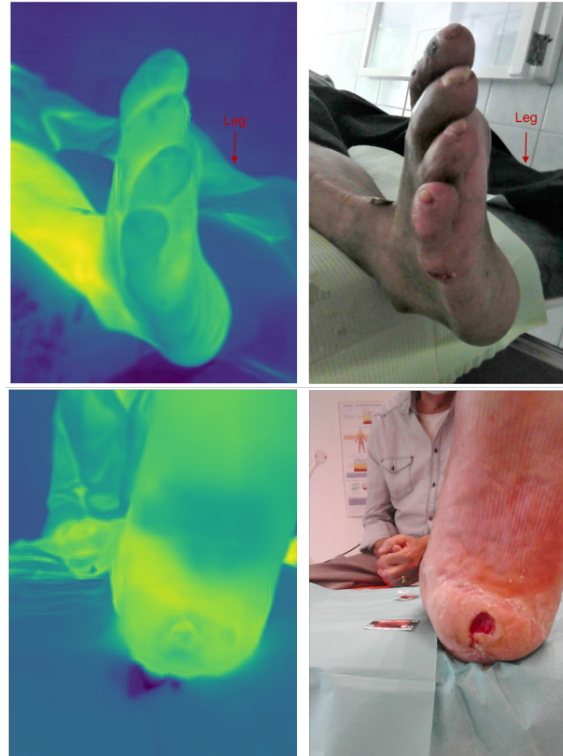


Figure 5.2: Infrared and corresponding RGB image of a foot where contours are not clearly defined in the infrared image due to the presence of other leg.

5.2 Multimodal Stereo Calibration

Multimodal calibration consists on obtaining a geometrical transformation between cameras poses when the RGB and IR camera sensors are in relative fixed positions. It also provides intrinsic features for each camera like distortions. This section details the multimodal stereo calibration used with FlirOne Pro, a portable thermal device. The calibration step will subsequently be incorporated in the proposed methodology for the creation of the thermal 3D model.

FlirOne Pro has two built-in sensors: due for IR for color images, vertically aligned and separated by a small distance (See Figure 5.3).



Figure 5.3: FlirOne Pro thermal camera. In this camera, RGB and IR sensors are in fixed relative positions.

The FlirOne Pro camera takes, from one single shot, a pair of images: an RGB image and a IR image. Moreover, since the relative positions of the two sensors are fixed, a stereo calibration is used. The process of calibrating a stereo camera involves determining the intrinsic parameters of each sensor and the geometric transformation between the extrinsic parameters

The most common way to perform a stereo calibration is from images of an object containing a pattern with edges recognizable from both cameras. When dealing with unimodal calibration, i. e. both cameras provide same modality, for example, both are visible cameras, a black and white chessboard is used.

For multimodal calibration, a special chessboard required to be created. The chessboard was made of two materials with contrasting thermal properties to allow a distinctive pattern to be detected in the IR and RGB image views.

Multimodal chessboard pattern

The multimodal chessboard is an 8x5 board measuring 26cmx16cm. The chessboard is made of a rectangular white tile and black foam squares. This chessboard is refrigerated for 15 minutes, after which the board is removed from the refrigerator, and the photo shoot is performed.

Figure 5.4 shows the detection of corner points on the chessboard in both modalities.

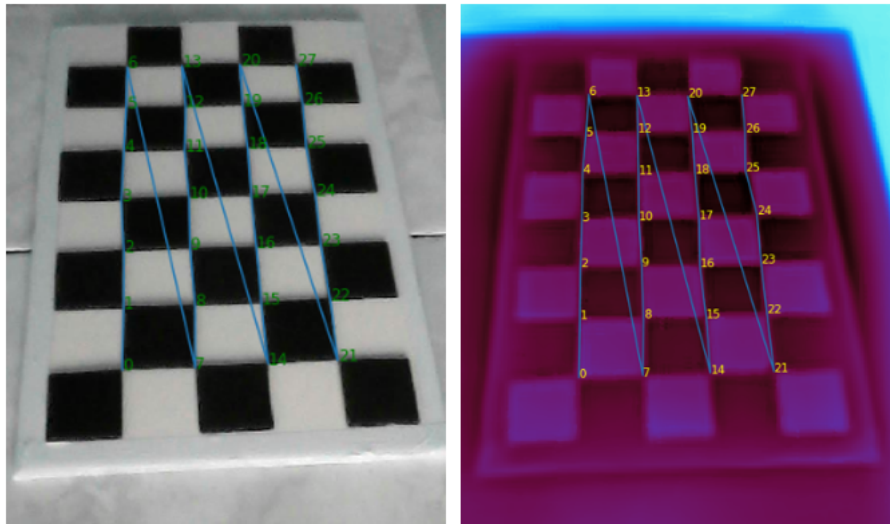


Figure 5.4: Example of the detection of edges on RGB image (left) and its corresponding IR image (right) for a multimodal calibration chessboard.

Chessboard Points Detection

Chessboard detection in RGB images is performed with standard algorithms implemented in the OpenCV Python library. On the other hand, chessboard detection in thermal images are difficult to detect as borders are not well defined. Thus, a procedure to preprocess the image is followed and described below:

1. First, contrast enhancement is applied to better differentiate black and white colors.
2. Then, conversion to grayscale is applied. This is done in preparation for applying the next step.
3. Chessboard edge detection with classical algorithms is performed using the OpenCV Python library.
4. Finally, a refinement of the detected points inspired by [92] is performed. The RANSAC algorithm is applied to the detected points to correct the misalignment between points belonging to the same row and columns.

Geometrical Transformation

The multimodal calibration consists initially on estimating the intrinsics and extrinsics for each sensor: RGB and IR sensor. Once intrinsics (K_{RGB}, K_{IR}) and extrinsics (R_{RGB}, R_{IR}, t_{RGB} and t_{IR}) are obtained, the relative geometrical transformation between the IR and RGB sensors are computed. Let R^* and t^* be the rotation and translation that define the geometrical transformation between the two sensors. Calculation of these matrices is done as follows:

$$R^2 = R^*R^1 + t^*t^2 = R^*t^1 \quad (5.1)$$

Then, R^* and t^* are the parameters that minimize the total re-projection error for all the points in all the available views from both cameras. The individual calibration as well as the stereo calibration was done using the OpenCV library in Python [18].

5.3 State-of-the-art on thermal 3D model creation

A thermal 3D model is a three-dimensional representation in which surface temperature data is stored. In this section, we review various methodologies for creating thermal 3D models, focusing on their use in skin and wound analysis.

The creation of these thermal models has been divided into two types: calibration-based methods and registration-based methods depending on the strategy used to create the thermal 3D models. Figure 5.5 depicts our classification of strategies for creating thermal 3D models.

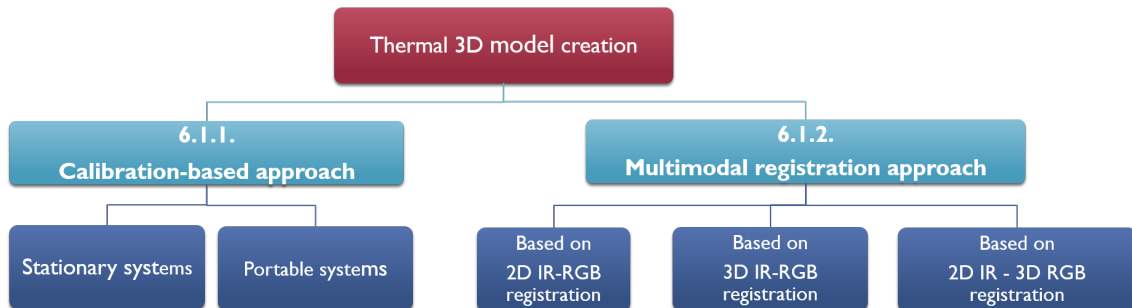


Figure 5.5: Our classification scheme for thermal 3D modeling methods.

5.3.1 Calibration-based method

Calibration-based methods rely on using a geometrical transformation to accurately estimate the pose of the thermal camera. Once the thermal camera pose is obtained, temperature values are mapped to the 3D point cloud via raycasting. Calibration-based methods are implemented on systems that are either stationary or portable. These two types of systems are reviewed below:

Stationary systems

In recent years, several studies have focused on the creation of thermal 3D models. To achieve accurate camera pose estimation, stationary systems have been employed in these studies. Stationary systems involve the use of devices that remain in fixed positions, which improves the accuracy of thermal and color camera pose estimation; however, the scanning area is restricted.

One of the earliest systems on record for thermal 3D modeling of skin employed a stationary system consisting of three devices: a pair of stereo cameras and a thermal camera [49]. The high-resolution stereoscopic cameras facilitated the creation of the 3D model from two different views, while the thermal camera provided 2D infrared images and radiance values that were mapped to the 3D model by raycasting and correction based on the viewing angle between the thermal camera and the skin surface. The use of a tripod was essential to ensure that all devices remained in fixed positions during calibration and acquisition.

Other studies have used structured light for 3D reconstruction [30, 12] and high-precision thermal cameras to obtain IR images, both fixed on a tripod to maintain fixed relative positions.

More recently, passive reconstruction has been employed to create three-dimensional thermal models [93, 13]. In [13], a portable thermal camera on a tripod was used to acquire images from different points of view; and in [93], a system consisting of a large rig with three high-definition cameras and three low-cost FlirOne thermal cameras was used. Although the cameras were portable, the large size of the equipment did not allow the entire system to be easily transported. In addition, the use of only three views limits the reconstruction to a restricted three-dimensional surface.



Figure 5.6: Stationary thermal 3D model systems. Images obtained from [101] (a), [30] (b), [12] (c), [51] (d), and [105] (e), [53] (f).

Table 5.1: Studies on the creation of thermal 3D models using stationary systems.

Study	3D modeling approach	3D modeling device	Thermal Camera (IR image Resolution)	# of Application cases
Skin and wounds				

Study	3D modeling approach	3D modeling device	Thermal Camera (IR image Resolution)	Application	# of cases
Ju, Nebel, and Siebert [49]	Stereo Reconstruction	Two high resolution cameras: Mamiya RZ67 PRO II)	FLIR Indigo Systems Merlin (320 x 256px)	Head	1
Colantonio et al. [30]	Structured light reconstruction	SONY XCD 910 SX (4MP)	FLIR A40 (320 × 240px)	Feet	3
Barone, Paoli, and Razionale [12]	Structured light reconstruction	RGB video camera (CCD, 10 MP) Standard video projector (DLP, 10MP pixels)	Thermal video camera NEC TH-9100 (320 × 240px)	Wounds	7
van Doremalen et al. [93]	Multiview Reconstruction	Vectra XT, Canfield Imaging Systems	FLIR One Gen 2 (160 × 120px)	Feet	8
Kręcichwost et al. [51]	Stereo Reconstruction + RGB-D	RGB Camera - Fujifilm X-T1, Stereo Camera - MicronTracker Hx40, Depth Camera - SwissRanger SR4000	FLIR A300 (320 × 240px)	Feet	79
Other applications					
Yang, Su, and Lin [104]	Stereo Reconstruction	Two iPhone SE	FlirOne Gen 3 (320x 240px)	Buildings and interior scene	3
Landmann et al. [53]	Structured light reconstruction	Two Photron FASTCAM SA-X2	FLIR X6900sc SLS (640x512px)	Moving targets: inflating airbag, a basketball player and the crushing of metal.	3

In summary, stationary systems can help provide accurate thermal 3D models, however, they are highly expensive and limited on scanning surface. Stationary systems are expensive as they are composed of high end devices like laser scanners. Stationary systems can access only to a few views of the scene, thus, reconstruction is limited to a small scene. Furthermore, the lack of portability is an additional problem. For this reason, presumably, most previous studies are implemented in few cases of application on the skin and wounds.

Portable Systems

Portable systems, on the other hand, are simpler to use and provide the advantage that multiple views of the scene can be scanned. Recent studies have shown the introduction of portable systems consisting of a 3D scanner with good accuracy and cameras mounted in fixed relative positions. However, only a few of them are applied on the skin, wounds and none of them is applied in more than 3 practical cases.

In [95, 96], they introduce a systems composed of a thermal camera and a commercial multi-sensor based equipment, i.e. Xbox. The commercial device is composed of a projector, an RGB camera and a NIR camera, and serves to create the 3D model structure. Both devices, Xbox and thermal camera, are attached with a holder and connected to a computer for a real time acquisition.

In a similar way, previous propositions rely on multiple devices attached to a holder [71, 101]. In contrast with previous approach, depth sensors are employed to create the 3D structure. Thermal camera to provide temperature values to the 3D model.



Figure 5.7: Portable thermal 3D model creation systems. Device images obtained from [96] (a), [71] (b), and [81] (c).

Portable systems are advantageous over fixed systems as they provide a comprehensive multi-view evaluation of the surface, However, portable systems require hand-held support to keep relative positions fixed. In addition, depth camera devices, although less expensive than laser scanners, could require a connection to a computer or power source, which could restrict their portability. Table 5.2 summarizes previous studies performed with portable 3D thermal modeling systems.

Table 5.2: Studies on the creation of thermal 3D models using calibration-based portable systems.

Study	3D modeling approach	3D modeling device	Thermal Camera (Resolution)	# of Application cases
Skin and wounds				
Moghadam [63]	RGB-D camera based	RGB-D camera (ASUS Xtion Pro Live)	Thermoteknix Miricle 307K (640 x 480px)	3 Human body parts (torso and legs)

Study	3D modeling approach	3D modeling device	Thermal Camera (Resolution)	Application	# of cases
Xu et al. [101]	RGB-D camera based	Structured light scanner (Microsoft Kinect v2 sensor)	Flir A65 uncooled LWIR (640 × 512 px)	Human body in indoor scene	-
Other applications					
Vidas and Moghadam [95], Vidas, Moghadam, and Sridharan [96]	RGB-D camera based	RGB-D camera (ASUS Xtion Pro Live)	Thermoteknix Miricle 307K (640 x 480px)	HVAC systems and machinery	
Ordonez Muller and Kroll [71]	RGB-D camera based	RGB-D camera (PrimeSense Carmine 1.09)	Optris PI 450 (382 x 288px)	Objects within a laboratory	3 case studies
Schramm et al. [81]	RGB-D camera based	Intel RealSense D415 (RGB 2MP, D	Optris PI 450 (382 x 288px)	Indoor scenes with lab objects	2 case studies

5.3.2 Multimodal (IR-RGB) registration approach

The multimodal registration approach are those not based on camera calibration, but on image registration. There are 3 types of multimodal registration that can be used for creating thermal 3D models:

1. 2D registration, i.e. IR-RGB images-based registration
2. 3D registration, i.e. aligning the color and thermal 3D models
3. 2D-3D registration, i.e. aligning 2D thermal image information onto 3D model

Few studies have proposed techniques to create thermal 3D models for skin and wound applications, especially applying multimodal registration.

Based on 2D registration

2D registration of color and thermal images for skin or body areas is often based on silhouette registration. This is feasible when body and skin images are taken from a great distance, as several edges become visible in both modalities, making alignment between images feasible. However, in the case of close-up images of extremities such as legs, the edges are not easily distinguishable, and this may result in incorrect registrations. As per our knowledge, this has not been used before for thermal 3D model creation. Presumably because Small registration errors in 2D images, can lead to large registration errors in 3D.

In devices with stereoscopically placed sensors, 2D multimodal registration can be performed using a fixed scaling and 2D translation, if the object scanned is kept at a fixed distance from the camera. [13] applies this idea to the fusion of thermal and color images taken from a specifically fixed distance. Then, using fused RGB and IR images, the thermal 3D models are created.

Based on 3D registration

This methodology involves aligning a noisy thermal 3D point cloud to a color 3D model. To achieve this, a thermal 3D model needs to be created using a passive 3D reconstruction method. In a study by Truong et al. [92], a portable system with a straightforward process was presented. The system applies SfM reconstruction to 2D RGB and 2D IR images, creating a color 3D model and a thermal 3D model, respectively. The resulting point clouds are then registered using ICP-based algorithms to align the thermal data with the color 3D model. The system requires only a portable color camera and an IR camera, and offers advantages such as simplicity, portability, and wide coverage of the reconstruction. The methodology is successfully applied to indoor scenes and buildings which contain varying intensity values and distinguishable edges in both IR and RGB modalities.

Based on 2D to 3D registration

This method consists of finding the thermal camera pose by optimizing a similarity metric between thermal data from 2D images and a 3D model. In [52], a 3D model is created using Structure from Motion (SfM) on RGB data, while [22] employs a laser scanner. Both models are projected onto a 2D space where an optimization is performed to find a thermal camera pose that optimizes the silhouette similarity metric. These methods have been successfully applied to individuals heads [52], small designed objects, and distant images of large statues where silhouettes are obvious [22].

In summary, two approaches are distinguished for creating thermal 3D models. First, an accurate estimation of the infrared thermal camera poses is performed. Then, raycasting is performed to assign the temperature values to the 3D model. To achieve high accuracy in camera pose estimation, active or stationary reconstruction systems are needed. To provide these systems with portability, manual assistance is often needed to maintain fixed relative positions. A second approach is based on multimodal registration. The thermal camera pose is estimated by optimizing a similarity metric, which is created from detectable silhouettes. This approach requires multiple edges to be detectable in both thermal and color imaging modalities. However, not many applications have been demonstrated in skin.

5.4 Proposed methodology for multiview thermal 3D model

This section presents a methodology for creating multi-view thermal 3D models.

The proposed methodology is implemented using images from two low-cost devices: a mobile device, which can be a smartphone or a tablet; and a dual sensor thermal camera, FlirOne Pro.

Several RGB and IR images are collected in manual mode from both devices, which serve as input for the proposed methodology (See 5.8). This methodology combines multimodal calibration and methodologies used in 2D/3D registration based approaches. The methodology is divided into 3 stages:

1. Calibration-based thermal 3D model creation.
2. Refinement of thermal camera poses.
3. Fusion of several thermal views.

In the first stage, 3D model is created with passive reconstruction from multi-view RGB images, and thermal camera poses are estimated using multimodal stereo camera calibration. Then, refinement of the thermal camera poses is performed based on an optimization technique. Finally, in the third stage, multi-view thermography is combined to estimate temperatures onto the 3D model. Fig 5.9 shows the complete pipeline of our proposed methodology.

Each of these stages is described in detail below.

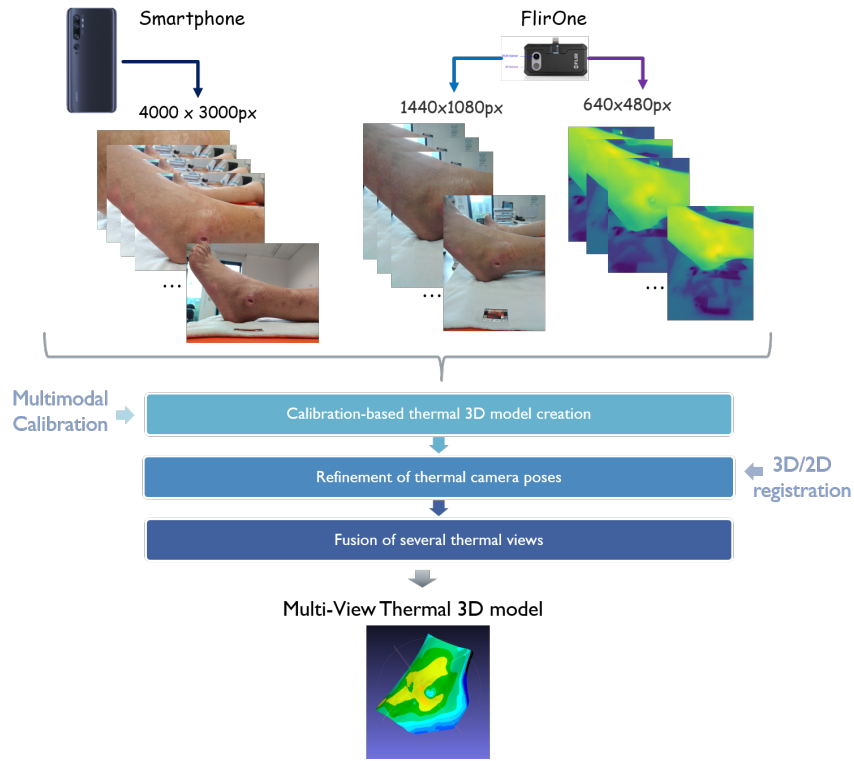


Figure 5.8: Summary of the inputs, outputs and stages of the proposed methodology.

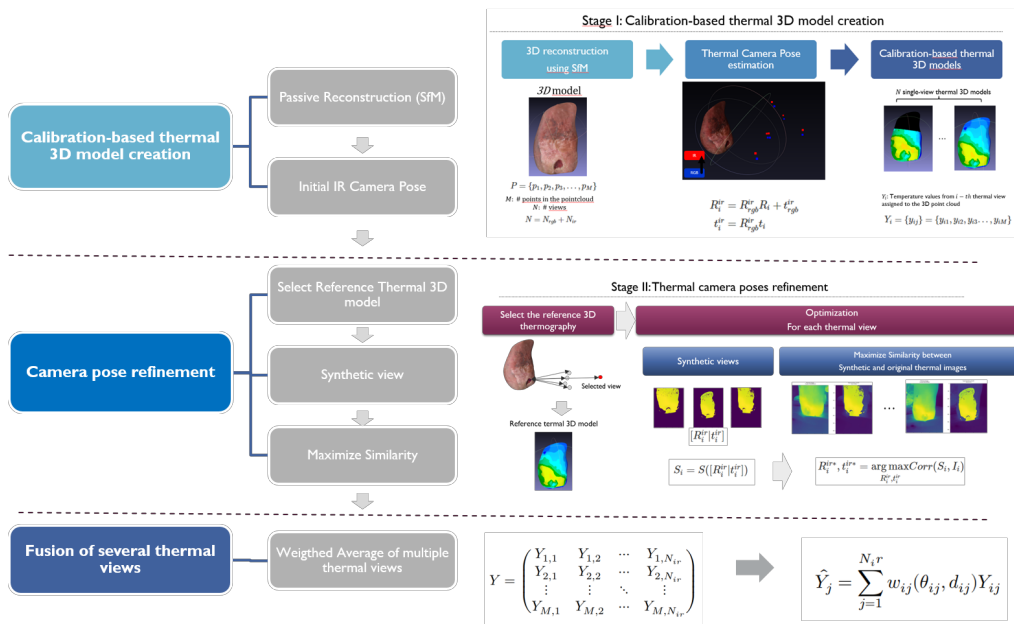


Figure 5.9: Workflow of the proposed methodology.

5.4.1 Stage I: Calibration-based thermal 3D model creation

The creation of single thermal 3D models is done by estimating the thermal camera pose of the FlirOne camera using multimodal calibration. Then, using raycasting, temperature estimated from radiometric files is transferred from 2D to 3D point cloud. Figure 5.10 illustrates this stage.

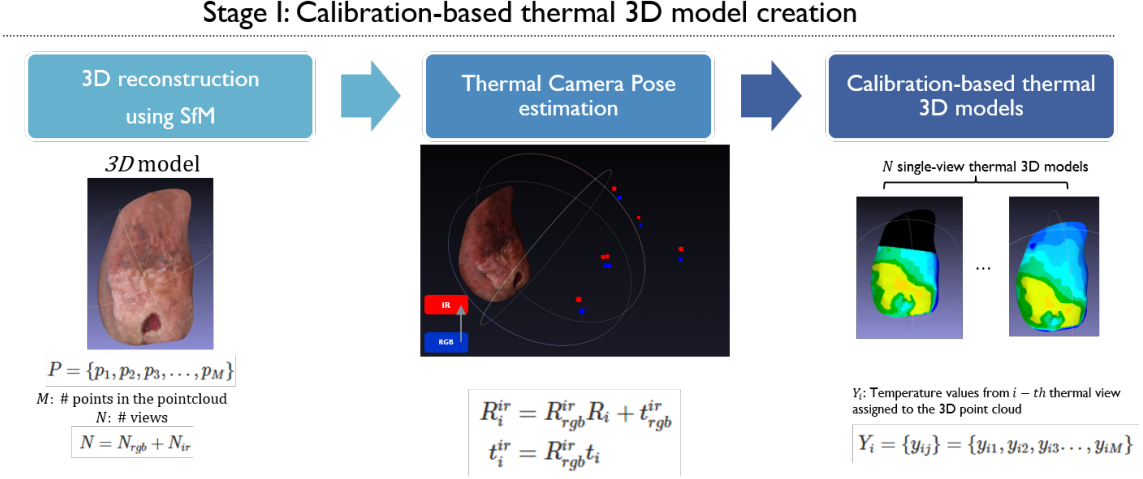


Figure 5.10: Workflow illustrating the creation of calibration-based thermal 3D models using passive reconstruction and multimodal calibration of stereo cameras.

The steps of this stage are explained in more detail below:

3D Structure from Motion (SfM)

The process of 3D reconstruction requires the use of RGB images as input. These RGB images can come from two sources: those taken using a smartphone or other mobile device and those captured using an IR device. Chapter 3 presented a portable thermal Camera: FlirOne Pro, which is capable of capturing both an RGB image and a IR image simultaneously. For the purpose of estimating camera poses from FlirOne Camera, the RGB images captured by the FlirOne Camera are used as inputs.

The 3D model is reconstructed using multi-view RGB images taken with a digital camera. The Structure from Motion algorithm, as implemented in the open-source software Meshroom [7], is used to perform the reconstruction. The feature detectors utilized are SIFT and AKAZE, with a sensitivity setting of “high” for smartphone images and “ultra” for low-resolution FLirOne RGB images. A maximum reprojection error of 4 is setup to the SfM algorithm.

As a result of the passive reconstruction, a 3D mesh, i.e., a point cloud P , and triangular polygons are obtained; along with estimated camera poses for all RGB cameras: i.e., smartphone camera poses and FlirOne camera poses. The number of images used for the reconstruction is N and could be written as follows:

$$N = N_{rgb} + N_{ir} \quad (5.2)$$

Where N_{rgb} is the number of color images captured by the mobile device that are used for 3D reconstruction. N_{ir} is the analog for the FlirOne thermal camera device.

Thermal camera pose estimation

After the SfM reconstruction, a 3D model represented by pointcloud $P = \{p_1, p_2, p_3, \dots, p_M\}$, composed of M points is obtained, as well as the camera pose is estimated $[R_i | t_i]$ for each color

image i . $i = \{1, 2, 3 \dots N\}$

The IR camera pose is determined using the multimodal calibration previously described in (5.1). Then, the IR camera poses are estimated based on corresponding stereo RGB camera poses as follows:

$$\begin{aligned} R_i^{ir} &= R_{rgb}^{ir} R_i + t_{rgb}^{ir} \\ t_i^{ir} &= R_{rgb}^{ir} t_i \end{aligned} \quad (5.3)$$

where $[R_i^{ir}|t_i^{ir}]$ represents the rotation and translation matrices of the i -th camera pose. This is computed for each of the N_{ir} images captured from FlirOne, $i = 1, 2, 3 \dots N_{ir}$.

Temperature information onto 3D models

For each thermal view, using the estimated IR camera pose, a calibration-based thermal 3D model is created. To assign temperatures to the 3D model, we do the following: First, the 3D model is transformed into the image plane through projection transformations. Then, points are assigned temperatures depending on the temperature of the pixels where they fall. Thus, for each j of the N_{ir} flirOne images, using the initial estimated camera pose, the thermal values associated with the j -th views are as follows:

$$Y_j = \{y_{ij}\} = \{y_{1j}, y_{2j}, y_{3j} \dots, y_{Mj}\} \quad (5.4)$$

where y_{ij} is the temperature value using view j assigned to the i -th point of the 3D point cloud. $i = \{1, 2, 3, \dots M\}$, and $j = \{1, 2, 3, \dots N_{ir}\}$

5.4.2 Stage II. Refinement of thermal camera poses

The thermal camera poses estimated in Equation (5.3) are subject to two sources of error: 1) errors related to the RGB camera pose estimated via passive reconstruction, and 2) errors related to the geometrical transformation determined by the stereo calibration. To address these errors, a refinement of the camera pose is incorporated. This refinement involves selecting one of the thermal views and using its corresponding calibration-based thermal 3D model to improve camera poses of the rest of the thermal 2D views.

As a result of the 2D/3D registration, the thermal camera poses are refined. Figure 5.11 depicts the workflow for this stage where camera pose refinement is performed.

The registration of a thermal 3D model and 2D IR images is achieved by solving an optimization problem in 2D space. We generate synthetic views by projecting the reference thermal 3D model and use the optimization algorithm to maximize the similarity between the synthetic thermal views and the real thermal images. We use the correlation between pixel values as a similarity metric, as both images contain thermal data from the skin and wound scene. As a result of the optimization process, we can refine the IR camera poses.

The refinement process implemented is similar to the optimization-based registration approach presented in [101] where multimodal registration was done on thermal images and depth images.

Selecting the reference thermal 3D model

When using thermal camera poses to transfer temperatures from 2D thermography to the 3D model, even small errors in camera pose estimation can cause significant registration errors, particularly when images are taken from a short distance. To mitigate this problem, we propose using

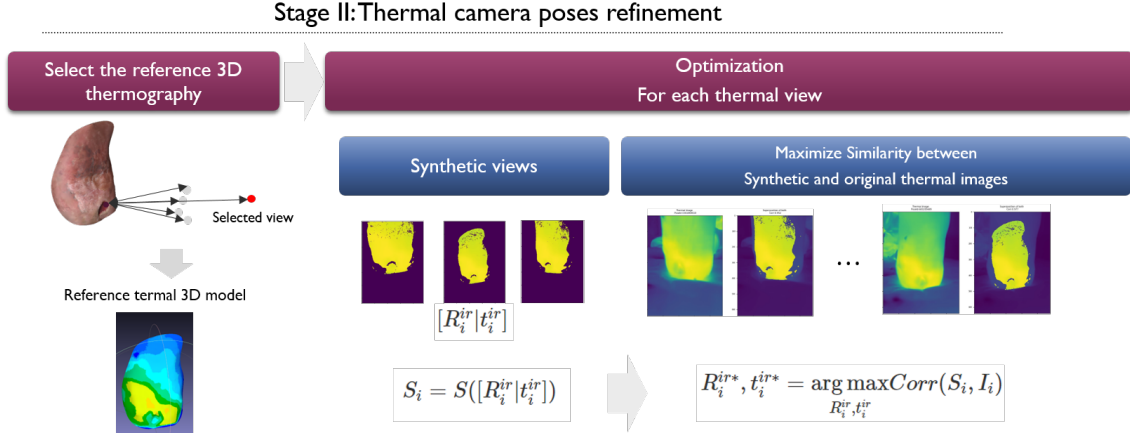


Figure 5.11: Illustration of the thermal camera pose refinement process based on the reference thermal 3D model and optimization.

the farthest thermal view as the reference view and adjusting the camera poses in other views to match the thermal patterns in the reference view.

By using this reference Thermal 3D model approach, we can refine the camera poses in other views to achieve high correlation with the reference thermal 3D model. This method offers two key benefits: first, the farthest thermal view provides a reference thermal 3D model for multiple views, which helps to cover a large portion of the surface; second, errors in camera pose estimation have minimal impact on creating the thermal 3D model.

To determine the farthest image, we measure the distances between the wound 3D model and the camera poses. We then use the selected thermal view to assign temperatures to the 3D model, resulting in a thermal 3D model called the Reference Thermal 3D Model (RT3DM).

Synthetic views

A synthetic view is created using rasterization, which involves projecting the 3D model pointcloud (P) onto a 2D plane of the IR camera. This projection is similar to taking a virtual photo using the reference thermal 3D model (RT3DM), resulting in what is known as a synthetic view. For each of the N_i^r images, a synthetic image S_i is created using its camera pose $[R_i^{ir} | t_i^{ir}]$.

$$S_i = S(P, [R_i^{ir} | t_i^{ir}]) \quad (5.5)$$

Optimization of similarity metric

For each thermal image, the similarity is optimized in order to determine the refined camera pose. The similarity metric is the correlation between intensity values from the synthetic view and the 2D IR image. The correlation is calculated using only those pixels for which there is a value in the synthetic image:

$$R_i^{ir*}, t_i^{ir*} = \arg \max_{R_i^{ir}, t_i^{ir}} Corr(S_i, I_i) \quad (5.6)$$

The Nelder-Mead algorithm is used to optimize the similarity metric described above. This algorithm is widely recognized as one of the best methods for multidimensional optimization. The initial estimation of the IR camera pose serves as the starting point for the optimization algorithm. The termination tolerance is set at 10^{-8} , with a maximum of 1200 iterations. Figure 5.12 depicts the optimization process.

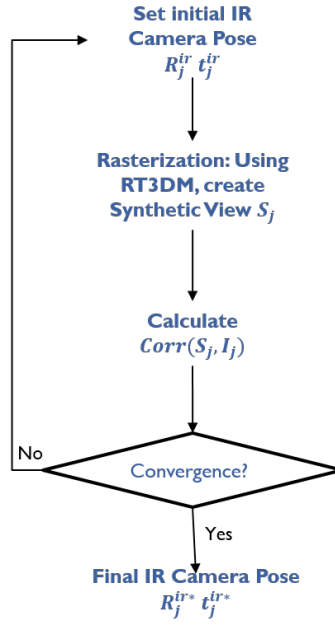


Figure 5.12: Optimization process carried out for each thermal view to refine camera pose.

On an Intel(R) Core(TM) i7-8750H CPU @ 2.20GHz 2.21 GHz computer, this algorithm takes an average of 7 seconds per thermal image.

5.4.3 Stage III: Fusion of several thermal views

Given the N_{ir} thermal views, each of the M points on the 3D model pointcloud have several temperatures that could be assigned to it. These temperature values can be represented in a matrix $M \times N_{ir}$ that represents all temperature values assigned to the point cloud from different views as follows:

$$Y = \begin{pmatrix} Y_{1,1} & Y_{1,2} & \cdots & Y_{1,N_{ir}} \\ Y_{2,1} & Y_{2,2} & \cdots & Y_{2,N_{ir}} \\ \vdots & \vdots & \ddots & \vdots \\ Y_{M,1} & Y_{M,2} & \cdots & Y_{M,N_{ir}} \end{pmatrix} \quad (5.7)$$

To obtain a single measurement that combines the temperature of multiple views, a weighted average is calculated. The method used to combine the temperatures is a weighted average as proposed in 4.3 which takes into account the distance and angle between the camera and the captured scene surface. This approach reduces noise and improves temperature accuracy. A similar weighted average for fusion of multiple views has been previously employed in [95].

After combining the temperature measurements, we can estimate the temperature at any point i in the 3D model point cloud using the weighed average as in the following equation:

$$\bar{Y}_i = \frac{\sum_{j=1}^{N_{ir}} w_{ij}(\theta_{ij}, d_{ij}) Y_{ij}}{\sum_{j=1}^{N_{ir}} w_{ij}(\theta_{ij}, d_{ij})} \quad (5.8)$$

where $w_{ij}(\theta, d)$ is the weight for the point i in the image view j . j represents the camera view, with $j = 1, 2, 3, \dots, N_{ir}$ and i represents a point in the 3D model, with $i = 1, 2, 3, \dots, M$. The weight depends on the visualization angle (θ) and the distance between the camera and the point (d). Points with small distances and acute angles have higher weights than distant points with

larger angles. Specifically, points with distances smaller than 40cm and angles lower than 60° have weights greater than 0.5.

5.4.4 Evaluation of multi-view consistency

To assess that the images are consistency between the different views and, therefore, well aligned with the reference thermography, a multivariate measure of correlation is observed: the intraclass correlation coefficient is applied to the data structured in (5.7).

Given Y_{ij} , the values of temperature for a given i -th point in the 3D model point cloud, observed from j -th view. The temperature value can be modeled as follows:

$$Y_{ij} = \mu_i + \alpha_j + \varepsilon_{ij}$$

where Y_{ij} , is decomposed in three parts: a real temperature for each point μ_i ; an effect from j -th thermal view α_j ; and a random error for each point and thermal view ε_{ij} . Assuming independent effects between the components, the variance of temperatures in the point cloud could be expressed as follows:

$$\sigma_Y^2 = \sigma_\mu^2 + \sigma_\alpha^2 + \sigma_\varepsilon^2$$

Then, ICC is calculated as follows:

$$ICC = \frac{\sigma_\alpha^2}{\sigma_\alpha^2 + \sigma_\varepsilon^2}$$

where

- σ_α^2 : variance due to the different views.
- σ_ε^2 : variance due to random error.
- n = number of subjects;
- k = number of raters/measurements.

ICC is a scale-free measurement which varies from 0 to 1. When ICC is close to 0, it means there is a low correlation between different views values. In contrasts, when ICC is close to 1, there is consistency between different views; i.e. there is high correlation between values from different views.

5.5 Proof of concept on real wounds

Six wounds are analysed to demonstrate the feasibility of the presented methodology. The images of the patients' wounds were acquired in a hospital in France, where the acquisition protocol was performed in manual mode with instructions to take multiple views around the wound. The user acquired several views in front of the wound with an arc position movement to capture multiple overlapping views of the wound. With four thermal images in front of the wound, and one of the thermal images from further away. The thermal imaging camera is always placed on top of the smartphone to capture the photos, so we can always use the same geometric calibration. Figure 5.13 illustrates the six cases for which we show the result in this section.



Figure 5.13: Six cases of foot and lower extremity injuries used to show application of our algorithm for multi-view thermal 3D model creation.

5.5.1 Calibration-based thermal 3D models

For each model, we used passive reconstruction and applied a geometric transformation to the RGB camera pose to obtain the IR camera pose.

To perform multimodal stereo calibration, we captured 86 images of the chessboard pattern described in section 5.2 and used the open-cv package in Python for calibration. The resulting average reprojection error was 6.83 pixels, which represents 0.85% of the diagonal pixels. This error provides a baseline for comparison, and we anticipate that implementing geometric translation between cameras to estimate the IR camera pose will result in a similar level of error.

Using SfM with Meshroom, we obtained estimated camera poses for all N color views: N_{rgb} from the high resolution RGB camera and N_{ir} views from the thermal camera. We applied a geometric transformation by stereo calibration to each of the N_{ir} IR camera views, and then, we used raycasting to assign temperature values to the 3D point cloud. Figure 5.14 shows examples of the resulting calibration-based thermal 3D models created using this methodology.

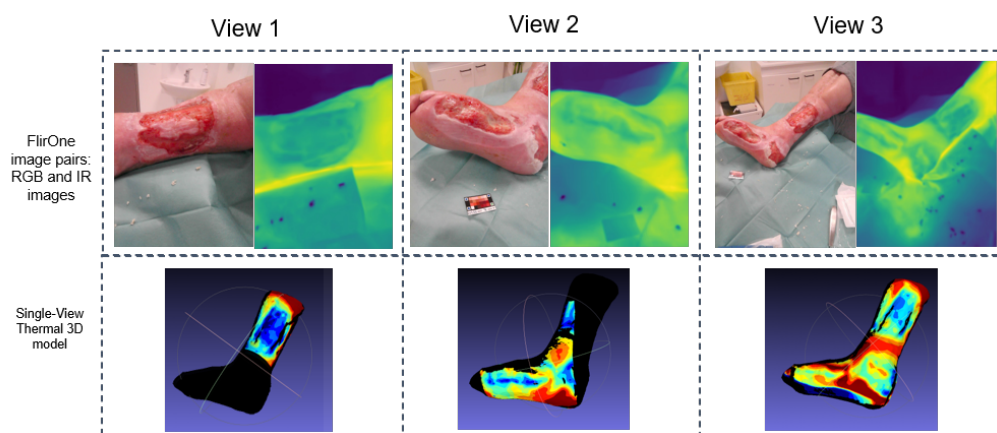


Figure 5.14: Calibration-based thermal 3D models created based on 3D models from passive reconstruction and initial infrared camera poses estimated by stereo multimodal calibration.

5.5.2 Thermal camera pose refinement

After creating the first calibration-based thermal 3D model, a camera pose refinement is performed. Using different visualizations, we demonstrate that the proposed refinement process improves the registration between the infrared images and the 3D colour model.

To refine the infrared camera pose, we compared the perspective view of the 3D model with its corresponding 2D thermography. Fig 5.15 shows four examples of 3D models viewed from the perspective of the estimated IR camera poses overlaid with raw thermal images. The initial IR camera pose estimation resulted in a visible mismatch between the object edges and those of the IR image, as shown in the images (top row). However, our proposed pipeline showed a qualitative improvement in edge alignment after IR camera pose refinement (bottom row).

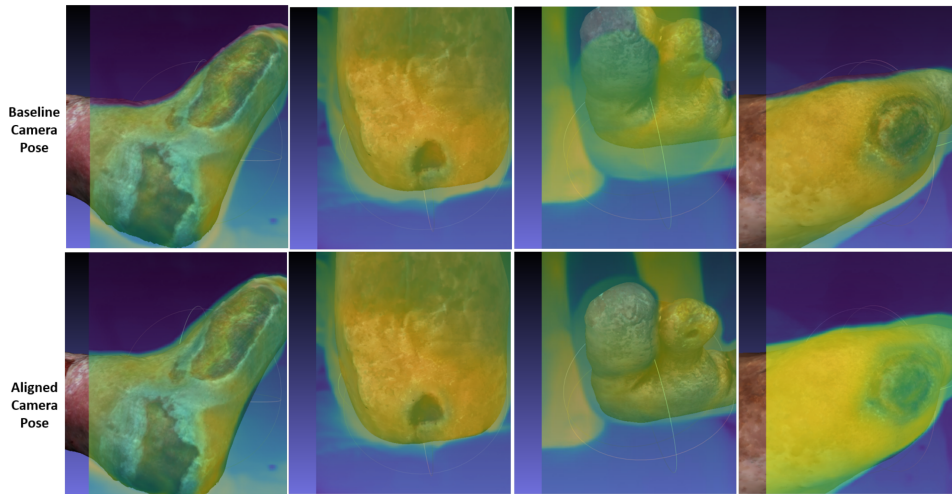


Figure 5.15: Example of thermal 3D registration before and after the IR Camera Pose Refinement

When comparing Synthetic Views Before and After Refinement, we can see that there is an improvement in thermography registration. In Figure 5.16, an example is shown. Two synthetic views of a foot area are shown. The synthetic views were created before and after refinement of the thermal camera pose. The alignment between the synthetic view and the real thermal image is improved after the camera pose refinement.

5.5.3 Multi-View Thermal 3D models

A comparison between the single-view and multi-view thermal 3D models reveals several advantages of the latter. With multiview thermography, thermal data can cover larger surfaces, resulting in more comprehensive 3D models. Figure 5.17 provides a visual comparison of the results obtained using single and multiple thermal views. It demonstrates the benefits of the multiview approach and its suitability for large as well as small wounds.

Finally, the methodology has been applied to all six cases, and the results are shown below. Figure 5.18 shows the resulting color 3D model and thermal 3D model obtained using the methodology presented for creating thermal 3D models.

To evaluate the consistency achieved within multi-view thermography by different views, we used the Intra-Class Correlation Coefficient (ICC) as described in Section 5.4.4 before and after the refinement of the IR camera pose.

We observed an improvement in ICC for cases where the ICC was initially low ($ICC \leq 0.65$) before the refinement. However, for those with high ICC, the refinement process improved slightly (<0.1 improvement), and only one case with high ICC decreased from 0.89 before to 0.78 after

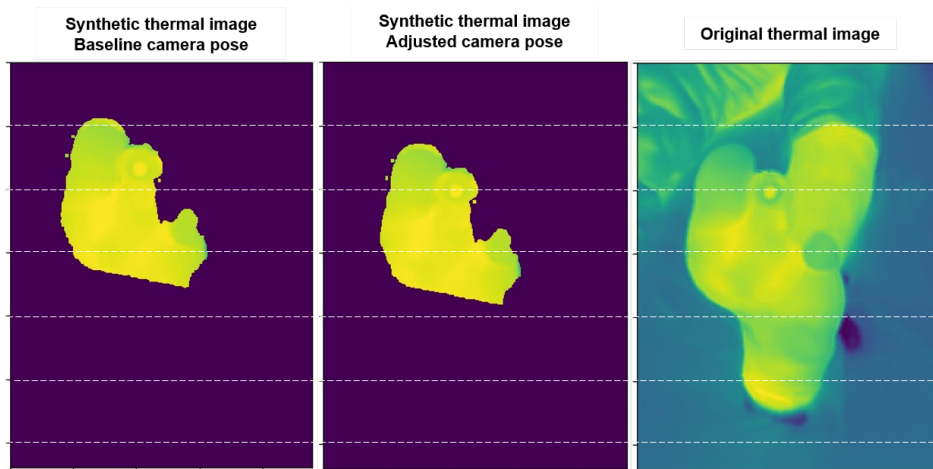


Figure 5.16: Illustration of synthetic thermal images created by projecting the reference view model using the baseline (left), the adjusted IR camera pose (center), and the original thermal image (right). The dashed horizontal lines show that the synthetic images are in better alignment with the actual thermal image when the camera pose is adjusted.

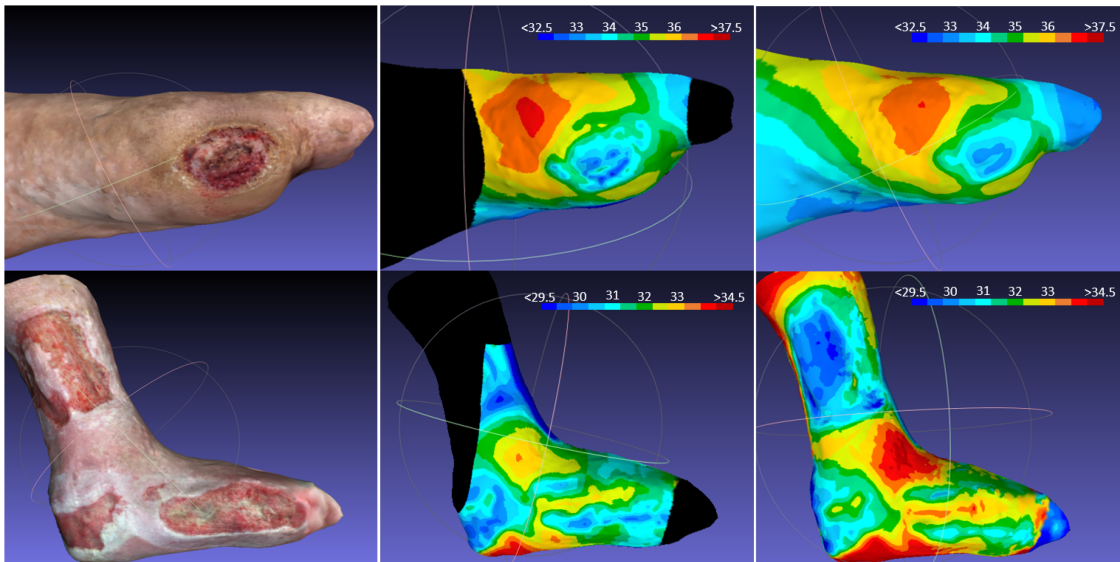


Figure 5.17: Two examples of calibration-based thermal 3D models and their corresponding multi-view thermal 3D models. Multi-view thermal models created with the proposed methodology.

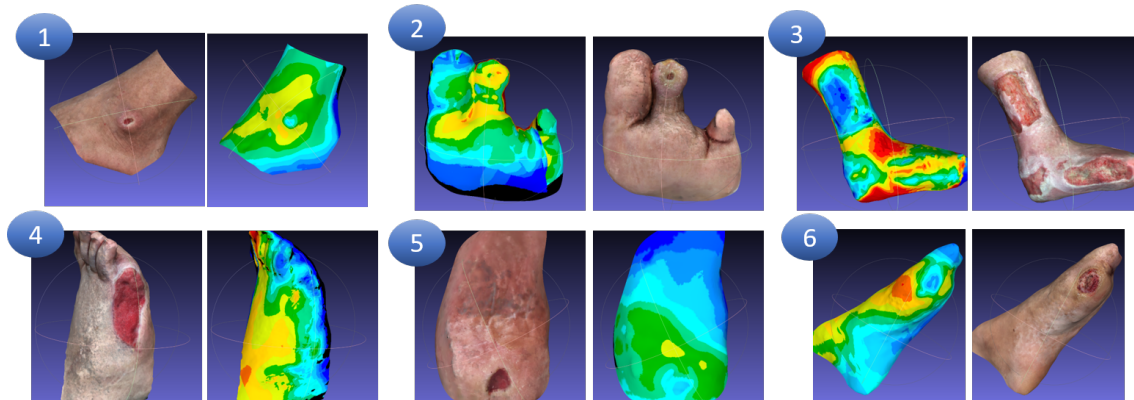


Figure 5.18: Six cases were chosen to show the thermal 3D creation.

refinement. Table 5.3 presents the results on ICC before and after the camera pose refinement process.

Table 5.3: Intraclass Correlation Coefficient (ICC) before and after the refinement of thermal camera poses. Last columns shows the relative change in ICC.

Patient	Location	Area	No. points in 3D model (M)	ICC		ICC Change
				Before	After	Difference
P1	Ankle	1.49	247997	0.42	0.66	0.24
P2	Toe	0.80	156712	0.87	0.94	0.07
P3	Multiple	25.43	123347	0.89	0.78	-0.11
P4	Lateral	4.49	210024	0.27	0.91	0.64
P5	Calcaneus	2.47	189054	0.93	0.94	0.01
P6	Lateral	9.29	70493	0.65	0.97	0.32

5.6 Discussion

Thermography, a technique for evaluating wounds, has gained increasing interest in recent years. Using two-dimensional (2D) thermography restricts the evaluation to a single viewpoint. In addition, 2D thermography for wounds requires a manual definition of regions of interest to obtain quantitative metrics for wound assessment. Furthermore, the thermal accuracy changes depending on the angle and distance between the camera and the wound. Given the current limitations of 2D thermography, alternative approaches such as thermal 3D modeling are more interesting for wound evaluation.

The literature review of thermal 3D models for skin and wounds shows that the various systems proposed for creating thermal models rely on high-cost devices and fixed cameras. Thus, many of them are not practical for hectic clinical environments. Moreover, most thermal 3D models generally use a single view, which leads to a decision regarding the scanning coverage and the thermal resolution targeted. However, in curved areas, neither option would be feasible to assess the entire area and its surroundings with a single view.

Therefore, this chapter presents a methodology for creating thermal 3D models from digital images. No complex equipment is required: acquisition with low-cost commercial devices is proposed. Our methodology focuses on the use of low-cost portable devices, in contrast to previous approaches that require specialized equipment. By relying on readily available digital images, the proposed methodology enables an affordable and accessible solution for thermal 3D modeling.

Our proposed thermal 3D model improves the thermal estimation of thermography by synthesizing information from multiple-view thermal images, which is a contrast to previous thermal 3D modeling systems that typically use a limited number of thermal views. Furthermore, our approach uses passive reconstruction and refinement of camera poses, an alternative to most previous work's expensive active reconstruction techniques. It only requires digital images acquired with a portable device like a smartphone and a commercial portable dual-sensor thermal camera.

Our study results demonstrate that our proposed methodology can generate high-quality thermal 3D models from images captured using low-cost devices. By creating a multi-view thermal model, we address the trade-off between scanning surface area and thermal resolution, which is commonly observed in single-view thermal images. Combining multiple thermal views obtained at varying distances, we enlarge the scanning area while preserving detailed thermal information on the surface. Furthermore, integrating thermal views from multiple perspectives and distances enhances temperature accuracy, leading to more reliable and precise temperature estimation, as demonstrated in Chapter 4.

The employed refinement methodology demonstrates the capability to improve camera poses. However, the table presented in Section 5.3 shows that the refinement is most useful for thermal views with no consistency among them, i.e., where the thermal views are not consistent across different views. Inconsistency in the views when using a calibration-based thermal 3D model can lead to varying and non-repeatable thermal metrics. In the case of multiple views, the camera poses are adjusted, and the thermography of the multiple views is combined, leading to stable and robust thermography metrics.

Finally, the proposed methodology has the potential to be implemented in use cases beyond wounds and skin due to several key factors. Firstly, passive reconstruction can be used for any object as long as the scene is static with no movement and the surface is not reflective. Secondly, stereo calibration only depends on the device, so it can be used in any other case. Finally, refinement does not rely on the silhouette but rather on the variability of temperatures on the surface. As such, it can be applied to surfaces with variable temperatures.

5.7 Conclusion

This chapter presents a methodology for creating multi-view thermal 3D models for wound evaluation. In addition, a comprehensive literature review on previous systems for creating thermal 3D models has been included, providing a detailed overview of the state-of-the-art in the field. The chapter also details the process of stereo camera calibration, which is an important step in creating accurate thermal 3D models. Overall, the chapter thoroughly analyzes the methodology used to create thermal 3D models for wound evaluation, including a review of previous work and a detailed description of the proposed methodology and calibration process.

Our proposed methodology employs passive 3D reconstruction and camera pose refinement to create a multi-view thermal 3D model. This approach offers several advantages, including an increased surface area coverage compared to calibration-based thermal 3D models. Additionally, camera poses estimation from multiple IR views is refined using a reference thermal 3D model, resulting in more accurate and reliable models. One of the key benefits of our proposed methodology is that it can be implemented using low-cost devices, such as a smartphone or mobile device, along with any dual-sensor (IR-RGB) portable thermal camera like the FlirOne Pro. This makes the technology accessible to a wide range of users, including healthcare professionals in low-resource settings.

Furthermore, using portable and user-friendly devices for image acquisition makes our proposed methodology more accessible than previously proposed models, enabling its application in areas with limited medical resources. This approach offers a promising solution for objective and affordable wound assessment and monitoring. Moreover, our methodology has the potential to be applied to other areas besides wound assessment, as there are no limits on the acquisition, and it

could be suitable for larger surfaces. This versatility opens up opportunities for the application of our proposed methodology in different fields where portable thermal 3D modeling is necessary.

Chapter 6

Clinical Application

Contents

6.1 Towards automated creation of thermal 3D models	67
6.2 Quantitative wound measurements	70
6.3 Experimental Setup	72
6.4 Evaluation of thermal 3D models and metrics	76
6.5 Discussion	80
6.6 Conclusion	82

In the previous chapter, an algorithm was presented for creating thermal 3D models from 2D thermal and color images acquired with affordable and portable devices. Given the purpose of its application in clinical scenarios, this chapter proposes a detailed pipeline for the automated creation of thermal 3D models. The implementation of our proposed system to create thermal 3D model has been demonstrated on 68 cases of wound in a real clinical setting. This clinical study surpasses the sample size of previous studies that report the usefulness of 3D thermal models on skin or wounds but only show their results on small samples composed of less than 5 cases [12, 63].

This chapter is structured as follows: In section 6.1, the details of the automated process to create thermal 3D models are described. In section 6.2, the quantitative measurements relevant to the wound assessment are described. Next, in Section 6.3, the experimental setup for the clinical study and the acquisition protocol are described; followed by Section 6.4, where results of the implementation on real patients are presented with a detailed analysis of the thermal metrics and their relevance for chronic wound assessment. Finally, Section 6.5 presents a discussion on the prospects for clinical integration, and Section 6.6 concludes with a summary of the chapter.

6.1 Towards automated creation of thermal 3D models

In order to create thermal 3D models in an automatic process, additional methodologies have been implemented to automate the thermal 3D model creation process.

These additional processes are incorporated into the thermal 3D model creation process described above in 5.4. They include image preprocessing for the removal of non-relevant background objects in the images, postprocessing of the color 3D model, and finally the creation of geometric and thermal metrics from the thermal 3D model. Figure 6.1 shows an overview of the process of automatic thermal 3D model creation.

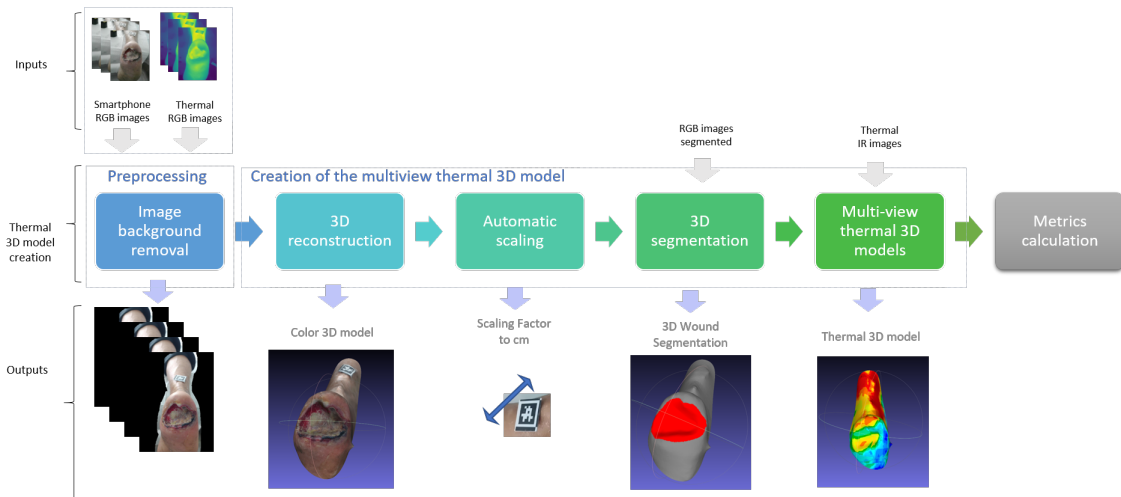


Figure 6.1: Pipeline for automated creation of thermal 3D models.

6.1.1 Background Removal

The Structure from Motion (SfM) technique involves performing 3D points triangulation based on feature detection and matching between several points of views. However, when capturing images from different perspectives in handheld mode, several background objects can inadvertently appear on the images.

In a clinical environment, images often include non-interesting surrounding objects, such as the bed, clothing, other body parts, and medical equipment, which are not useful for wound analysis. Moreover, detecting and matching these non-useful background objects can consume resources and slow down the creation of thermal 3D models. To address this issue, a pre-processing step for removing surrounding background objects has been implemented. This step utilizes a U-network deep learning model previously used by the STANDUP project. The model was trained and applied as a helper to assist in wound segmentation tasks in previous studies of the STANDUP project [66]. The skin segmentation model was applied on raw color images to obtain a skin mask, a binary mask that detects the skin and rejects the background. Subsequently, a mask dilation with a kernel of 10x10 was performed to avoid eliminating misclassified skin edges as could be seen in Figure 6.2.



Figure 6.2: Automatic background removal procedure by deep learning based skin segmentation: raw RGB image (left) and the corresponding image after applying background removal (right).

This process leads to efficient removal of surrounding objects, as well as improved processing time and 3D reconstruction. Fig 6.3 shows the 3D model results after applying background removal in various examples. Moreover, a quantitative evaluation of this pre-processing on 5 wound cases shows a reduction in processing time by 17% on average, with a reduction in the 3D model repro-

jection error (root mean square error, RMSE) by 9% on average.



Figure 6.3: Example of 3 cases where the background removal treatment was applied. Baseline 3D models with reconstructed background objects (top) and corresponding 3D models once the background removal process is implemented (bottom).

6.1.2 3D model scaling

After 3D modeling by SfM, the color 3D model has an arbitrary scale. Therefore, to convert the 3D model scale to a real-world scale in centimeters, a scale factor is applied.

The scale factor is calculated by using a reference object with a known size placed near the patient's skin. The reference object chosen is an ArUco markers as state-of-the-art algorithms already exist for efficient detection of the object. The reference object is kept close to the wound and should be visible in at least two of the images captured.

AruCo detection for RGB images is implemented using OpenCV within python. Once corners of the ArUco marker are detected in 2D images, raycasting is used for finding corresponding points in the 3D model. The size of the square ArUco marker is calculated in the 3D model and compared to the real size of the ArUco in centimeters. Mathematically, the scaling factor calculated with j -th RGB image is denoted as SF_j and is computed as follows:

$$SF_j = \frac{\hat{d}_j^{3D}}{d^{Real}} \quad (6.1)$$

where \hat{d}_j^{3D} is the estimated size of the square in the 3D model using AruCo corner detection from the j -th image. d^{Real} is the actual size, in centimeters, of the ArUco marker. In our case: $d^{Real} = 2.2cm$.

Finally, a single scale factor is calculated averaging the scaling factors obtained from several N views as follows:

$$ScalingFactor = \frac{\sum_{i=1}^N SF_i}{N} \quad (6.2)$$

Fig 6.4 shows the detection of the ArUco markers in 2D and 3D space. The detected corners are used to calculate the scale factor.

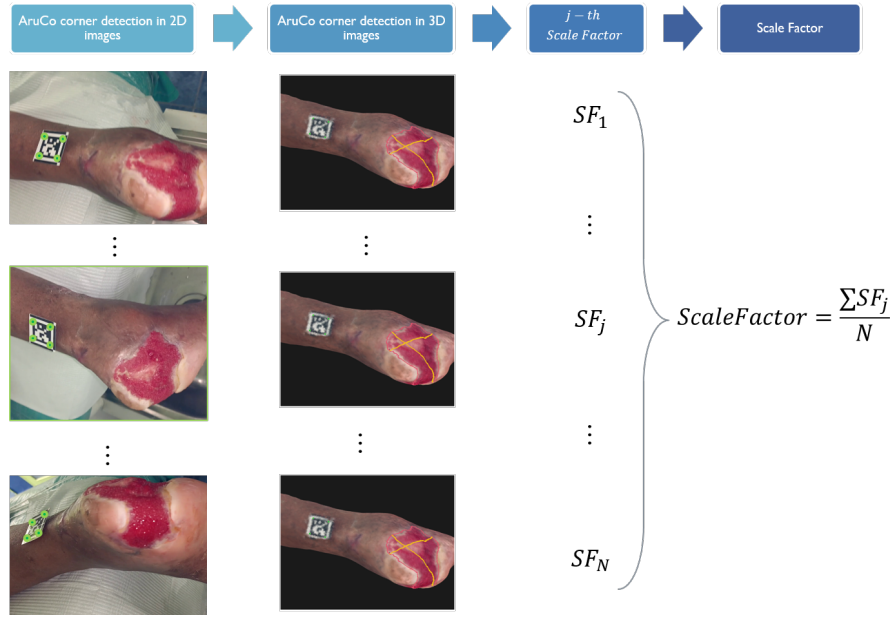


Figure 6.4: Illustration of Aruco markers detection process and computation of the scale factor.

6.1.3 3D wound segmentation

Wound segmentation in the 3D model was created from 2D color image segmentation, which was performed by applying a deep learning model previously developed in the STANDUP project [76].

The 2D segmentation of multiple views are reprojected onto the 3D mesh using the extrinsic RGB matrix and raycasting. Then, points on the 3D mesh are assigned to wounded or unwounded based on the majority vote of the multiple reprojected views. The idea of using majority vote strategy comes from a previous study on multiview classification [98]. Fig 6.5 depicts an example of the 3D wound segmentation from 2D images.

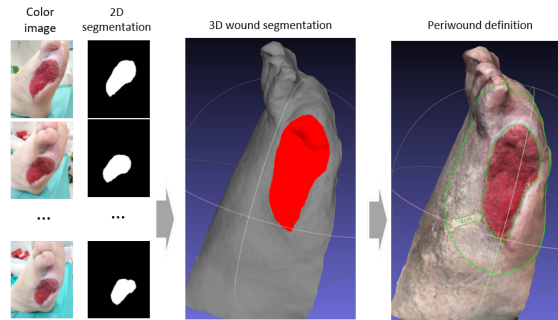


Figure 6.5: Ilustración de la segmentación en imágenes 2D, y su resultado en el modelo 3D de una herida.

6.2 Quantitative wound measurements

In this section, we provide the definitions of geometric and thermal metrics, which will be later analyzed in Section 6.4.

6.2.1 Evaluation regions

As highlighted earlier in Chapter 1, evaluation regions beyond the wound, such as the wound edges and periwound, are important for wound assessment. In this section, we provide an objective definition of such regions in the 3D model in order to subsequently use them in the calculations of the thermal metrics.

Wound Edges (WE)

Based on a 3D segmentation of the wound, the wound edge (WE) is the region surrounding the wound, limited to a width of 0.5 cm. This area clearly separates the wound bed and the periwound area.

Periwound (PW)

The periwound region has been into the focus of research as it has the potential to provide thermal metrics for wound assessment. This region is defined as the adjacent area located within a geodesic width of up to 4 cm from the wound edges, as proposed by Dowsett et al. [33]. The use of a geodesic distance from the wound edges is a critical factor in the definition of the periwound area, as it enables the consideration of the complex three-dimensional (3D) structure of the wound and its surrounding tissue.

Normal Skin (NS)

The region of normal skin, characterized by the absence of visible signs of injury, is defined as the area adjacent to the periwound. Although there are no fixed criteria for the extent of normal skin, a width of up to 4 cm from the wound edge has been selected to capture a representative sample of the surrounding tissue. This width is similar to the periwound area and provides a balance between obtaining adequate baseline temperature information and ensuring that the region is of sufficient size to provide meaningful information while avoiding an overly wide or diffuse extent.

Figure 6.6 depicts the 3D segmentation of the wound model, including the wound bed, wound edges, periwound, and normal skin regions previously described.

While the region size parameters have been established for the purposes of this thesis based on general guidelines and considerations, it is important to acknowledge that they are open to adaptation in future applications as deemed appropriate by the treating physician.

6.2.2 Wound surface area

Once the wound has been segmented in the 3D model, the calculation of the wound area is a straightforward process. It consists of adding the area of the triangles corresponding to the wound bed area obtained by the segmentation process described above. With this method, a more realistic measurement of the wound surface can be obtained, as it takes into account the curvature of the area and, therefore, can provide more detailed indicators for wound assessment and follow-up.

6.2.3 Thermal metrics

Temperature metrics, including temperature differences between evaluation regions and wound variability within regions, have previously been studied in the assessment and prognosis of chronic wounds [23, 65, 27, 26]. Therefore, six thermal metrics have been created. The first three metrics serve to analyze the temperature differences between evaluation regions (i.e. wound, periwound, and normal skin), while the last three metrics are intended to analyze temperature variability within each evaluation region. These metrics are defined above:

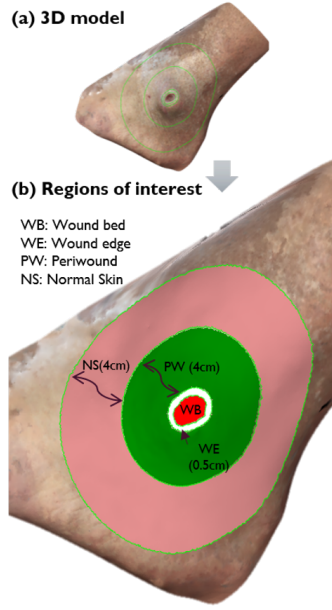


Figure 6.6: Depicted in the 3D model are the distinct regions of skin, including the wound bed, wound edges, peri-wound, and normal skin.

- T_{WB-PW} : Calculated and expressed in Celsius ($^{\circ}\text{C}$), this metric provides information on the temperature of the wound bed relative to that of the peri-wound. A value greater than zero indicates that the temperature of the wound bed is higher than that of the peri-wound.
- T_{WB-NS} : Temperature difference between wound bed(WB) and normal skin(NS) in $^{\circ}\text{C}$, is calculated and expressed in Celsius ($^{\circ}\text{C}$). This metric provides information on the temperature of the wound bed relative to that of the normal skin.
- T_{PW-NS} : Temperature difference between peri-wound(PW) and normal skin(NS), is calculated and expressed in Celsius ($^{\circ}\text{C}$). This metric provides information on the temperature of the peri-wound relative to that of the normal skin.
- CV_{WB} , CV_{PW} , and CV_{NS} : The coefficient of variation (CV) of temperatures within the wound bed (WB), peri-wound (PW) and normal skin (NS) respectively. CV quantifies the degree of temperature variation within each evaluation region, and is calculated as follows:

$$CV_{zone} = \frac{Std(T_{zone})}{Avg(T_{zone})} \quad (6.3)$$

where the *Zone* can be either wound bed (WB), peri-wound (PW) and normal skin (NS). $Std(T_{zone})$ is the standard deviation of the zone, and $Avg(T_{zone})$ is the average temperature on the zone.

6.3 Experimental Setup

The primary objective of the present study is to investigate the feasibility of employing portable devices to construct thermal 3D models in clinical settings. Furthermore, the study aims to evaluate the value of thermal metrics obtained from these thermal 3D models chronic wounds assessment.

The experiments were conducted between December 2021 and June 2022 at a private clinic in Lima, Peru, and were approved by the Ethics Committee of the Pontificia Universidad del Peru.

Patients with an open wound who were undergoing treatment and agreed to participate in the study were included in the data collection process, while patients without a wound were excluded. An experienced clinic assistant, who had received specialized training in image acquisition, performed the data acquisition process.

In this section, we describe the research protocol in clinical environment, as well as provide detailed information on the image acquisition process.

6.3.1 Research protocol in clinical environment

The standard protocol for evaluating wounds typically begins by instructing patients to rest in a comfortable position and cleaning the affected area. Subsequently, healthcare providers proceed to qualitatively assess the wound and document their observations, followed by necessary treatment.

Our data acquisition process adheres to the aforementioned initial steps of patient positioning and wound cleaning. Before initiating image acquisition, patients who consent to participate are informed and asked to remain in a comfortable and still position for five minutes to minimize motion blur. This is important for achieving accurate correspondence between the images in the Structure from Motion (SfM) algorithm.

To ensure visual clarity and accurate documentation in the 3D model, the wound area should be free of bandages and creams. If necessary, any residual bandages or creams can be gently removed with warm water. After cleaning, the patient should rest for five minutes to allow the wound and surrounding skin to equilibrate to ambient temperature.

The subsequent image acquisition process involves capturing images with both a mobile and a thermal camera. More details on image acquisition are given in Section 6.3.2. After the images are collected, healthcare providers can continue with qualitative evaluation and treatment of the wound.

6.3.2 Data Acquisition

The complete acquisition workflow is depicted in Figure 6.7

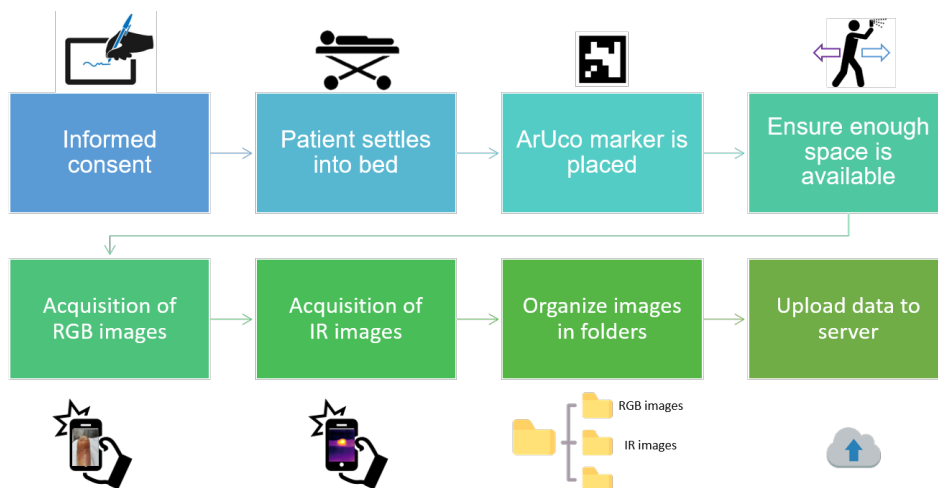


Figure 6.7: Workflow for image acquisition in the clinical environment

Devices

The acquisition of images was performed using a smartphone Xiaomi Redmi Pro 10, and a FlirOne Pro thermal camera(FLIR Systems, Inc., Oregon, USA). The thermal camera was attached to the

smartphone as shown in 6.10. The smartphone camera captures images at a high resolution of 4000x3000 pixels, while the FlirOne Pro thermal camera captures two images at the same time: an RGB image and a IR image, both saved in a unique radiometric JPG file. The RGB image has a resolution of 1080x1440 pixels, and the IR image has a resolution of 480x640 pixels. The thermal sensor of the FlirOne camera has a spectral range of 8 – 14 μ m, a thermal sensitivity of 70mK, and a thermal accuracy of $\pm 3^{\circ}C$ or $\pm 5\%$, according to the manufacturer.

Device - Sensor	Resolution
Smartphone - RGB	3000x4000px
FlirOne Pro - RGB	1080x1440px
FlirOne Pro - IR	480x640px

The mobile device has been a smartphone in this study. However, as previously reported in Section 2, SfM 3D models can be created with any other digital camera with similar resolution can be used, such as those found in tablets.

Reference Card

An easy-to-detect reference card was also used to adjust the 3D size to a true centimeter scale. The reference card can be any object for which at least two points of known distance are known. It will be used to adjust the 3D scale to real scale in *cm*.

Initially, a colored rectangular marker was used for this purpose. However, we switched to using the Aruco marker after a month, since the ArUco marker has algorithms implemented to detect its four corners in a efficient way [37].

The fiducial marker is placed on the clean skin or on the wound bed, close to the wound, in a position where it is visible when the photographs are taken. At least two images must contain the ArUco marker so that it can be reconstructed in the 3D model.



Figure 6.8: A sample of an ArUco marker. The ArUco marker is easy to detect by well known algorithms implemented in opencv.

Image acquisition

To create thermal 3D models for wound evaluation, the protocol for acquiring thermal and color images is done using low-cost cameras in handheld model. The acquisition procedure builds upon previous studies on 3D photogrammetric reconstruction for wounds [25, 107], but with the addition of thermal imaging to the acquisition protocol. The acquisition process consists of two phases: RGB image acquisition and thermal imaging acquisition. The details for each process are described below.

1. RGB image acquisition: To build the color 3D model, the operator captures various different overlapping views of the wound with a smartphone, using a traditional passive reconstruction protocol. The camera is placed about 20-30 cm in front of the wound, and the operator captures images in a circular motion, ensuring the images are in focus on the wound. The number of images requested is 20 images. However, It's important to note that the operator could take a few more color or thermal images than requested inadvertently, which is not a problem and can improve the quality of the 3D models. In general, the more images, the

better the quality of the 3D model, although it will require more time to process the images. It is even possible to create 3D models with only 2 images.

2. Thermal imaging acquisition: With the thermal camera, a similar procedure is followed. The thermal camera is placed about 20-30 cm in front of the wound, and the operator captures at least 4 different overlapping views. In addition, an additional thermal image is captured from a greater distance (between 30 and 40 cm) to provide a broader thermal perspective of the wound and the surrounding skin. This distant image is used as the reference view in the thermal 3D model algorithm described in the previous chapter.

The goal of the different thermal images is to capture the thermography of the wound and surrounding area from different perspectives and map resulting temperatures onto the surface of the 3D model. While more images from different views could be useful to cover a larger area of the 3D model with thermography, the number of images was not controlled and only used as a reference for the acquisition. Figure 6.9 depicts the acquisition that should be performed in two steps: first with the mobile camera and then the acquisition with the thermal camera.

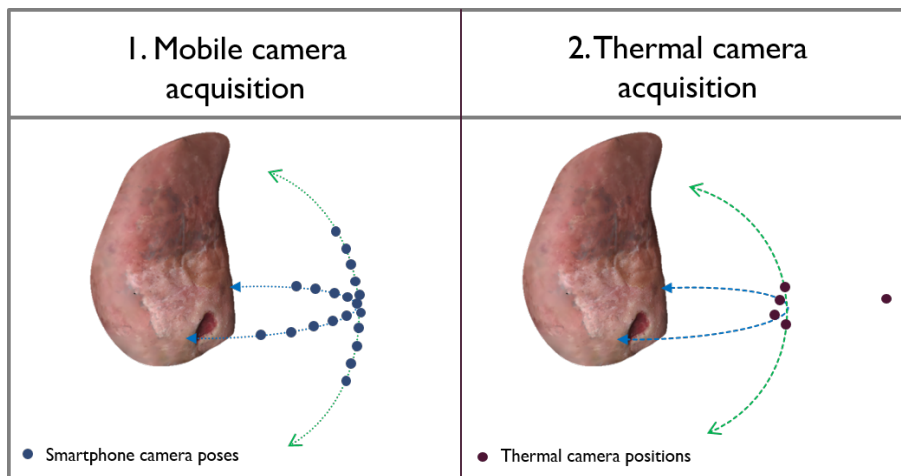


Figure 6.9: Acquisition configuration proposed as a reference. First, acquisition is performed with the high-resolution camera of the mobile device in two circular motions in front of the wound. Next, a small thermal image is acquired with the thermal camera in a similar motion, and a thermal image captured from further away.

The process of acquiring images for wound monitoring is generally straightforward and allows for flexibility in the number of images needed.

Operator

Since the acquisition procedure depends on the operator's ability to take photographs, user acquisition training is conducted. First, a training is conducted in an office with an uncluttered environment. Then, another training is conducted in the clinical environment. Figure 6.10 shows an example of handheld acquisition in an uncluttered environment with an artificial wound phantom.

Since the acquisition is manual and therefore the camera positions are not controlled, the camera positions may differ from those presented in Figure 6.9. This is not a problem for the creation of 3D models with the SfM algorithm.

6.3.3 Database

Each acquisition of images performed on a wound is called a visit. Images of each visit are processed to create the thermal 3D model; some patients have been captured more than once.

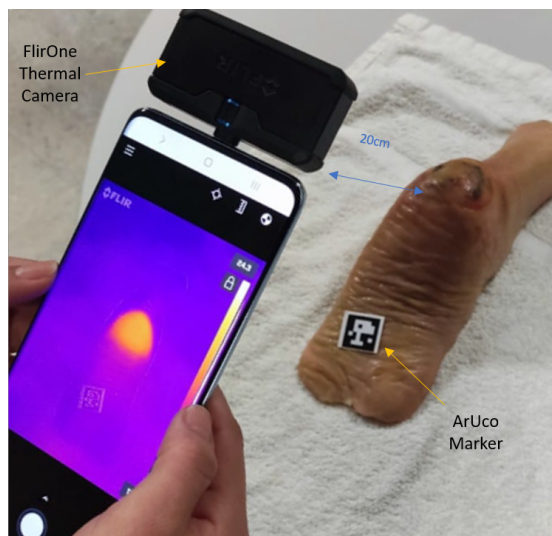


Figure 6.10: Illustration of handheld image acquisition using portable devices in clinical settings for creating thermal 3D models of wounds.

In total, the database is composed of 68 processed visits, which correspond to 32 volunteers. From those, 13 patients have been captured more than once, i.e. they have various visits over time.

Thermal 3D models were used to calculate geometrical and thermal metrics as described in the 6.2 section. Wound surface area ranged from 0.4 cm^2 to 139.4 cm^2 , with a mean surface area of 27.75 cm^2 and a standard deviation of 28.7 cm^2 .

The wounds were located in different areas of the foot and leg: sole, heel and edges of the foot; and 58 visits (75%) had been previously undergone any amputation, generally of one or more fingers or toes.

Wound classification according to the Wagner wound classification system was performed manually for each wound case. Wagner's wound grading system was described previously in Section 1.3.1. Wound grading was distributed as follows: 16 (23.5) cases had grade 4 wounds, 23 cases (33.8%) grade 3 wounds, 24 cases (35.3%) grade 2 wounds and 5 cases (7.4%) grade 1 wounds. This is shown in Table 6.2

Table 6.2: Distribution of wound grades in the 68 thermal 3D models processed.

Wound grading	Freq	%
Grade 1	5	7%
Grade 2	24	35%
Grade 3	23	34%
Grade 4	16	24%

6.4 Evaluation of thermal 3D models and metrics

In Figure 6.11, we could observe the color and thermal 3D models created for various wound stages and sizes. This demonstrates the feasibility of creating the multi-view thermal 3D model with our proposed methodology, specially in clinical environment.

For each visit, the acquisition of images takes less than 5 minutes. On the other hand, the processing time for creating thermal 3D models for each visit is in average 15 minutes using a Intel i7-12650H

CPU (16 cores), 2.3 Ghz (Hyper-Threading 3.6 Ghz) 16 GB DDR5 RAM (4800 Mhz); a Nvidia GeForce Rtx 3060 6GB GPU; 512 GB Disk memory (NVNe SSD), and O.S. Windows 11.

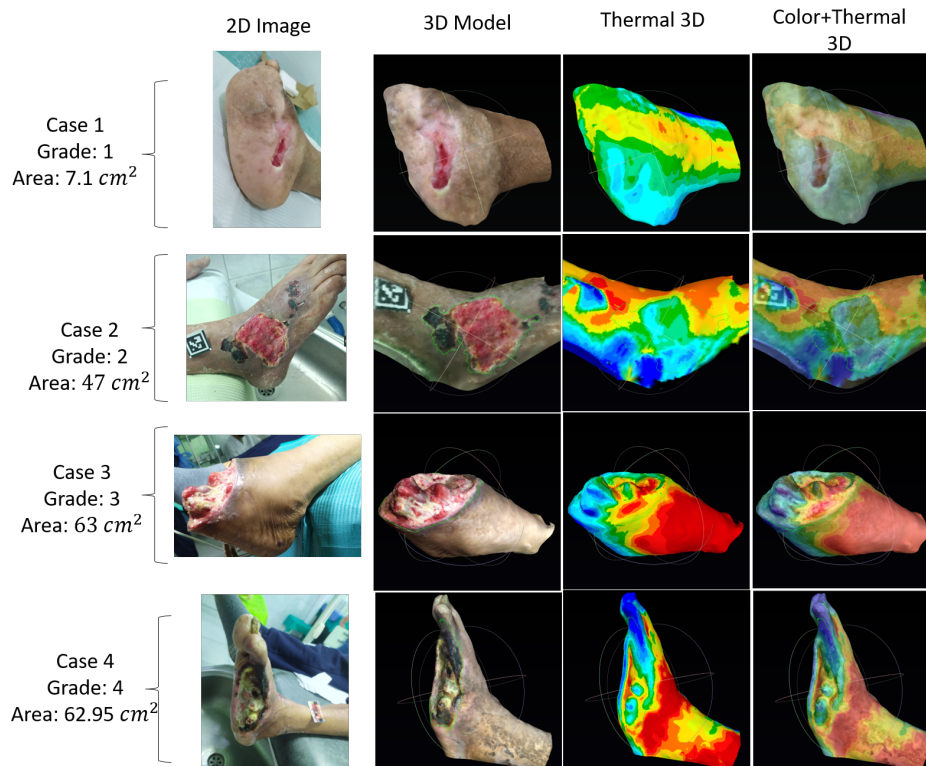


Figure 6.11: Examples of 3D color and thermal models created for three different wound sizes and wound grades. In each case, color 3D models (left), thermal 3D models (center) and blended color and thermal 3D model visualization (right) are displayed.

The system demonstrated to be straightforward, requires minimal resources and can provide 3D thermal models in clinical settings, including remote areas or at home. In terms of time, a processing time of 15 minutes per model, leads to about 4 hours of processing for a maximum of 16 acquisitions per day, assuming patients each 30 minutes during a work day of 8 hours.

In addition to assessing the feasibility of creating 3D thermal models with the proposed automated process in clinical settings, An analysis of the relevance of thermal metrics is performed.

6.4.1 Relevance of thermal metrics for wound assessment

The six thermal metrics obtained from the thermal 3D model are analyzed to test its relevance in wound evaluation.

First, we explore the temperature difference metrics. From 6.3, we observe that difference between the periwound and normal skin vary between positive and negative results; i.e. our sample is composed of patients with higher temperature in the periwound compared to the normal skin, as well as patients lower temperature in the periwound, compared to normal skin.

Table 6.3: Statistics for temperature differences, including the mean and its 95% confidence interval (CI). The final column displays the p-value obtained from a t-test that was used to determine whether the temperature differences between evaluation regions are statistically different from zero.

Difference	mean	ci95	pval
T_{PW-NS}	-0.64	[-0.99; -0.3]	0.00043
T_{WB-NS}	-0.93	[-1.45; -0.42]	0.00056
T_{WB-PW}	-0.29	[-0.69; 0.11]	0.15104

In contrast, a significant difference was found between the average wound temperature and the average temperature of normal skin, which suggest that our database is composed mostly of cases where average wound bed has lower temperatures than the periwound and normal skin. On average, the wound temperature was 0.93°C lower than the normal skin temperature. Average wound bed temperature was also significantly lower than the periwound temperature, with the wound bed temperature being 0.64°C lower on average.

Temperature difference metrics were also evaluated in relation to the Wagner’s wound grading. Figure 6.12 presents box plots that show the distribution of thermal metrics grouped by wound staging.

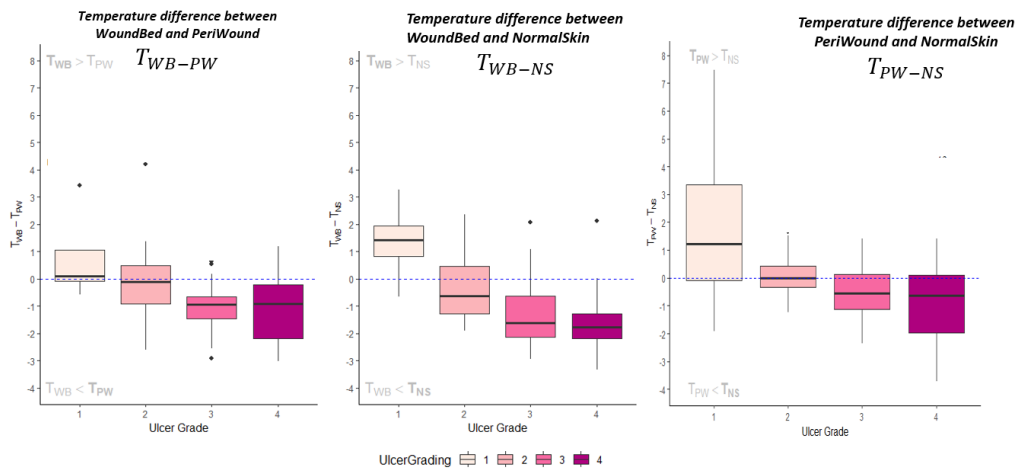


Figure 6.12: Distribution of temperature differences for different grades of wounds. The wound grade corresponds to the Wagner classification for diabetic wounds.

From this figure, a difference in metrics between grading is noticeable. Specifically, the periwound temperature is slightly higher than the temperature of normal skin in grade 1 wounds. Conversely, the periwound temperature is lower than the normal skin temperature in grade 3 and 4 wounds. In grade 2 wounds, the periwound temperature and normal skin temperature are similar on average. When analyzing the temperature difference between wound bed and normal skin, a similar trend is observed. Lower wound bed temperatures are associated with severe wound stages. Table 6.4 demonstrated significant differences in differential thermal metrics by one-way ANOVA.

Table 6.4: ANOVA test results for each temperature difference metric, to test for significant differences between wound grades.

Response	Mean Sq BetweenGroups	Mean Sq Residual	F-value	p-val
$T_{WB} - T_{PW}$	8.6077	1.6635	5.1744	0.002600
$T_{WB} - T_{NS}$	18.4456	2.7901	6.6111	0.000573

Response	Mean Sq BetweenGroups	Mean Sq Residual	F-value	p-val
$T_{PW} - T_{NS}$	3.8009	0.8375	4.5382	0.005306

On the other hand, Table 6.5 presents the basic statistics for the temperature variability metrics. Overall, the metrics on the coefficient of variation (CV) of temperatures are less than 20%, with a right-skewed distribution. The CV of wound bed temperatures is found to be the lowest compared to the CV of periwound (PW) temperatures and normal skin (NS) temperatures.

Table 6.5: Statistical analysis of the coefficient of variation (CV) metrics obtained from thermal 3D models created for 68 wound cases. The table presents each evaluated metric along with its basic statistical measures, such as minimum value, quartile 1, median, mean, quartile 3, and maximum.

Metrics	Min	Q1	Median	Mean	Q3	Max
CV_{WB}	0.004	0.025	0.036	0.041	0.050	0.178
CV_{PW}	0.009	0.044	0.063	0.069	0.086	0.178
CV_{NS}	0.003	0.042	0.064	0.070	0.084	0.193

Coefficients of variation within evaluation regions, were also analyzed with wound grade. The KS test was applied to determine if there were significant differences in the metrics between the different wound grades. The results demonstrated a significant difference in the CV of wound bed temperature: the higher the wound grade, the greater the variability of temperatures within the wound. No statistically significant differences were observed for other CV metrics. Table 6.6 presents the p-values obtained by Kruskal Wallis test.

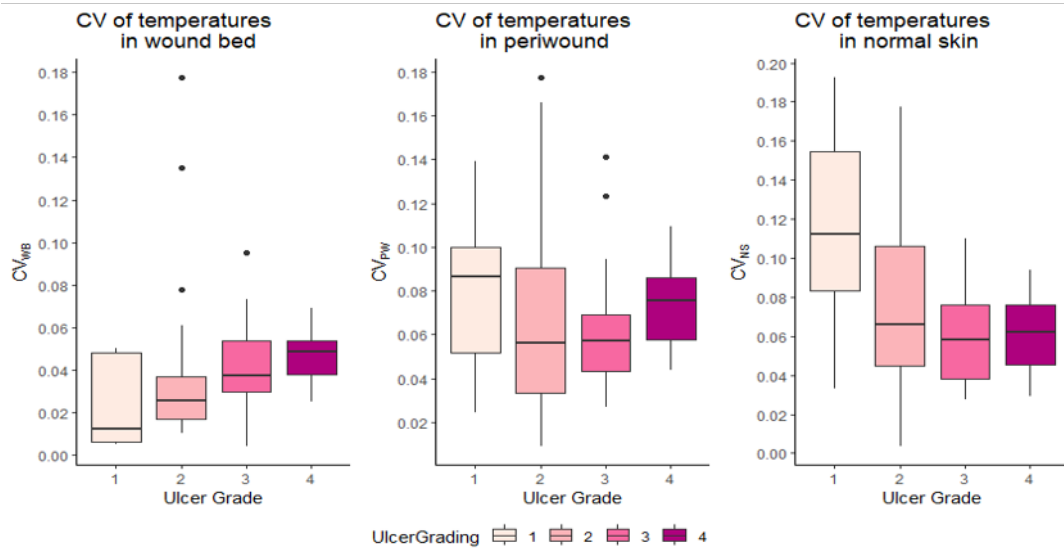


Figure 6.13: Distribution of temperature differences for different grades of wounds. The wound grade corresponds to the Wagner classification for diabetic wounds.

Table 6.6: Kruskal Wallis test results to assess whether thermal variability is significantly different between wound grades.

Metric	Median	Kruskal-Wallis Chi-squared	p-value
CV_{WB}	0.036403	10.7590	0.01311
CV_{PW}	0.063138	3.1729	0.36570
CV_{NS}	0.063635	4.7379	0.19200

It should be emphasized that the previous analysis was based on a sample of patients with temperature differences between $+/- 2^{\circ}C$. Therefore, to explore relationships of thermal metrics beyond this range, a further study has to be done. Nonetheless, these findings provide evidence of the potential of using these metrics as a support metric in evaluating wound evolution. By analyzing the temperature differences between different evaluation regions, wound bed, periwound, and normal skin, against Wagners's wound gradient, the study was able to provide insights of thermal metrics for wound assessment.

6.5 Discussion

Traditional wound assessment is time-consuming and subjective. Thermography and 3D models provide helpful complementary information on wound assessment and, most importantly, allow quantitative measurements to be made and documented over time to monitor wound healing.

Two-dimensional thermography can provide objective indicators on wound evaluation; however, the election of the region of interest within the wound in periwound is subjective and limited. By creating the wound segmentation on the 3D model, we can provide objective definitions of evaluation regions like wound bed, periwound, and normal skin, which contributes to the reproducibility and objectivity of geometrical and thermal metrics created from the color and thermal 3D models. Nevertheless, as the definition of evaluation regions depends on wound segmentation, which in turn depends on the 2D segmentation of color images, special attention should be focused on the model for 2D segmentation to have the most accurate 3D wound segmentation results. To improve the 2D segmentation model, a data augmentation based on the reprojection of the 3D segmentation into 2D was proposed by our team in [67]. Given the dataset collected so far, data augmentation can be performed to explore the improvements of the current 2D segmentation model.

The thermal 3D model created with our methodology enables the creation of comprehensive and affordable visualization tools, which can help clinicians and patients. Indeed, visualization of color and thermal 3D models, and their evolution over time, can increase patient knowledge and awareness of his/her condition, which in turn, can motivate better home care and clinical outcomes [64].

The clinical study presented in this chapter shows the use of thermal metrics and thermal 3D models in the clinical setup. Acquisition time is less than 5 minutes, and therefore convenient to be performed during a 30-minutes appointment. The current processing time to create 3D thermal models is, on average, 15 minutes per case. In the best scenario, the thermal 3D models could be completed before the end of the visit, which could be helpful in two ways: for the physician to review or corroborate the state of the wound in order to define a subsequent appointment, and also, it could be helpful in explaining the patient the evolution of his/her wound over time. Furthermore, the documentation of thermal 3D models over time could also allow the identification of subito changes commonly related to complications in wound evolution.

In remote areas where specialists in wound care are not available [19], creating thermal 3D models could help with teleconsultation and remote evaluation. Documentation of thermal 3D models could enable the transmission of information to a specialized clinician for analysis and treatment recommendations.

Moreover, if this is implemented in remote locations where the internet is not always available, the processing can be performed at the end of the day. For 16 patients per day, assuming one patient every 30 minutes for 8 hours, a maximum of 4 hours per day is estimated to process the 3D thermal models. Therefore, the image processing can be done overnight and be ready the next day. This challenge offers opportunities to further research on the implementation of these algorithms totally in a smartphone.

The proposed methodology can be implemented to be used at home. For this, the patient requires a low-cost dual-sensor commercial thermal camera, a marker with known size, and undergo training to acquire thermal images. Currently, image processing cannot be performed entirely on the smartphone but can be uploaded to the cloud. Cloud processing and storage are done so that thermal 3D models are available when required by the physician and the patient.

The clinical study results show that wound grading is associated with temperature differences between evaluation regions. Specifically, we have found that severe stages of chronic wounds are associated with low temperatures in the periwound compared to normal skin. Also, they are associated with low temperatures on the wound bed, compared to the periwound and normal skin. On the other hand, wounds in mild stages are associated with higher temperatures in the periwound compared to the normal skin (T_{NS-PW}). They are also associated with higher temperatures on the wound bed, compared to the periwound (T_{PW-WB}) and normal skin (T_{NS-WB}). These results are consistent with clinical analysis of wound healing.

In addition, thermal metrics have also shown a linear relationship to the healing rate by day. In particular, the temperature in the wound bed compared to the normal skin T_{NS-WB} shows that when more temperature in the wound bed is compared to the normal skin, the wound is more likely to have a higher healing rate by day.

The relationship found in the clinical is exciting as they show the potential of the thermal metrics for the evaluation of the wound status and the prognosis of wound evolution. Further research is needed as the sample size of patients followed over time is reduced, and patients have not been observed since the first day of the evaluation.

The clinical study has faced some limitations which have to be improved in the future. First, due to several confinements in Peru, data acquisition has been interrupted or limited. As a result, patients followed over time were not sampled at a regular visit interval: While some patients were collected every week, others were observed every two weeks or more. Furthermore, patients were not followed from the beginning of their treatments.

Our sample of patients was composed mostly of complex cases: 75% of the wounds had previous amputations, which makes these cases likely to heal slowly. These cases require longer-term follow-up than wounds of patients with no amputation. Therefore, extending this study to other types of patients would be valuable to confirm the findings. A larger collection of thermal 3D models would be feasible to acquire and process given the experience acquired during this clinical study and thanks to the automated pipeline for processing thermal 3D models.

Looking forward to the integration of this application in the clinical process, some considerations to be taken into account are presented, according to our experience in the realization of this clinical study:

Acquisition images should be taken at the beginning. The time is less than 5 minutes and is performed at the beginning of the session. During this time, we observed physicians speaking to patients about general symptoms and answering questions raised by the patient and relatives regarding the wound evolution.

The system we have presented does not require a specialized setup. The user in charge of the acquisition does not need to be specialized in photography but should undergo a short training period to get used to acquisition devices and protocol. Thus, the user can be a nurse, or a medical assistant used to take pictures with a smartphone.

Although the acquisition is easy, there are external conditions that must be taken into account in order for the acquisition to be successful. In our experience, the most common drawbacks that

may arise during acquisition are as follows: First, The finger may obstruct the view of the thermal camera, as the position of the thermal camera when holding the smartphone may inadvertently cover the camera with the hand or fingers. Second, thermal camera images may focus on other objects instead of the skin and wound. The user must practice capturing images with the thermal imaging camera device to receive feedback on how to move the entire smartphone in order for the camera to focus on the wound.

Ambient lighting conditions observed during acquisition must be taken into account in image acquisition. In particular, we strongly recommend the use of natural or diffused light. The wound should not be exposed to direct light, as this can reflect off on moist tissue and produce shadows. Both reflections and shadows pose problems in 3D triangulation by SfM and could reduce the quality of the 3D model.

6.6 Conclusion

The current chapter discusses the application of a system that utilizes previous work on algorithms for creating thermal 3D models from low-cost devices. The chapter details the data acquisition and implementation of an automated algorithm for processing thermal 3D models, which was applied in a clinical setting to a non-negligible sample size of 68 cases of wounds. This study surpasses previous reports on the usefulness of thermal 3D models, which are commonly limited to small sample sizes of less than five cases. This implementation demonstrates the feasibility of automating the creation of 3D thermal models, enabling clinicians to document the thermal 3D model visualization and objective metrics for better wound management.

The chapter also highlights findings of clinical interest: relationships are observed between wound grading and temperature differences in the wound bed, peri-wound, and normal skin areas. These results are consistent with clinicians' expectations of wound temperature patterns as a function of wound grading.

Chapter 7

Conclusion and perspectives

7.1 Conclusion

To go beyond the state of the art on imaging techniques proposed for the follow-up of chronic wounds, the European STANDUP project has taken the challenge of using a low cost multimodal equipment composed of a Flir one camera plugged to a Smartphone. This equipment allows a light and practical use in all care environments, including telemedicine, in rural areas with poor access and few medical staff.

To address this challenge, this thesis presents several contributions:

An analysis of the accuracy of a Flir One thermal camera for freehand acquisition

The experimentation under controlled temperature presented in Chapter 3, has allowed to highlight the importance of camera perspective, i.e. camera-object angle and distances, for improving temperature estimates. (Published in [39])

Two methods to improve temperature estimates in a multi-view context

Following the previous analysis, we have introduced two innovative methods for temperature correction in multiple thermal data contexts. The first method improves temperature estimates from a single thermal image using a state-of-the-art regression model with inverse prediction. The second method improves temperature estimation by combining data from multiple thermal views with a weighted average, giving priority to frontal and close views of the wound. These two methods have demonstrated the potential to improve the accuracy and precision of temperature estimates obtained with raw IR images. This is especially important for low-cost cameras, which typically have lower thermal accuracy.

A comprehensive review of previous works on thermal 3D model adapted for wounds and skin

We present a review of several works aimed at the creation of thermal 3D models for wounds and skin. Our review has uncovered some critical gaps. We have identified a shortage of portable and affordable thermal 3D models systems for wound assessment, which presents a significant barrier to wider adoption of thermal 3D models. Moreover, our review has highlighted the lack of clinical studies, and the reliance on small case studies to validate 3D thermal models.

A methodology for creating thermal 3D models from low-cost portable devices

Our methodology is suitable for being used with a smartphone or any other mobile device like a tablet, which can capture high resolution RGB images; coupled any dual-sensor thermal camera, like FlirOne. It goes beyond state-of-the-art approaches to create high-quality 3D thermal models, including more accurate estimates of the surface temperature of a 3D model through a multi-view fusion approach.

Unlike previous methods, our approach does not require any specialized setting for acquisition and allows for freehand acquisition, making it convenient and accessible. We showcase the efficacy of our methodology by utilizing two commercial and low-cost devices: a smartphone and a low-cost thermal camera, FlirOne Pro; and we have demonstrated its capabilities with several cases of wounds. Notably, our methodology offers the advantage of unrestricted scanning surfaces, making it particularly suitable for large wounds or those with curved surfaces

The proposed methodology can be extrapolated to create 3D thermal models of other body parts, objects or scenes. As our method is based on SfM, larger scenes can be reconstructed with sufficient overlapping images. Moreover, our algorithm allows the combination of multiple thermal views, which is useful to enlarge the scanning surface of the created thermal 3D models.

The proposed methodology was integrated into a fully automated process to create reproducible and accurate 3D thermal models. This is a key point in collecting data from images acquired in medical centers for clinical study. This process has also contributed to the growing base of labeled images for deep learning of wound segmentation [67].

Clinical study for wounds assessment and healing monitoring

An extensive collection of images of chronic wounds and thermal 3D models for diabetic patients has been done on a clinical settings. We provide a detailed clinical protocol for further replication, and provide insights for its implementation in clinical settings.

Furthermore, we have analyzed the thermal metrics produced by our thermal 3D models, and we have found evidence of its usefulness for wound evaluation and monitoring. Our results show significant relationship between thermal metrics wound staging, a clinical bio-marker of wound status.

In summary, in contrast to previous studies that proposed impractical and expensive systems, we propose a methodology to create 3D thermal models suitable for portable and low-cost devices. Furthermore, an automated process based on the proposed methodology was implemented to create 3D thermal models from 68 wound cases collected in a clinical setting. The data collection has allowed the study of thermal metrics, which have shown their potential for wound assessment and monitoring.

7.2 Perspectives

The application of our methodology has highlighted certain challenges that need to be further investigated. Although the process of acquiring images for chronic wound monitoring is generally straightforward and allows for flexibility in the number of images needed, it is important to note that larger surfaces may require a greater number of images to ensure complete coverage of the area. Further research is necessary to investigate and define better acquisition protocol according to the wound size, and curvature of the surface where the wound is located.

The accuracy of our process for creating thermal 3D models and metrics relies heavily on wound segmentation for obtaining precise geometrical and thermal metrics. Therefore, it is important to advance the wound segmentation technique, either in 2D imaging or solely on the 3D model.

Improving the background removal process is also necessary. Currently, the background removal helps to a great extent in eliminating non-useful surrounding objects; however, certain parts of

the bed are still present. To automate thermal metrics, it is essential to ensure that all non-skin surrounding objects are removed. This could be automated further using 3D model colors and changes in curvature of the surface.

Using 3D thermal models beyond chronic wounds

The methodology presented does not limit the number of different views in RGB and color images. Therefore, it is worth noting that its applicability goes beyond chronic wounds. Thermal 3D models would also be very useful for the follow-up of other pathologies such as acute wounds, burns, angiomas, and inflammations in any other body part.

However, while the thermal 3D modeling methodology is suitable for other cases beyond wounds, the automated process for creating thermal 3D models has been specially designed for dealing with cluttered and hectic clinical environment. The application to other objects or scenes might require particular automation process of the thermal 3D model creation. For example, background removal, in our case, is applied to remove any uninteresting object and for reducing computational time. The same might not be desired in other applications, like indoor scene scanning.

Computing resources

We have shown that a simple handheld acquisition can be used for creating thermal 3D models. The creation of thermal 3D models has also been automated for a simple processing of thermal 3D models for wounds. Nevertheless, despite the advantages of our automated implemented process, the algorithm creates thermal 3D models in an average of approximately 15 minutes per case, and computational resources required are not negligible. This is a current limitation, which provides opportunities for improvement in the future.

A mobile application is under development to manage image acquisition and provide visualization of the thermal 3D models. The android application could be useful for providing user instant feedback on image acquisition. This would help ensure that only suitable 2D images are used for 3D thermal modeling. Furthermore, the application's capabilities could be improved by enabling real-time reconstruction. This could be achieved by utilizing algorithms that support real-time reconstruction on smartphones such as [69]. Alternatively, ToF sensors available in smartphones nowadays could also be incorporated into the thermal 3D modeling pipeline to obtain higher resolution and more accurate 3D models.

Appendix

7.3 Other attempts to create thermal 3D models

7.3.1 SfM with thermal imaging only

In an attempt to construct a thermal 3D model using only Structure from Motion with IR images, we conducted a series of experiments on a human hand, as illustrated in Fig 7.1. However, our results revealed that thermal 3D models can be subject to noise and significant deviations from the actual object being reconstructed. More specifically, the use of solely thermal images for 3D reconstruction can lead to difficulties in distinguishing between concave and convex forms in certain cases, thereby highlighting the need for further investigation and development in this area.

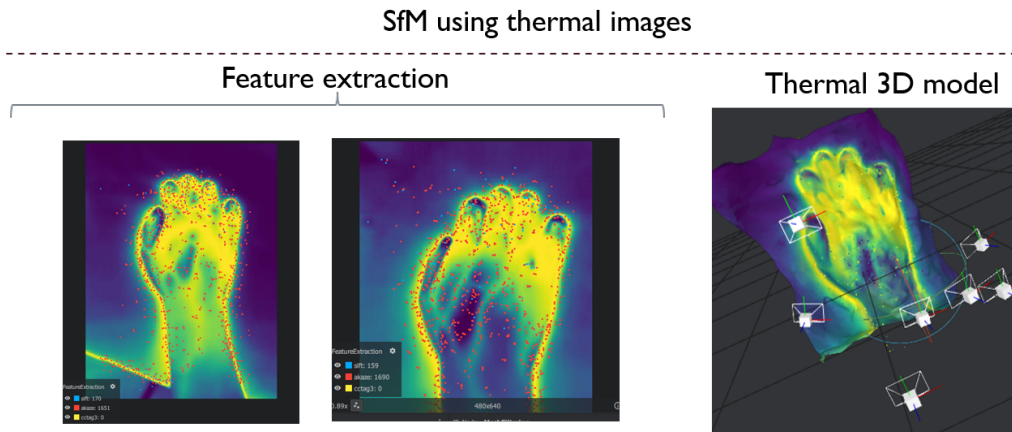


Figure 7.1: Example of SfM reconstruction using only thermal images.

7.4 Visualization Tools

7.4.1 Online HTML visualization

An innovative online visualization tool has been developed using Rmarkdown, which provides an efficient and user-friendly platform for displaying 3D thermal models. The tool presents the 3D thermal and color models in an organized and easily accessible manner while also displaying relevant statistics associated with each model. Furthermore, the web page serves as a useful platform for organizing color, thermal 3D models, and metrics, as illustrated in Figure 7.2. Fig 7.3 shows the 3D interactive visualization on the web page. A web page with the results can be found in this [link](#).

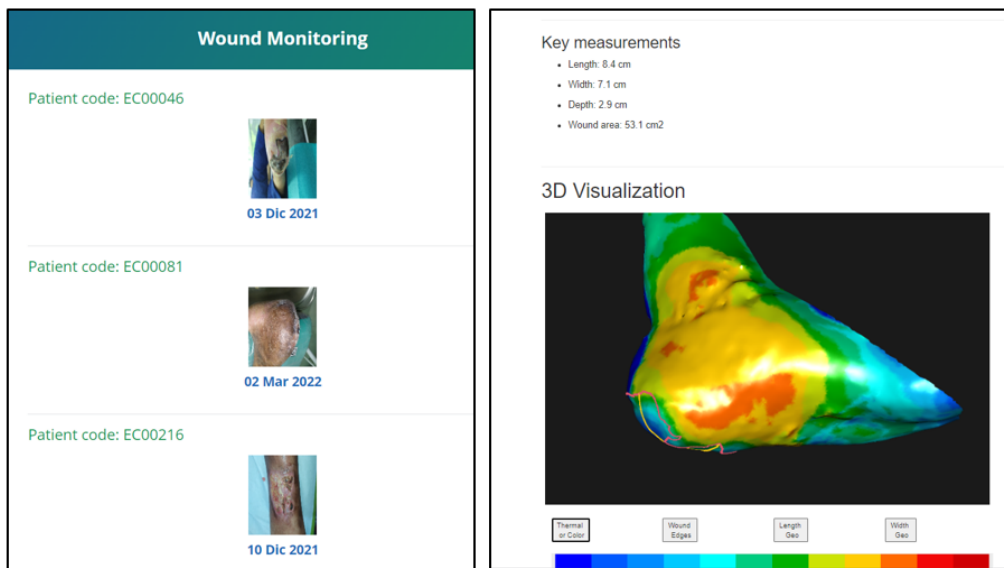


Figure 7.2: Preview of a web page created to organize and navigate through the results of thermal 3D modeling.

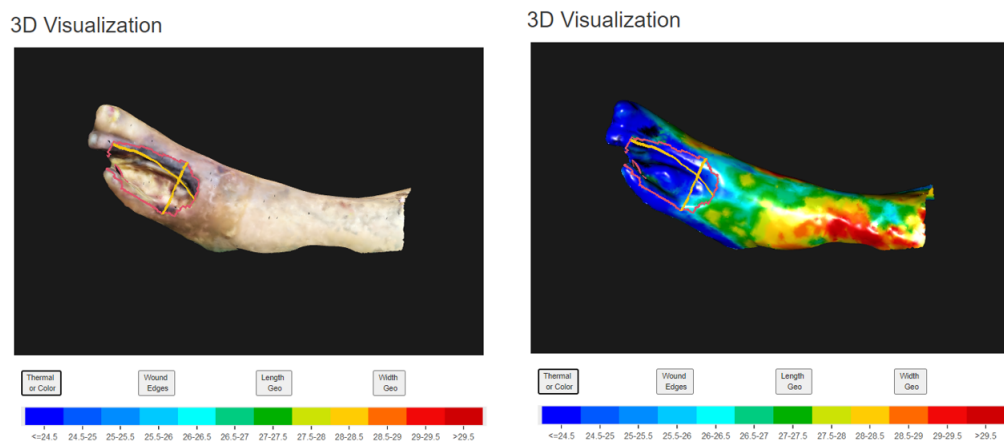


Figure 7.3: Visualization tool to observe the color and thermal 3D model on the web page.

7.4.2 Smartphone Application

An smartphone application has been developed in Android to showcase the possibilities of the proposed methodology. The application is currently under development. Preliminary views of the smartphone application are shown in 7.4

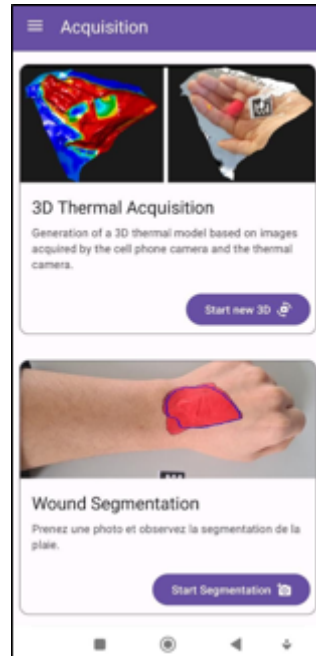


Figure 7.4: Preview of the smartphone application which provides acquisition support and visualization of results.

Related works

1. Gutierrez, E., Castañeda, B., Treuillet, S., 2020. Correction of Temperature Estimated from a Low-Cost Handheld Infrared Camera for Clinical Monitoring, in: Blanc-Talon, J., Delmas, P., Philips, W., Popescu, D., Scheunders, P. (Eds.), *Advanced Concepts for Intelligent Vision Systems*. Springer International Publishing, Cham, pp. 108–116. https://doi.org/10.1007/978-3-030-40605-9_10
2. Gutierrez, E., Castañeda, B., Treuillet, S., Lucas, Y.: Combined thermal and color 3D model for wound evaluation from handheld devices. In: Park, B.J. and Deserno, T.M. (eds.) *Medical Imaging 2021: Imaging Informatics for Healthcare, Research, and Applications*. p. 7. SPIE, Online Only, United States (2021). <https://doi.org/10.1117/12.2580669>.
3. Gutierrez, E., Castañeda, B., Treuillet, S., Hernandez, I.: Multimodal and Multi-view Wound Monitoring with Mobile Devices. *Photonics*. 8, 424 (2021). <https://doi.org/10.3390/photonics8100424>.
4. Niri, R., Gutierrez, E., Douzi, H., Lucas, Y., Treuillet, S., Castaneda, B., Hernandez, I.: Multi-View Data Augmentation to Improve Wound Segmentation on 3D Surface Model by Deep Learning. *IEEE Access*. 9, 157628–157638 (2021). <https://doi.org/10.1109/ACCESS.2021.3130784>.

Bibliography

- [1] Mohammad Faizal Ahmad Fauzi et al. “Computerized Segmentation and Measurement of Chronic Wound Images”. In: *Computers in Biology and Medicine* 60 (May 2015), pp. 74–85. ISSN: 00104825. DOI: [10.1016/j.compbiomed.2015.02.015](https://doi.org/10.1016/j.compbiomed.2015.02.015). URL: <https://linkinghub.elsevier.com/retrieve/pii/S0010482515000645> (visited on 08/28/2019).
- [2] Jarmo Alametsä et al. “Thermal Imaging in Skin Trauma Evaluation: Observations by CAT S60 Mobile Phone”. In: *Finnish Journal of eHealth and eWelfare* 10.2-3 (May 21, 2018). ISSN: 1798-0798, 1798-0798. DOI: [10.23996/fjhw.69150](https://doi.org/10.23996/fjhw.69150). URL: <https://journal.fi/finjehew/article/view/69150> (visited on 07/02/2019).
- [3] B. Albouy, Y. Lucas, and S. Treuillet. “3D Modeling from Uncalibrated Color Images for a Complete Wound Assessment Tool”. In: *2007 29th Annual International Conference of the IEEE Engineering in Medicine and Biology Society*. 2007 29th Annual International Conference of the IEEE Engineering in Medicine and Biology Society. Lyon, France: IEEE, Aug. 2007, pp. 3323–3326. ISBN: 978-1-4244-0787-3 978-1-4244-0788-0. DOI: [10.1109/IEMBS.2007.4353041](https://doi.org/10.1109/IEMBS.2007.4353041). URL: <http://ieeexplore.ieee.org/document/4353041/> (visited on 07/02/2019).
- [4] Benjamin Albouy et al. “Accurate 3D Structure Measurements from Two Uncalibrated Views”. In: *Advanced Concepts for Intelligent Vision Systems*. Ed. by Jacques Blanc-Talon et al. Red. by David Hutchison et al. Vol. 4179. Berlin, Heidelberg: Springer Berlin Heidelberg, 2006, pp. 1111–1121. ISBN: 978-3-540-44630-9 978-3-540-44632-3. DOI: [10.1007/11864349_101](https://doi.org/10.1007/11864349_101). URL: http://link.springer.com/10.1007/11864349_101 (visited on 06/01/2022).
- [5] Behzad Aliahmad et al. “Is Thermal Imaging a Useful Predictor of the Healing Status of Diabetes-Related Foot Ulcers? A Pilot Study”. In: *Journal of Diabetes Science and Technology* 13.3 (May 2019), pp. 561–567. ISSN: 1932-2968, 1932-2968. DOI: [10.1177/1932296818803115](https://doi.org/10.1177/1932296818803115). URL: <http://journals.sagepub.com/doi/10.1177/1932296818803115> (visited on 07/02/2019).
- [6] AliceVision. *Meshroom: A 3D Reconstruction Software*. 2018. URL: <https://github.com/alicevision/meshroom>.
- [7] “AliceVision Meshroom: An open-source 3D reconstruction pipeline”. In: *Proc. 12th ACM Multimed. Syst. Conf. - MMSys '21*. ACM Press, 2021. DOI: [10.1145/3458305.3478443](https://doi.org/10.1145/3458305.3478443).
- [8] *ALLIED VISION INFRARED CAMERAS, Brochure*. URL: https://www.stemmer-imaging.com/media/uploads/cameras/avt/87/87762-Allied_Vision_SWIR_and_LWIR_Camera_Brochure.pdf.
- [9] David G. Armstrong et al. “Five Year Mortality and Direct Costs of Care for People with Diabetic Foot Complications Are Comparable to Cancer”. In: *Journal of Foot and Ankle Research* 13.1 (Dec. 2020), p. 16. ISSN: 1757-1146. DOI: [10.1186/s13047-020-00383-2](https://doi.org/10.1186/s13047-020-00383-2). URL: <https://jfootankleres.biomedcentral.com/articles/10.1186/s13047-020-00383-2> (visited on 04/06/2023).
- [10] C. J. Ash, E. Gotti, and C. H. Haik. “Thermography of the Curved Living Skin Surface”. In: *Missouri Medicine* 84.11 (Nov. 1987), pp. 702–708. ISSN: 0026-6620. pmid: [3506662](https://pubmed.ncbi.nlm.nih.gov/3506662/).
- [11] Laura Banks et al. *Multi-Course Case Studies in the Health Sciences*. OE Lab at Ontario Tech University, 2021. URL: <https://ecampusontario.pressbooks.pub/casestudieshealthsciences/chapter/jacks-health-diabetic-foot-ulcers/>.

- [12] S Barone, A Paoli, and A V Razionale. “Assessment of Chronic Wounds by Three-Dimensional Optical Imaging Based on Integrating Geometrical, Chromatic, and Thermal Data”. In: *Proceedings of the Institution of Mechanical Engineers, Part H: Journal of Engineering in Medicine* 225.2 (Feb. 2011), pp. 181–193. ISSN: 0954-4119, 2041-3033. DOI: [10.1243/09544119JEIM705](https://doi.org/10.1243/09544119JEIM705). URL: <http://journals.sagepub.com/doi/10.1243/09544119JEIM705> (visited on 07/02/2019).
- [13] Rafael Bayareh-Mancilla. “Towards a Tool for Diabetic Foot Diagnosis Using a 3D Modeling Based on Thermographic and Visible Spectrum Images”.
- [14] Manish Bharara et al. “Wound Inflammatory Index: A “Proof of Concept” Study to Assess Wound Healing Trajectory”. In: *Journal of Diabetes Science and Technology* 4.4 (July 2010), pp. 773–779. ISSN: 1932-2968, 1932-2968. DOI: [10.1177/193229681000400402](https://doi.org/10.1177/193229681000400402). URL: <http://journals.sagepub.com/doi/10.1177/193229681000400402> (visited on 02/04/2023).
- [15] Rodrigo Bruno Biagioni et al. “Smartphone Application for Wound Area Measurement in Clinical Practice”. In: *Journal of Vascular Surgery Cases, Innovations and Techniques* 7.2 (June 2021), pp. 258–261. ISSN: 24684287. DOI: [10.1016/j.jvscit.2021.02.008](https://doi.org/10.1016/j.jvscit.2021.02.008). URL: <https://linkinghub.elsevier.com/retrieve/pii/S2468428721000320> (visited on 01/16/2023).
- [16] Guillaume-Alexandre Bilodeau et al. “Thermal–Visible Registration of Human Silhouettes: A Similarity Measure Performance Evaluation”. In: *Infrared Physics & Technology* 64 (May 2014), pp. 79–86. ISSN: 13504495. DOI: [10.1016/j.infrared.2014.02.005](https://doi.org/10.1016/j.infrared.2014.02.005). URL: <https://linkinghub.elsevier.com/retrieve/pii/S1350449514000334> (visited on 06/02/2022).
- [17] Andrew J. M. Boulton. “The Diabetic Foot: A Global View”. In: *Diabetes/Metabolism Research and Reviews* 16.S1 (Sept. 2000), S2–S5. ISSN: 1520-7552, 1520-7560. DOI: [10.1002/1520-7560\(200009/10\)16:1+<::AID-DMRR105>3.0.CO;2-N](https://doi.org/10.1002/1520-7560(200009/10)16:1+<::AID-DMRR105>3.0.CO;2-N). URL: [https://onlinelibrary.wiley.com/doi/10.1002/1520-7560\(200009/10\)16:1+%3C::AID-DMRR105%3E3.0.CO;2-N](https://onlinelibrary.wiley.com/doi/10.1002/1520-7560(200009/10)16:1+%3C::AID-DMRR105%3E3.0.CO;2-N) (visited on 04/06/2023).
- [18] G. Bradski. “The OpenCV Library”. In: *Dr. Dobb’s Journal of Software Tools* (2000).
- [19] F. Brundisini et al. “Chronic Disease Patients’ Experiences with Accessing Health Care in Rural and Remote Areas: A Systematic Review and Qualitative Meta-Synthesis”. In: *Ontario Health Technology Assessment Series* 13.15 (2013), pp. 1–33. ISSN: 1915-7398. pmid: [24228078](https://pubmed.ncbi.nlm.nih.gov/24228078/).
- [20] Ruth A. Bryant and Denise P. Nix, eds. *Acute & Chronic Wounds: Current Management Concepts*. Fifth edition. St. Louis, Missouri: Elsevier, 2016. ISBN: 978-0-323-31621-7.
- [21] James Stewart Campbell and M. Nathaniel Mead. *Human Medical Thermography*. 1st ed. Boca Raton: CRC Press, June 14, 2022. ISBN: 978-1-00-328176-4. DOI: [10.1201/9781003281764](https://doi.org/10.1201/9781003281764). URL: <https://www.taylorfrancis.com/books/9781003281764> (visited on 09/29/2022).
- [22] Ivo Campione et al. “3D Thermal Imaging System with Decoupled Acquisition for Industrial and Cultural Heritage Applications”. In: *Applied Sciences* 10.3 (Jan. 23, 2020), p. 828. ISSN: 2076-3417. DOI: [10.3390/app10030828](https://doi.org/10.3390/app10030828). URL: <https://www.mdpi.com/2076-3417/10/3/828> (visited on 08/17/2020).
- [23] Michelle E. Carrière et al. “Validity of Thermography for Measuring Burn Wound Healing Potential”. In: *Wound Repair and Regeneration* 28.3 (May 2020), pp. 347–354. ISSN: 1067-1927, 1524-475X. DOI: [10.1111/wrr.12786](https://doi.org/10.1111/wrr.12786). URL: <https://onlinelibrary.wiley.com/doi/10.1111/wrr.12786> (visited on 12/11/2022).
- [24] Leslie Casas, Castaneda Benjamin, and Sylvie Treuillet. “Imaging Technologies Applied to Chronic Wounds: A Survey”. In: Oct. 2011, p. 6. DOI: [10.1145/2093698.2093865](https://doi.org/10.1145/2093698.2093865).
- [25] Leslie Casas et al. “Low-Cost Uncalibrated Video-Based Tool for Tridimensional Reconstruction Oriented to Assessment of Chronic Wounds”. In: Tenth International Symposium on Medical Information Processing and Analysis. Ed. by Eduardo Romero and Natasha Lepore. Cartagena de Indias, Colombia, Jan. 28, 2015, p. 928711. DOI: [10.1117/12.2070999](https://doi.org/10.1117/12.2070999). URL: <http://proceedings.spiedigitallibrary.org/proceeding.aspx?doi=10.1117/12.2070999> (visited on 07/02/2019).

- [26] Ming-Ching Chang et al. “Multimodal Sensor System for Pressure Ulcer Wound Assessment and Care”. In: *IEEE Transactions on Industrial Informatics* 14.3 (Mar. 2018), pp. 1186–1196. ISSN: 1551-3203, 1941-0050. DOI: [10.1109/TH.2017.2782213](https://doi.org/10.1109/TH.2017.2782213). URL: <http://ieeexplore.ieee.org/document/8186246/> (visited on 08/28/2019).
- [27] Arjun Chanmugam et al. “Relative Temperature Maximum in Wound Infection and Inflammation as Compared with a Control Subject Using Long-Wave Infrared Thermography:” in: *Advances in Skin & Wound Care* 30.9 (Sept. 2017), pp. 406–414. ISSN: 1527-7941. DOI: [10.1097/01.ASW.0000522161.13573.62](https://doi.org/10.1097/01.ASW.0000522161.13573.62). URL: <http://Insights.ovid.com/crossref?an=00129334-201709000-00004> (visited on 01/15/2020).
- [28] Maria Emília Abreu Chaves et al. “Evaluation of Healing of Pressure Ulcers through Thermography: A Preliminary Study”. In: *Research on Biomedical Engineering* 31.1 (Mar. 2015), pp. 3–9. ISSN: 2446-4740. DOI: [10.1590/2446-4740.0571](https://doi.org/10.1590/2446-4740.0571). URL: http://www.scielo.br/scielo.php?script=sci_arttext&pid=S2446-47402015000100003&lng=en&tlng=en (visited on 06/05/2020).
- [29] Tze-Yuan Cheng, Daxiang Deng, and Cila Herman. “Curvature Effect Quantification for In-Vivo IR Thermography”. In: *Volume 2: Biomedical and Biotechnology*. ASME 2012 International Mechanical Engineering Congress and Exposition. Houston, Texas, USA: American Society of Mechanical Engineers, Nov. 9, 2012, pp. 127–133. ISBN: 978-0-7918-4518-9. DOI: [10.1115/IMECE2012-88105](https://doi.org/10.1115/IMECE2012-88105). URL: <https://asmedigitalcollection.asme.org/IMECE/proceedings/IMECE2012/45189/127/260549> (visited on 01/17/2020).
- [30] S. Colantonio et al. “A Method to Integrate Thermographic Data and 3D Shapes for Diabetic Foot Disease”. In: *Proceedings of the 2006 International Conference on Quantitative InfraRed Thermography*. 2006 Quantitative InfraRed Thermography. QIRT Council, 2006. DOI: [10.21611/qirt.2006.073](https://doi.org/10.21611/qirt.2006.073). URL: <http://qirt.org/archives/qirt2006/papers/073.pdf> (visited on 07/02/2019).
- [31] Evan S Darwin et al. “Comparison of 3-Dimensional Wound Measurement With Laser-assisted and Hand Measurements: A Retrospective Chart Review”. In: *Wound Management & Prevention* 65.1 (Jan. 15, 2019), pp. 36–41. ISSN: 26405237, 26405245. DOI: [10.25270/wmp.2019.1.3641](https://doi.org/10.25270/wmp.2019.1.3641). URL: <https://www.o-wm.com/article/comparison-3-dimensional-wound-measurement-laser-assisted-and-hand-measurements> (visited on 07/02/2019).
- [32] Valentina Dini et al. “Correlation Between Wound Temperature Obtained With an Infrared Camera and Clinical Wound Bed Score in Venous Leg Ulcers”. In: *Wounds: A Compendium of Clinical Research and Practice* 27.10 (Oct. 2015), pp. 274–278. ISSN: 1943-2704. pmid: [26479211](https://pubmed.ncbi.nlm.nih.gov/26479211/).
- [33] Caroline Dowsett and Martin Nyløkke. “Taking Wound Assessment beyond the Edge”. In: *Clinical practice* 6.1 (2015).
- [34] *Eykona 3D Wound Imaging*. Eykona (Fuel 3D, Los Angeles). URL: <https://www.qt.io/eykona-built-with-qt>.
- [35] Marjorie Fierheller and R. Gary Sibbald. “A Clinical Investigation into the Relationship between Increased Periwound Skin Temperature and Local Wound Infection in Patients with Chronic Leg Ulcers”. In: *Advances in Skin & Wound Care* 23.8 (Aug. 2010), pp. 369–379. ISSN: 1527-7941. DOI: [10.1097/01.ASW.0000383197.28192.98](https://doi.org/10.1097/01.ASW.0000383197.28192.98). URL: <https://journals.lww.com/00129334-201008000-00008> (visited on 06/24/2021).
- [36] Damir Filko, Robert Cupec, and Emmanuel Karlo Nyarko. “Wound Measurement by RGB-D Camera”. In: *Machine Vision and Applications* 29.4 (May 2018), pp. 633–654. ISSN: 0932-8092, 1432-1769. DOI: [10.1007/s00138-018-0920-4](https://doi.org/10.1007/s00138-018-0920-4). URL: <http://link.springer.com/10.1007/s00138-018-0920-4> (visited on 06/14/2021).
- [37] S. Garrido-Jurado et al. “Automatic Generation and Detection of Highly Reliable Fiducial Markers under Occlusion”. In: *Pattern Recognition* 47.6 (June 2014), pp. 2280–2292. ISSN: 00313203. DOI: [10.1016/j.patcog.2014.01.005](https://doi.org/10.1016/j.patcog.2014.01.005). URL: <https://linkinghub.elsevier.com/retrieve/pii/S0031320314000235> (visited on 01/25/2023).

- [38] Sara González-Pérez et al. “Assessment of Registration Methods for Thermal Infrared and Visible Images for Diabetic Foot Monitoring”. In: *Sensors* 21.7 (Mar. 24, 2021), p. 2264. ISSN: 1424-8220. DOI: [10.3390/s21072264](https://doi.org/10.3390/s21072264). URL: <https://www.mdpi.com/1424-8220/21/7/2264> (visited on 06/02/2022).
- [39] Evelyn Gutierrez, Benjamin Castañeda, and Sylvie Treuillet. “Correction of Temperature Estimated from a Low-Cost Handheld Infrared Camera for Clinical Monitoring”. In: *Advanced Concepts for Intelligent Vision Systems*. Ed. by Jacques Blanc-Talon et al. Vol. 12002. Cham: Springer International Publishing, 2020, pp. 108–116. ISBN: 978-3-030-40604-2 978-3-030-40605-9. DOI: [10.1007/978-3-030-40605-9_10](https://doi.org/10.1007/978-3-030-40605-9_10). URL: http://link.springer.com/10.1007/978-3-030-40605-9_10 (visited on 12/22/2020).
- [40] Richard Hartley and Andrew Zisserman. *Multiple View Geometry in Computer Vision*. 2nd ed. Cambridge, UK ; New York: Cambridge University Press, 2003. 655 pp. ISBN: 978-0-521-54051-3.
- [41] Constantijn E.V.B. Hazenberg et al. “Assessment of Signs of Foot Infection in Diabetes Patients Using Photographic Foot Imaging and Infrared Thermography”. In: *Diabetes Technology & Therapeutics* 16.6 (June 2014), pp. 370–377. ISSN: 1520-9156, 1557-8593. DOI: [10.1089/dia.2013.0251](https://doi.org/10.1089/dia.2013.0251). URL: <http://www.liebertpub.com/doi/10.1089/dia.2013.0251> (visited on 07/02/2019).
- [42] *Herschel Experiment*. Herschel Experiment, Gizmoz. URL: <https://gizmos.explorelarning.com/index.cfm?method=cResource.dspView&ResourceID=389>.
- [43] Tomislav Hrkać, Zoran Kalafatić, and Josip Krapac. “Infrared-Visual Image Registration Based on Corners and Hausdorff Distance”. In: *Image Analysis*. Ed. by Bjarne Kjær Ersbøll and Kim Steenstrup Pedersen. Vol. 4522. Berlin, Heidelberg: Springer Berlin Heidelberg, 2007, pp. 383–392. ISBN: 978-3-540-73039-2 978-3-540-73040-8. DOI: [10.1007/978-3-540-73040-8_39](https://doi.org/10.1007/978-3-540-73040-8_39). URL: http://link.springer.com/10.1007/978-3-540-73040-8_39 (visited on 06/01/2022).
- [44] *InSight (eKare, Inc., Fairfax, VA)*. URL: <https://ekare.ai/advanced-wound-imaging/>.
- [45] Kanakamani Jeyaraman et al. “Mortality in Patients with Diabetic Foot Ulcer: A Retrospective Study of 513 Cases from a Single Centre in the Northern Territory of Australia”. In: *BMC Endocrine Disorders* 19.1 (Dec. 2019), p. 1. ISSN: 1472-6823. DOI: [10.1186/s12902-018-0327-2](https://doi.org/10.1186/s12902-018-0327-2). URL: <https://bmcendocrdisord.biomedcentral.com/articles/10.1186/s12902-018-0327-2> (visited on 04/06/2023).
- [46] Xingyu Jiang et al. “A Review of Multimodal Image Matching: Methods and Applications”. In: *Information Fusion* 73 (Sept. 2021), pp. 22–71. ISSN: 15662535. DOI: [10.1016/j.inffus.2021.02.012](https://doi.org/10.1016/j.inffus.2021.02.012). URL: <https://linkinghub.elsevier.com/retrieve/pii/S156625352100035X> (visited on 06/01/2022).
- [47] Line Bisgaard Jørgensen et al. “Monitoring Wound Healing of Diabetic Foot Ulcers Using Two-Dimensional and Three-Dimensional Wound Measurement Techniques: A Prospective Cohort Study”. In: *Advances in Wound Care* 9.10 (Oct. 1, 2020), pp. 553–563. ISSN: 2162-1918, 2162-1934. DOI: [10.1089/wound.2019.1000](https://doi.org/10.1089/wound.2019.1000). URL: <https://www.liebertpub.com/doi/10.1089/wound.2019.1000> (visited on 02/16/2021).
- [48] Line Bisgaard Jørgensen et al. “Validation of Three-dimensional Wound Measurements Using a Novel 3D-WAM Camera”. In: *Wound Repair and Regeneration* 26.6 (Nov. 2018), pp. 456–462. ISSN: 1067-1927, 1524-475X. DOI: [10.1111/wrr.12664](https://doi.org/10.1111/wrr.12664). URL: <https://onlinelibrary.wiley.com/doi/abs/10.1111/wrr.12664> (visited on 06/16/2021).
- [49] Xiangyang Ju, Jean-Christophe Nebel, and J. Paul Siebert. “3D Thermography Imaging Standardization Technique for Inflammation Diagnosis”. In: *Photonics Asia 2004*. Ed. by Haimei Gong, Yi Cai, and Jean-Pierre Chatard. Beijing, China, Jan. 10, 2005, p. 266. DOI: [10.1117/12.577055](https://doi.org/10.1117/12.577055). URL: <http://proceedings.spiedigitallibrary.org/proceeding.aspx?doi=10.1117/12.577055> (visited on 07/02/2019).

- [50] Ellen Keenan et al. “Enhanced Thermal Imaging of Wound Tissue for Better Clinical Decision Making”. In: *Physiological Measurement* 38.6 (June 1, 2017), pp. 1104–1115. ISSN: 0967-3334, 1361-6579. DOI: [10.1088/1361-6579/aa6ea0](https://doi.org/10.1088/1361-6579/aa6ea0). URL: <https://iopscience.iop.org/article/10.1088/1361-6579/aa6ea0> (visited on 07/22/2021).
- [51] Michał Kręćichwost et al. “Chronic Wounds Multimodal Image Database”. In: *Computerized Medical Imaging and Graphics* 88 (Mar. 2021), p. 101844. ISSN: 08956111. DOI: [10.1016/j.compmedimag.2020.101844](https://doi.org/10.1016/j.compmedimag.2020.101844). URL: <https://linkinghub.elsevier.com/retrieve/pii/S0895611120301397> (visited on 05/03/2022).
- [52] Andriy Guilherme Krefer et al. “A Method for Generating 3D Thermal Models with Decoupled Acquisition”. In: *Computer Methods and Programs in Biomedicine* 151 (Nov. 2017), pp. 79–90. ISSN: 01692607. DOI: [10.1016/j.cmpb.2017.08.009](https://doi.org/10.1016/j.cmpb.2017.08.009). URL: <https://linkinghub.elsevier.com/retrieve/pii/S0169260716314195> (visited on 02/23/2021).
- [53] Martin Landmann et al. “High-Speed 3D Thermography”. In: *Optics and Lasers in Engineering* 121 (Oct. 2019), pp. 448–455. ISSN: 01438166. DOI: [10.1016/j.optlaseng.2019.05.009](https://doi.org/10.1016/j.optlaseng.2019.05.009). URL: <https://linkinghub.elsevier.com/retrieve/pii/S0143816618317895> (visited on 10/19/2021).
- [54] Joel Willem Johan Lasschuit, Jill Featherston, and Katherine Thuy Trang Tonks. “Reliability of a Three-Dimensional Wound Camera and Correlation With Routine Ruler Measurement in Diabetes-Related Foot Ulceration”. In: *Journal of Diabetes Science and Technology* 15.6 (Nov. 2021), pp. 1361–1367. ISSN: 1932-2968, 1932-2968. DOI: [10.1177/1932296820974654](https://doi.org/10.1177/1932296820974654). URL: <http://journals.sagepub.com/doi/10.1177/1932296820974654> (visited on 11/14/2022).
- [55] Bruno Lévy et al. “Least Squares Conformal Maps for Automatic Texture Atlas Generation”. In: *ACM Transactions on Graphics* 21.3 (July 2002), pp. 362–371. ISSN: 0730-0301, 1557-7368. DOI: [10.1145/566654.5666590](https://doi.org/10.1145/566654.5666590). URL: <https://dl.acm.org/doi/10.1145/566654.5666590> (visited on 01/04/2023).
- [56] David W. Lewis, Herbert O. Goller, and Charles D. Teates. “Apparent Temperature Degradation in Thermograms of Human Anatomy Viewed Obliquely”. In: *Radiology* 106.1 (Jan. 1973), pp. 95–99. ISSN: 0033-8419, 1527-1315. DOI: [10.1148/106.1.95](https://doi.org/10.1148/106.1.95). URL: <http://pubs.rsna.org/doi/10.1148/106.1.95> (visited on 07/03/2019).
- [57] *LifeViz 3D System (Quantificare S.A., Valbonne, France)*. URL: <https://www.quantificare.com/3d-photography-systems/lifviz-pro/>.
- [58] Minta Lu et al. “Enhance Wound Healing Monitoring through a Thermal Imaging Based Smartphone App”. In: *Medical Imaging 2018: Imaging Informatics for Healthcare, Research, and Applications*. Imaging Informatics for Healthcare, Research, and Applications. Ed. by Jianguo Zhang and Po-Hao Chen. Houston, United States: SPIE, Mar. 6, 2018, p. 60. ISBN: 978-1-5106-1647-9 978-1-5106-1648-6. DOI: [10.1117/12.2293674](https://doi.org/10.1117/12.2293674). URL: <https://www.spiedigitallibrary.org/conference-proceedings-of-spie/10579/2293674/Enhance-wound-healing-monitoring-through-a-thermal-imaging-based-smartphone/10.1117/12.2293674.full> (visited on 12/01/2022).
- [59] Fellipe M. C. Barbosa, Bruno M. Carvalho, and Rafael B. Gomes. “Accurate Chronic Wound Area Measurement Using Structure from Motion”. In: *2020 IEEE 33rd International Symposium on Computer-Based Medical Systems (CBMS)*. 2020 IEEE 33rd International Symposium on Computer-Based Medical Systems (CBMS). Rochester, MN, USA: IEEE, July 2020, pp. 208–213. ISBN: 978-1-72819-429-5. DOI: [10.1109/CBMS49503.2020.00047](https://doi.org/10.1109/CBMS49503.2020.00047). URL: <https://ieeexplore.ieee.org/document/9183195/> (visited on 06/02/2022).
- [60] Virginia Mamone et al. “Monitoring Wound Healing with Contactless Measurements and Augmented Reality”. In: *IEEE Journal of Translational Engineering in Health and Medicine* (2020), pp. 1–1. ISSN: 2168-2372. DOI: [10.1109/JTEHM.2020.2983156](https://doi.org/10.1109/JTEHM.2020.2983156). URL: <https://ieeexplore.ieee.org/document/9050807/> (visited on 04/06/2020).
- [61] Waldemar Minkina and Sebastian Dudzik. “Infrared Thermography: Errors and Uncertainties”. In: (), p. 222.

- [62] Carlo Mirabella et al. “Hemodynamic 3D Infrared Thermal Stereoscopic Imaging (TSI) Investigation in Chronic Vascular Leg Ulcers: A Feasibility Study”. In: *Wounds: A Compendium of Clinical Research and Practice* 23.9 (Sept. 2011), pp. 276–284. ISSN: 1044-7946. pmid: [25879268](#).
- [63] Peyman Moghadam. “3D Medical Thermography Device”. In: *SPIE Sensing Technology + Applications*. Ed. by Sheng-Jen (Tony) Hsieh and Joseph N. Zalameda. Baltimore, Maryland, United States, May 12, 2015, 94851J. DOI: [10.1117/12.2177880](#). URL: <http://proceedings.spiedigitallibrary.org/proceeding.aspx?doi=10.1117/12.2177880> (visited on 06/23/2020).
- [64] Ingrid Mühlhauser and Matthias Lenz. “Verbesserung der Therapieergebnisse durch Patientenwissen?” In: *Zeitschrift für Evidenz, Fortbildung und Qualität im Gesundheitswesen* 102.4 (July 2008), pp. 223–230. ISSN: 18659217. DOI: [10.1016/j.zefq.2008.04.002](#). URL: <https://linkinghub.elsevier.com/retrieve/pii/S1865921708001098> (visited on 01/09/2023).
- [65] G. Nakagami et al. “Predicting Delayed Pressure Ulcer Healing Using Thermography: A Prospective Cohort Study”. In: *Journal of Wound Care* 19.11 (Nov. 2010), pp. 465–472. ISSN: 0969-0700, 2052-2916. DOI: [10.12968/jowc.2010.19.11.79695](#). URL: <http://www.magonlinelibrary.com/doi/10.12968/jowc.2010.19.11.79695> (visited on 05/05/2020).
- [66] R. Niri et al. “Multi-View Data Augmentation to Improve Wound Segmentation on 3D Surface Model by Deep Learning”. In: *IEEE Access* 9 (2021), pp. 157628–157638. ISSN: 2169-3536. DOI: [10.1109/ACCESS.2021.3130784](#). URL: <https://ieeexplore.ieee.org/document/9627142/> (visited on 08/09/2022).
- [67] R. Niri et al. “Multi-View Data Augmentation to Improve Wound Segmentation on 3D Surface Model by Deep Learning”. In: *IEEE Access* 9 (2021), pp. 157628–157638. ISSN: 2169-3536. DOI: [10.1109/ACCESS.2021.3130784](#). URL: <https://ieeexplore.ieee.org/document/9627142/> (visited on 01/15/2022).
- [68] Robert Nunan, Keith G. Harding, and Paul Martin. “Clinical Challenges of Chronic Wounds: Searching for an Optimal Animal Model to Recapitulate Their Complexity”. In: *Disease Models & Mechanisms* 7.11 (Nov. 1, 2014), pp. 1205–1213. ISSN: 1754-8411, 1754-8403. DOI: [10.1242/dmm.016782](#). URL: <https://journals.biologists.com/dmm/article/7/11/1205/19939/Clinical-challenges-of-chronic-wounds-searching> (visited on 01/16/2023).
- [69] Peter Ondruska, Pushmeet Kohli, and Shahram Izadi. “MobileFusion: Real-Time Volumetric Surface Reconstruction and Dense Tracking on Mobile Phones”. In: *IEEE Transactions on Visualization and Computer Graphics* 21.11 (Nov. 15, 2015), pp. 1251–1258. ISSN: 1077-2626, 1941-0506, 2160-9306. DOI: [10.1109/TVCG.2015.2459902](#). URL: <https://ieeexplore.ieee.org/document/7165662/> (visited on 07/02/2019).
- [70] “OpenGL 4.6 (Core Profile) - May 5, 2022”. In: ().
- [71] Antonio Ordonez Muller and Andreas Kroll. “Generating High Fidelity 3-D Thermograms With a Handheld Real-Time Thermal Imaging System”. In: *IEEE Sensors Journal* 17.3 (Feb. 1, 2017), pp. 774–783. ISSN: 1530-437X, 1558-1748, 2379-9153. DOI: [10.1109/JSEN.2016.2621166](#). URL: <http://ieeexplore.ieee.org/document/7676356/> (visited on 07/05/2021).
- [72] Daryoush Parvizi et al. “BurnCase 3D Software Validation Study: Burn Size Measurement Accuracy and Inter-Rater Reliability”. In: *Burns* 42.2 (Mar. 2016), pp. 329–335. ISSN: 03054179. DOI: [10.1016/j.burns.2016.01.008](#). URL: <https://linkinghub.elsevier.com/retrieve/pii/S0305417916000115> (visited on 05/31/2022).
- [73] Dereck W. Paul et al. “Noninvasive Imaging Technologies for Cutaneous Wound Assessment: A Review: Noninvasive Optical Imaging Technologies”. In: *Wound Repair and Regeneration* 23.2 (Mar. 2015), pp. 149–162. ISSN: 10671927. DOI: [10.1111/wrr.12262](#). URL: <https://onlinelibrary.wiley.com/doi/10.1111/wrr.12262> (visited on 06/02/2022).
- [74] U. Pavlovčič and M. Jezeršek. “Handheld 3-Dimensional Wound Measuring System”. In: *Skin Research and Technology* 24.2 (May 2018), pp. 326–333. ISSN: 0909752X. DOI: [10.1111/srt.12434](#). URL: <https://onlinelibrary.wiley.com/doi/10.1111/srt.12434> (visited on 02/05/2023).

- [75] J. Posnett et al. “The Resource Impact of Wounds on Health-Care Providers in Europe”. In: *Journal of Wound Care* 18.4 (Apr. 2009), pp. 154–154. ISSN: 0969-0700, 2052-2916. DOI: [10.12968/jowc.2009.18.4.41607](https://doi.org/10.12968/jowc.2009.18.4.41607). URL: <http://www.magonlinelibrary.com/doi/10.12968/jowc.2009.18.4.41607> (visited on 02/27/2023).
- [76] Niri Rania et al. “Semantic Segmentation of Diabetic Foot Ulcer Images: Dealing with Small Dataset in DL Approaches”. In: *Image and Signal Processing*. Ed. by Abderrahim El Moataz et al. Cham: Springer International Publishing, 2020, pp. 162–169. ISBN: 978-3-030-51935-3.
- [77] Marco Romanelli et al. “Wound Assessment by 3-Dimensional Laser Scanning”. In: *Archives of Dermatology* 143.10 (Oct. 1, 2007). ISSN: 0003-987X. DOI: [10.1001/archderm.143.10.1333](https://doi.org/10.1001/archderm.143.10.1333). URL: <http://archderm.jamanetwork.com/article.aspx?doi=10.1001/archderm.143.10.1333> (visited on 02/26/2023).
- [78] Roope Lasanen. “Infrared Thermography in the Evaluation of Skin Temperature: Applications in Musculoskeletal Conditions”. Department of Applied Physics, University of Eastern Finland, Oct. 9, 2015.
- [79] E. Saiti and T. Theoharis. “An Application Independent Review of Multimodal 3D Registration Methods”. In: *Computers & Graphics* 91 (Oct. 2020), pp. 153–178. ISSN: 00978493. DOI: [10.1016/j.cag.2020.07.012](https://doi.org/10.1016/j.cag.2020.07.012). URL: <https://linkinghub.elsevier.com/retrieve/pii/S009784932030114X> (visited on 08/31/2020).
- [80] David Sánchez-Jiménez et al. “SFM-3DULC : Reliability of a New 3D Wound Measurement Procedure and Its Accuracy in Projected Area”. In: *International Wound Journal* 19.1 (Jan. 2022), pp. 44–51. ISSN: 1742-4801, 1742-481X. DOI: [10.1111/iwj.13595](https://doi.org/10.1111/iwj.13595). URL: <https://onlinelibrary.wiley.com/doi/10.1111/iwj.13595> (visited on 11/15/2022).
- [81] S. Schramm et al. “Generation of Large-Scale 3D Thermograms in Real-Time Using Depth and Infrared Cameras”. In: *Proceedings of the 2020 International Conference on Quantitative InfraRed Thermography*. 2020 Quantitative InfraRed Thermography. QIRT Council, 2020. DOI: [10.21611/qirt.2020.008](https://doi.org/10.21611/qirt.2020.008). URL: <http://qirt.org/archives/qirt2020/papers/008.pdf> (visited on 03/02/2021).
- [82] Dr Gheorghe Serbu. “Infrared Imaging of the Diabetic Foot”. In: (2009), p. 8.
- [83] Aj Shah, C. Wollak, and J.B. Shah. “Wound Measurement Techniques: Comparing the Use of Ruler Method, 2D Imaging and 3D Scanner”. In: *Journal of the American College of Clinical Wound Specialists* 5.3 (Dec. 2013), pp. 52–57. ISSN: 22135103. DOI: [10.1016/j.jccw.2015.02.001](https://doi.org/10.1016/j.jccw.2015.02.001). URL: <https://linkinghub.elsevier.com/retrieve/pii/S2213510315000111> (visited on 06/16/2021).
- [84] Awatif Shamata and Tim Thompson. “Determining the Effectiveness of Noncontact Three-Dimensional Surface Scanning for the Assessment of Open Injuries”. In: *Journal of Forensic Sciences* 65.2 (Mar. 2020), pp. 627–635. ISSN: 0022-1198, 1556-4029. DOI: [10.1111/1556-4029.14205](https://doi.org/10.1111/1556-4029.14205). URL: <https://onlinelibrary.wiley.com/doi/10.1111/1556-4029.14205> (visited on 02/05/2023).
- [85] Awatif Shamata and Tim Thompson. “Documentation and Analysis of Traumatic Injuries in Clinical Forensic Medicine Involving Structured Light Three-Dimensional Surface Scanning versus Photography”. In: *Journal of Forensic and Legal Medicine* 58 (Aug. 2018), pp. 93–100. ISSN: 1752928X. DOI: [10.1016/j.jflm.2018.05.004](https://doi.org/10.1016/j.jflm.2018.05.004). URL: <https://linkinghub.elsevier.com/retrieve/pii/S1752928X18302737> (visited on 12/30/2022).
- [86] *Silhouette Camera (Aranz, Christchurch, New Zealand)*. URL: <https://www.aranzmedical.com/>.
- [87] *STANDUP Project*. home page. URL: <https://www.standupproject.eu/>.
- [88] K.A. Stockton et al. “3D Photography Is as Accurate as Digital Planimetry Tracing in Determining Burn Wound Area”. In: *Burns* 41.1 (Feb. 2015), pp. 80–84. ISSN: 03054179. DOI: [10.1016/j.burns.2014.04.022](https://doi.org/10.1016/j.burns.2014.04.022). URL: <https://linkinghub.elsevier.com/retrieve/pii/S0305417914001636> (visited on 06/01/2022).
- [89] *Structure Sensor*. URL: <https://structure.io/>.

- [90] Richard Szeliski. *Computer Vision*. Texts in Computer Science. London: Springer London, 2011. ISBN: 978-1-84882-934-3 978-1-84882-935-0. DOI: [10.1007/978-1-84882-935-0](https://doi.org/10.1007/978-1-84882-935-0). URL: <http://link.springer.com/10.1007/978-1-84882-935-0> (visited on 02/13/2022).
- [91] S. Treuillet, B. Albouy, and Y. Lucas. “Three-Dimensional Assessment of Skin Wounds Using a Standard Digital Camera”. In: *IEEE Transactions on Medical Imaging* 28.5 (May 2009), pp. 752–762. ISSN: 0278-0062, 1558-254X. DOI: [10.1109/TMI.2008.2012025](https://doi.org/10.1109/TMI.2008.2012025). URL: <http://ieeexplore.ieee.org/document/4749314/> (visited on 07/02/2019).
- [92] Trong Phuc Truong et al. “Registration of RGB and Thermal Point Clouds Generated by Structure From Motion”. In: *2017 IEEE International Conference on Computer Vision Workshops (ICCVW)*. 2017 IEEE International Conference on Computer Vision Workshop (ICCVW). Venice: IEEE, Oct. 2017, pp. 419–427. ISBN: 978-1-5386-1034-3. DOI: [10.1109/ICCVW.2017.57](https://doi.org/10.1109/ICCVW.2017.57). URL: <http://ieeexplore.ieee.org/document/8265267/> (visited on 07/02/2019).
- [93] Rob F. M. van Doremalen et al. “Infrared 3D Thermography for Inflammation Detection in Diabetic Foot Disease: A Proof of Concept”. In: *Journal of Diabetes Science and Technology* 14.1 (Jan. 2020), pp. 46–54. ISSN: 1932-2968, 1932-2968. DOI: [10.1177/1932296819854062](https://doi.org/10.1177/1932296819854062). URL: <http://journals.sagepub.com/doi/10.1177/1932296819854062> (visited on 09/03/2020).
- [94] Ricardo Vardasca and Ricardo Simoes. “Current Issues in Medical Thermography”. In: *Topics in Medical Image Processing and Computational Vision*. Ed. by João Manuel R.S. Tavares and Renato M. Natal Jorge. Vol. 8. Dordrecht: Springer Netherlands, 2013, pp. 223–237. ISBN: 978-94-007-0725-2 978-94-007-0726-9. DOI: [10.1007/978-94-007-0726-9_12](https://doi.org/10.1007/978-94-007-0726-9_12). URL: http://link.springer.com/10.1007/978-94-007-0726-9_12 (visited on 12/21/2022).
- [95] Stephen Vidas and Peyman Moghadam. “HeatWave: A Handheld 3D Thermography System for Energy Auditing”. In: *Energy and Buildings* 66 (Nov. 2013), pp. 445–460. ISSN: 03787788. DOI: [10.1016/j.enbuild.2013.07.030](https://doi.org/10.1016/j.enbuild.2013.07.030). URL: <https://linkinghub.elsevier.com/retrieve/pii/S0378778813004180> (visited on 08/17/2020).
- [96] Stephen Vidas, Peyman Moghadam, and Sridha Sridharan. “Real-Time Mobile 3D Temperature Mapping”. In: *IEEE Sensors Journal* 15.2 (Feb. 2015), pp. 1145–1152. ISSN: 1530-437X, 1558-1748, 2379-9153. DOI: [10.1109/JSEN.2014.2360709](https://doi.org/10.1109/JSEN.2014.2360709). URL: <http://ieeexplore.ieee.org/document/6912941/> (visited on 03/02/2021).
- [97] F. William Wagner. “The Dysvascular Foot: A System for Diagnosis and Treatment”. In: *Foot & Ankle* 2.2 (Sept. 1981), pp. 64–122. ISSN: 0198-0211. DOI: [10.1177/107110078100200202](https://doi.org/10.1177/107110078100200202). URL: <http://journals.sagepub.com/doi/10.1177/107110078100200202> (visited on 01/05/2023).
- [98] H Wannous, Y Lucas, and S Treuillet. “Enhanced Assessment of the Wound-Healing Process by Accurate Multiview Tissue Classification”. In: *IEEE Transactions on Medical Imaging* 30.2 (Feb. 2011), pp. 315–326. ISSN: 0278-0062, 1558-254X. DOI: [10.1109/TMI.2010.2077739](https://doi.org/10.1109/TMI.2010.2077739). URL: <http://ieeexplore.ieee.org/document/5582291/> (visited on 07/02/2019).
- [99] H. Wannous et al. “A Complete 3D Wound Assessment Tool for Accurate Tissue Classification and Measurement”. In: *2008 15th IEEE International Conference on Image Processing*. 2008 15th IEEE International Conference on Image Processing - ICIP 2008. San Diego, CA: IEEE, Oct. 2008, pp. 2928–2931. ISBN: 978-1-4244-1765-0. DOI: [10.1109/ICIP.2008.4712408](https://doi.org/10.1109/ICIP.2008.4712408). URL: <http://ieeexplore.ieee.org/document/4712408/> (visited on 02/16/2021).
- [100] *WoundVision*. URL: <https://woundvision.com/wound-solutions/>.
- [101] Baobei Xu et al. “On-the-Fly Extrinsic Calibration of Multimodal Sensing System for Fast 3D Thermographic Scanning”. In: *Applied Optics* 58.12 (Apr. 20, 2019), p. 3238. ISSN: 1559-128X, 2155-3165. DOI: [10.1364/AO.58.003238](https://doi.org/10.1364/AO.58.003238). URL: <https://www.osapublishing.org/abstract.cfm?URI=ao-58-12-3238> (visited on 03/02/2021).
- [102] Erica Y. Xue et al. “Use of FLIR ONE Smartphone Thermography in Burn Wound Assessment.” in: *Annals of Plastic Surgery* (Feb. 2018), p. 1. ISSN: 0148-7043. DOI: [10.1097/SAP.0000000000001363](https://doi.org/10.1097/SAP.0000000000001363). URL: <http://Insights.ovid.com/crossref?an=00000637-90000000-97458> (visited on 01/16/2020).

- [103] Manoj Kumar Yadav et al. “Segmentation of Chronic Wound Areas by Clustering Techniques Using Selected Color Space”. In: *Journal of Medical Imaging and Health Informatics* 3.1 (Mar. 1, 2013), pp. 22–29. ISSN: 2156-7018. DOI: [10.1166/jmihi.2013.1124](https://doi.org/10.1166/jmihi.2013.1124). URL: <http://www.ingentaconnect.com/content/10.1166/jmihi.2013.1124> (visited on 07/02/2019).
- [104] Ming-Der Yang, Tung-Ching Su, and Hung-Yu Lin. “2 Fusion of Infrared Thermal Image and Visible Image 3 for 3D Thermal Model Reconstruction Using 4 Smartphone Sensors”. In: (2018), p. 16.
- [105] Ming-Der Yang, Tung-Ching Su, and Hung-Yu Lin. “Fusion of Infrared Thermal Image and Visible Image for 3D Thermal Model Reconstruction Using Smartphone Sensors”. In: *Sensors* 18.7 (June 22, 2018), p. 2003. ISSN: 1424-8220. DOI: [10.3390/s18072003](https://doi.org/10.3390/s18072003). URL: <http://www.mdpi.com/1424-8220/18/7/2003> (visited on 07/02/2019).
- [106] Adam Yee, John Harmon, and Steven Yi. “Quantitative Monitoring Wound Healing Status Through Three-dimensional Imaging on Mobile Platforms”. In: *Journal of the American College of Clinical Wound Specialists* 8.1-3 (2016), pp. 21–27. ISSN: 22135103. DOI: [10.1016/j.jccw.2017.11.001](https://doi.org/10.1016/j.jccw.2017.11.001). URL: <https://linkinghub.elsevier.com/retrieve/pii/S2213510317300076> (visited on 07/08/2019).
- [107] Omar Zenteno et al. “Volumetric Monitoring of Cutaneous Leishmaniasis Ulcers: Can Camera Be as Accurate as Laser Scanner?” In: *Computer Methods in Biomechanics and Biomedical Engineering: Imaging & Visualization* 7.5-6 (Nov. 2, 2019), pp. 667–675. ISSN: 2168-1163, 2168-1171. DOI: [10.1080/21681163.2018.1546623](https://doi.org/10.1080/21681163.2018.1546623). URL: <https://www.tandfonline.com/doi/full/10.1080/21681163.2018.1546623> (visited on 08/24/2021).
- [108] F. Zvietcovich et al. “A 3D Assessment Tool for Accurate Volume Measurement for Monitoring the Evolution of Cutaneous Leishmaniasis Wounds”. In: *2012 Annual International Conference of the IEEE Engineering in Medicine and Biology Society*. 2012 34th Annual International Conference of the IEEE Engineering in Medicine and Biology Society (EMBC). San Diego, CA: IEEE, Aug. 2012, pp. 2025–2028. ISBN: 978-1-4577-1787-1 978-1-4244-4119-8. DOI: [10.1109/EMBC.2012.6346355](https://doi.org/10.1109/EMBC.2012.6346355). URL: <http://ieeexplore.ieee.org/document/6346355/> (visited on 07/02/2019).